~~Validating~~Testing floc settling velocity models in rivers and freshwater wetlands

Justin A. Nghiem[1], Gen K. Li[1,2], Joshua P. Harringmeyer[3], Gerard Salter[1], Cédric G. Fichot[3], Luca Cortese[3], Michael P. Lamb[1]

[1]Division of Geological and Planetary Sciences, California Institute of Technology, Pasadena, 91125, USA
[2]Department of Earth Science, University of California, Santa Barbara, Santa Barbara, 93106, USA
[3]Department of Earth and Environment, Boston University, Boston, 02215, USA

Correspondence to: Justin A. Nghiem (jnghiem@caltech.edu)

Abstract. Flocculation controls mud sedimentation and organic carbon burial rates by increasing mud settling velocity. ~~Floc settling velocity can be predicted using a semi-empirical model that depends on turbulence, sediment concentration, and geochemical variables or an explicit Stokes law-type model that depends on floc diameter, permeability, and fractal properties.~~ However, calibration and validation of ~~the semi-empirical and explicit~~ floc settling velocity models ~~with direct field measurements is~~in freshwater are lacking. We ~~employed~~used a camera, in situ laser diffraction particle sizing, and ~~analysis of grain size-specific~~ suspended sediment concentration-depth profiles to measure flocs in ~~the freshwater channels and wetlands of~~ Wax Lake Delta, Louisiana. We developed a new workflow that combines our multiple floc data sources to distinguish between flocs and unflocculated sediment and measure floc attributes that were previously difficult to constrain. Sediment finer than ~20 to 50 µm ~~flocculates~~was flocculated with median floc diameter of 30 to 90 µm, bulk solid fraction of 0.05 to 0.3, fractal dimension of ~2.1, and floc settling velocity of ~0.1 to 1 mm s^{-1}, with little variation along water depth. ~~These values~~Results are consistent with ~~the~~a semi-empirical model~~, which indicates~~ indicating that ~~turbulence limits variation in~~sediment concentration and mineralogy, organics, water chemistry, and, above all, turbulence control floc settling velocity ~~on flood-to-seasonal time scales. In the explicit model, the effective~~. Effective primary particle diameter~~, commonly assumed to be the median primary particle diameter, differs by a factor of ~2 to 6~~ is ~2 µm, about two-to-six times smaller than the median primary particle diameter, and ~~can be~~is better described using a ~~simple~~ fractal theory. Flow through the floc increases settling velocity by an average factor of 2 and up to a factor of ~~~2~~7, and can be ~~explained~~described by ~~parameterizing flocs as effectively permeable clusters of primary particles. Our results provide~~a modified permeability model that accounts for the ~~first full field validation~~effect of ~~effective~~many primary particle ~~diameter and floc permeability theories, which improve floc~~ sizes on flow paths. These findings help explain discrepancies between observations and an explicit Stokes law-type settling ~~velocity predictions of the explicit model.~~model that depends on floc diameter, permeability, and fractal properties.

Formatted: English (United States)

1 Introduction

Mud, defined as grains with ~~diameter~~diameters finer than 62.5 μm, constitutes the bulk of sediment load in large alluvial rivers and deltas (Walling and Fang, 2003; Cohen et al., 2022). Mud deposition can counteract land loss in coastal areas experiencing sea level rise, subsidence, and reduced sediment supply (Blum and Roberts, 2009; Syvitski et al., 2009). ~~Mud~~Fluvial mud also hosts abundant mineral-bound organic carbon and pollutants~~, making mud fluxes in rivers relevant~~ and is thus important to the global carbon cycle (Mayer, 1994; Galy et al., 2008; Blair and Aller, 2012) and water quality (Nelson and Lamothe, 1993; Pizzuto, 2014). ~~Understanding~~Flocculation is key for understanding mud sedimentation ~~relies on knowledge of flocculation~~ because flocculation can drastically increase the in situ mud settling velocity~~, affect~~ (Lamb et al., 2020). Enhanced settling velocity affects mud ~~deposition~~exchange with the bed and ~~entrainment fluxes,~~bedform geometry (Partheniades, 1965; Schindler et al., 2015; Tran and Strom, 2019) and can ultimately alter landscape-scale mud transport ~~patterns (Lamb~~(Nicholas and Walling, 1996; Craig et al., 2020~~;~~, Zeichner et al., 2021).

Flocculation is the reversible process by which ~~individual~~ suspended sediment~~ grains~~ (primary particles) aggregate into larger and less dense particles called flocs, which can settle orders-of-magnitude faster than their primary particles (Chase, 1979; Winterwerp, 1998). Many physical, chemical, and biological ~~mechanisms are known to~~factors affect flocculation like turbulence, sediment concentration and mineralogy, organics, and water chemistry (Kranck, 1984; ~~Winterwerp, 1998~~Mietta et al., 2009; Nghiem et al., 2022). ~~In particular, researchers~~Researchers have long studied flocculation in estuaries and the ocean where salinity ~~is a key driver of~~mainly affects flocculation (Kranck and Milligan, 1980; McCave, 1984; Hill et al., 2001). High salinity promotes flocculation because cations compress the electric double layer to the point that van der Waals attraction causes grains to aggregate (i.e., DLVO theory; Derjaguin and Landau, 1941; Verwey, 1947). However, recent studies have found widespread flocculation in rivers (Lamb et al., 2020; Nghiem et al., 2022~~much~~). Much less is known about ~~flocs~~flocculation in freshwater~~ environments~~ where organic matter might instead be the main flocculating agent (Eisma et al., 1982; Lee et al., 2019; Zeichner et al., 2021). Organic matter biopolymers can bind sediment depending on charge interactions and adsorption kinetics (Yu and Somasundaran, 1996; Gregory and Barany, 2011), which classic DLVO theory cannot describe (Deng et al., 2023). Limited direct observations have shown that freshwater flocs are ~10 to 100 μm in diameter and settle at ~0.1 to 1 mm s^{-1} (Droppo and Ongley, 1994; Krishnappan, 2000; Guo and He, 2011; Larsen et al., 2009; Osborn et al., 2021). ~~These ranges largely match those measured in estuaries and the ocean (McCave, 1984; Gibbs, 1985) despite the salinity difference. More recent studies analyzed river suspended sediment concentration-depth profiles to infer floc settling velocities and revealed evidence for widespread flocculation of in rivers (Lamb et al., 2020; Nghiem et al., 2022), pointing to the need to calibrate and validate models for riverine flocs.~~

Although floc settling velocity is vital for understanding mud transport in rivers and freshwater wetlands, settling velocity models for freshwater flocs are still in their infancy. Many empirical models for estuarine flocs have been proposed (e.g., Gibbs, 1985; Manning and Dyer, 2007; Soulsby et al., 2013), but are not applicable to freshwater flocs because their parameters implicitly depend on sediment and water properties (e.g., Eisma, 1986). Strom and Keyvani (2011) derived a general floc settling velocity model by assuming that flocs are fractal aggregates and modifying ~~the classic~~ Stokes settling velocity ~~model~~theory to include floc density and permeability~~ effects~~. We refer to this ~~modified Stokes~~ model as the "explicit model" because it predicts floc settling velocity from ~~fundamental~~ physical principles. The explicit model ~~can be~~was validated against a data compilation of floc diameter and settling velocity measurements (Strom and Keyvani, 2011), but is difficult to ~~use~~apply because it ~~requires knowledge of the~~relies on floc permeability and primary particle diameter~~.~~, which are poorly constrained.

Alternatively, ~~the~~ floc diameter and settling velocity can be predicted using a flocculation model. In a seminal study, Winterwerp (1998) developed a turbulence-driven ~~model aimed at estuarine~~ flocculation model in which the relative rates of floc aggregation (due to particle collisions) and breakage (due to shear stress~~ on flocs) determine the~~) set floc diameter~~, which can be converted to floc~~ and settling velocity~~ using a settling velocity model.~~. The Winterwerp model is a function of shear rate and sediment concentration, but ~~is limited because~~ the effects of other factors ~~must be calibrated.~~are not explicit. Nghiem et al. (2022) modified the Winterwerp model to include ~~dependencies on~~additional factors known to affect flocculation: organic matter, sediment mineralogy, and water chemistry~~ and~~. They fitted the model to a global river compilation. We refer to the Nghiem et al. (2022) model as the "semi-empirical model" because ~~it contains~~the fitted parameters ~~that implicitly~~empirically account for the ~~natural heterogeneity in~~effects of floc structure, density, and permeability ~~considered in the explicit~~on floc settling velocity. The semi-empirical model was calibrated on floc settling velocity inferred from sediment concentration-depth profiles using Rouse-Vanoni theory (Nghiem et al., 2022), but has yet to be verified against direct measurements.

~~Both the explicit and semi-empirical models face many uncertainties in practice. The explicit model was validated against a large data compilation of floc diameter and settling velocity measurements (Strom and Keyvani, 2011), but the effects of primary particle diameter and floc permeability remain poorly constrained in general because paired floc diameter and settling velocity measurements alone cannot distinguish between them. The semi-empirical model was calibrated on floc diameter and settling velocity inferred from river suspended sediment concentration-depth profiles using Rouse-Vanoni theory (Nghiem et al., 2022) and has yet to be verified against direct floc measurements.~~

Here~~,~~ we combined geochemical sampling, camera observations, in situ laser diffraction particle sizing, and Rouse-Vanoni analysis of ~~suspended~~ sediment concentration-depth profiles in the freshwater Wax Lake Delta (WLD), Louisiana, USA to ~~characterize flocs and~~ examine these knowledge gaps~~.~~: floc permeability and primary particle diameter in the explicit model and validation of the semi-empirical model. First, we ~~present a detailed~~ review ~~of~~ the floc ~~theory that we aim to test~~theories (Sect. 2). We introduce the study area in Sect. 3. Next, we describe the field methods and data analysis to calculate ~~the~~ floc properties ~~to compare to theory~~ (Sect. 4). ~~Section 5 reports the results~~Importantly, our complementary data sources provide new constraints on floc properties, allowing us to isolate floc concentration and ~~theory comparison including floc fractal dimension,~~ size distribution and estimate floc permeability~~,~~ and primary particle diameter~~, floc size~~ for the explicit model. These properties, along with floc solid fraction, fractal dimension, and settling velocity ~~distributions, and semi-empirical model predictions of floc settling velocity.~~distribution, are reported in Sect. 5. In Sect. 6, we discuss the advantages of our data combination, practical considerations for predicting freshwater floc settling velocity, the physical interpretation of primary particle and permeability effects on floc settling velocity, and the leading role of environmental feedbacksturbulence in determiningsetting floc settling velocity in natural settings.

2 Floc Theory

We evaluated two complementary approaches, the explicit and semi-empirical models, to predict floc settling velocity, w_s (m s^{-1}).

2.1 Explicit Model

The explicit model for floc settling velocity, w_s (m s^{-1}), is Stokes law modified for flocs (Strom and Keyvani, 2011):) and hence predicts w_s at the scale of the individual floc:

$$w_s = \frac{R_s g D_p^2}{b_1 \Omega \nu} \left(\frac{D_f}{D_p}\right)^{n_f - 1}, \tag{1}$$

where R_s is the submerged specific gravity of sediment (= (1.65), g is gravitational acceleration (= (9.81 m s^{-2}), $D_p D_f$ (m) is the effective primary particlefloc diameter, and b_1 (dimensionless) is a shape factor assumed to be 20 (Ferguson and Church, 2004; see Sect. 6.3 for discussion). Equation (1) assumes that flocs are fractal aggregates (Kranenburg, 1994), for which a fractal solid fraction model applies:

$$\varphi = \left(\frac{D_f}{D_p}\right)^{n_f - 3}, \tag{2}$$

where φ (dimensionless) is the solid fraction, the volume fraction of the floc composed of mineral sediment. Although fractal theory is an approximation because floc structure is heterogeneous (e.g., Spencer et al., 2021), it has been well-tested for natural flocs (Kranenburg, 1994; Winterwerp, 1998; Dyer and Manning, 1999). Natural flocs contain many primary particle sizes, so D_p (m) is an effective primary particle diameter that is representative of the primary particle size distribution. Given D_f and D_p, fractal dimension, $n_f \in [1, 3]$ (dimensionless), quantifies the packing efficiency of primary particles. A compact solid grain has $n_f = 3$, while a linear chain of primary particles has $n_f = 1$. A typical fractal dimension for natural flocs is ~2 (Kranenburg, 1994; Winterwerp, 1998).). The dragAll else equal, Eq. (2) indicates that smaller flocs are denser than larger flocs and, in turn, the center of a given floc is denser than the edges.

Drag ratio, $\Omega \in (0, 1]$ (dimensionless), quantifies floc drag force reduction caused by flow passing through a permeable floc (Neale et al., 1973). (dimensionless),Specifically, Ω is the ratio of the drag force of the floc and that of an impermeable particle with the same density and diameter at the same flow velocity (Neale et al., 1973). Equivalently, Ω is the ratio of the settling velocity of the impermeable particle and that of the floc. If $\Omega <= 1$, then through flow in the floc reduces theis impermeable. $\Omega < 1$ indicates a permeability-induced drag coefficientforce reduction and increases the settling velocity relativeenhancement. Based on creeping flow theory, Ω decreases with permeability according to those of the equivalent

Formatted: Font: Cambria Math

impermeable particle at terminal settling conditions. Equation (1) assumes that flocs are fractal aggregates (Kranenburg, 1994), in which

$$\Omega = \frac{2\xi^2\left(1-\frac{\tanh\xi}{\xi}\right)}{2\xi^2+3\left(1-\frac{\tanh\xi}{\xi}\right)}, \qquad (3)$$

where the $\varphi = \left(\frac{D_f}{D_p}\right)^{n_f-3}$, (2)

φ (dimensionless permeability, $\xi^{-2} = 4kD_f^{-2}$, and k (m^2) is the solid fraction, defined as the volume fraction of the floc composed of mineral sediment grains. permeability (Neale et al., 1973). Equation (3) shows that predicting Ω is tantamount to predicting ξ^{-2}.

The fractal dimension, $n_f \in [1, 3]$ (dimensionless), controls the power law scaling between floc diameter and solid fraction. For the same floc volume, the fractal dimension quantifies the efficiency with which primary particles fill volume due to the structural configuration of primary particles. A compact solid grain is the high efficiency, high fractal dimension end-member ($n_f = 3$), while a linear chain of primary particles is the low efficiency, low fractal dimension end-member ($n_f = 1$). A typical fractal dimension for natural flocs is ~2 (Kranenburg, 1994; Winterwerp, 1998). Thus, the key inputs in the explicit model (Eq. 1) are floc diameter, D_f, fractal dimension, n_f, effective primary particle diameter, D_p, and drag ratio, Ω.

Effective primary particle diameter Of these, D_p, and drag ratio, Ω, are the outstanding unknowns in the explicit model because prior studies measuredhave well constrained floc diameter and fractal dimension (e.g., Jarvis et al., 2005; Strom and Keyvani, 2011), but did not measure D_p and Ω.). Cameras are commonly used to measure floc diameter and settling velocity, but thethis data are limited because regression onalone cannot separate the explicit model yields n_f and a coefficient conflatingeffects of D_p and Ω (Dyer and Manning, 1999; Strom and Keyvani, 2011). More independent data are neededAs such, D_p and Ω must be estimated from additional relations as follows, but these relations have yet to disentangle the effects of be tested against observations of natural flocs in freshwater rivers and deltas.

Determining an effective primary particle diameter, D_p, as required for the explicit model (Eq. 1), is uncertain because each floc carries many primary particle diameter and drag ratio, the absence of which has led to unverified assumptions about their parametrizationssizes. D_p is typically assumed to be the mean or median of the primary particle size distribution (e.g., Syvitski et al., 1995; Strom and Keyvani, 2011). However, natural flocs contain a primary particle size distribution.Alternatively, Bushell and Amal (1998) proposed a fractal D_p model to account for the distribution:

$$D_p = \left(\frac{\sum D_{pi}^3}{\sum D_{pi}^{n_f}}\right)^{\frac{1}{3-n_f}}, \qquad (34)$$

where D_{pi} is the diameter of the i^{th} primary particle in the floc. The fractal model predicts the effective primary particle diameter as a function of the primary particle size distribution and fractal dimension. This fractal D_p has the same physical volume and fills the same n_f-dimensional space as the original primary particles. (Bushell and Amal, 1998). The fractal model shows

Formatted: Indent: First line: 0.5"

thatmean or median of the effective primary particle diametersize distribution does not satisfy these conditions and thus might be very different from a simple statistical summary of the primary particle size distribution. the fractal D_p. Equation (34) has been validated using light scattering experiments on synthetic hematite grains (Bushell and Amal, 2000), but has not yet been testedgrains (Bushell and Amal, 2000). However, Eq. (4) is limited because it requires knowledge of all primary particle diameters in a floc which, like in our data, are often unknown. Instead, we followed Gmachowski (2003) and assumed the number of primary particles is sufficiently large for the central limit theorem to apply, yielding

$$D_p = \left(\overline{D_p^3}/\overline{D_p^{n_f}}\right)^{1/(3-n_f)}, \qquad (5)$$

where the overbars denote the mean. Equation (5) is simpler than Eq. (4) because it can be computed using the primary particle size distribution. We evaluate Eq. (5) herein for natural flocs. We tested the fractal D_p theory against estimates of effective primary particle diameter (Sect. 4.5.2 and 4.5.3).

We tested Existing analytical permeability models for the drag ratio, can struggle to predict Ω, (Eq. 3) because they have yet to be directly tested for natural flocs do not fulfill model assumptions of uniformly sized primary particles and uniform porosity (Eq. 2). Several experimental studies observed particularly high floc permeability incompatible with typical permeability models altogether (e.g., Johnson et al., 1996; Li and Logan, 1997).. Strom and Keyvani (2011) used a field and lab Using a data compilation of floc diameter and settling velocity and inferred that more compact field and lab flocs ($n_f \geq 2.5$) are impermeable ($\Omega = 1$) but more loosely bound flocs ($n_f < 2$) are appreciably permeable (Ω ~ 0.1 to 0.2). They compared the inferred Ω to drag ratio predictions from the , Strom and Keyvani (2011) found that the classic Brinkman permeability model, which is based on drag theory for a cluster of uniformly sized grains (Brinkman, 1947):

$$\xi^{-2} = \frac{1}{6}\left(\frac{D_p}{D_f}\right)^2\left(1+\frac{4}{3\varphi}-\sqrt{\frac{8}{\varphi}-3}\right), \qquad (4)$$

Under fractal theory, $(D_p/D_f)^2 = \varphi^{2/(3-n_f)}$ so the Brinkman model predicts the dimensionless permeability, ξ^{-2} =), vastly overestimated the inferred Ω for flocs with $n_f < 2$. However, $4kD_f^{-2}$, where k (m^2) is the floc permeability, given the solid fraction and fractal dimension. The drag ratio is then $\Omega = [2\xi^2(1-(\tanh\xi)/\xi)]/[2\xi^2+3(1-(\tanh\xi)/\xi)]$ (Neale et al., 1973). The main obstacle in applying the Brinkman model and many similar permeability models (i.e., Kim and Stolzenbach, 2002) to flocs is that flocs do not fulfill their assumptions of uniform porosity and uniformly sized primary particles. Flocs tend to be less dense at their edges (Eq. 2) owing to their fractal nature and contain a primary particle size distribution. Strom and Keyvani (2011) found that the Brinkman model overestimates Ω ~ 0.75 to 0.88 for the low n_f flocs, but it is unclear whether this indicates the Brinkman modelconclusion is invalid for flocsuncertain because they calculated Ω using reported primary particle diameters that might not be valid underif the fractal theory (Eq. 3). Nonetheless, several floc experiment studies have reported low values of Ω (highD_p model holds. Kim and Stolzenbach (2002) found that the empirical Davies permeability) incompatible with standard permeability models (e.g., model (Davies, 1953):

$$\xi^{-2} = \left(\frac{D_p}{D_f}\right)^2 [16\varphi^{1.5}(1+56\varphi^3)]^{-1}, \qquad (6)$$

predicted well the hydrodynamic force on simulated permeable fractal aggregates. Like the Brinkman model, the Davies model predicts ξ^{-2} (and hence Ω through Eq. 3) given φ and n_f because $\left(D_p/D_f\right)^2 = \varphi^{2/(3-n_f)}$ (Eq. 2).~~Johnson et al., 1996; Li and Logan, 1997).~~ Modified permeability models have been proposed to ~~account for the non-uniform pore distribution in fractal aggregates like flocs, in which the largest pores~~capture the fact that clustering of primary particles might create macropores that disproportionately ~~enhance~~set permeability (Li and Logan, 2001; Woodfield and Bickert, 2001). In particular, Li and Logan (2001) ~~simply~~ replaced D_p with a larger cluster diameter, D_c (m), in any given permeability equation (e.g., ~~Brinkman model), effectively increasing the solid fraction. The Li and Logan model posits that primary particles are clustered within flocs, so the cluster diameter sets the macropore size and floc permeability.~~Brinkman or Davies model). We tested the ~~ability~~abilities of the ~~original~~ Brinkman ~~model~~ and ~~its Li~~ Davies models and ~~Logan modification~~their Li and Logan variants, each coupled with Eq. (3), to ~~predict~~describe drag ratio estimates ~~(Sect. 4.5.2).~~.

2.2 Semi-Empirical Model

The semi-empirical model is the Winterwerp (1998) model as modified by Nghiem et al. (2022~~) to account for~~). Unlike the ~~effects~~explicit model, the semi-empirical model predicts values representative of ~~organics, sediment mineralogy, and water chemistry.~~a floc population (Winterwerp, 1998) rather than those of individual flocs. At equilibrium between floc growth and breakage, the Winterwerp model predicts floc diameter, ~~D_f (m),~~

$$D_f = \frac{k_A}{k_B}\sqrt{\frac{F_y}{\rho\nu^2}}\,(k_A/k_B)\,C\eta\,, \qquad (5)$$

$\sqrt{F_y/(\rho\nu^2)}$, in which k_A and k_B (dimensionless) are the ~~empirical~~ floc aggregation and breakage efficiencies, ρ is water density ~~(=~~ (1000 kg m^{-3}), ν is water kinematic viscosity ~~(=~~ (10^{-6} m^2 s^{-1}), F_y is the floc yield force (N), and C (dimensionless) is the volumetric sediment concentration. The Kolmogorov microscale, η (m), is the length scale of the smallest turbulent eddies in the flow and scales inversely with turbulence intensity (Tennekes and Lumley, 1972). ~~Winterwerp assumed a constant floc yield force $F_y = 10^{-10}$ N (Matsuo and Unno, 1981). Equation (5) is limited because it does not directly include the effects of biota and chemistry on flocculation (Lee et al., 2019; Zeichner et al., 2021).~~

The semi-empirical model (Nghiem et al. ~~(~~, 2022) ~~therefore modified the Winterwerp model to include~~includes the effects of organic matter, sediment mineralogy, and water chemistry in k_A/k_B using ~~parametrizations that take advantage of~~ standard geochemical ~~data~~variables measured from river sediment and water samples~~.~~, which are often more readily available than the floc parameters in the explicit model. The semi-empirical model predicts w_s, D_f, and floc cutoff diameter, D_t (m), which is the threshold grain diameter between significantly flocculated (finer) and unflocculated (coarser) sediment. Using D_t, w_s, and D_f~~. The model, calibrated on~~ inferred from a global river ~~floc~~ data compilation~~, is~~ of sediment concentration-depth profiles, Nghiem et al. (2022) calibrated the model:

$$D_t = 0.134\,(\eta D_{p,50})^{1/2}\,(\eta \tilde{D}_{p,50})^{1/2}\,(C_m\theta^2(1-\theta)^2)^{0.0734}\,(\mathrm{Al/Si})^{-0.774}\,\Phi^{-0.180}\,\Phi^{-0.180}\,, \qquad (~~6a~~7a)$$

Formatted: Spanish (Spain)
Formatted: Spanish (Spain)
Formatted: Spanish (Spain)
Formatted: Spanish (Spain)
Formatted: Spanish (Spain)
Formatted: Spanish (Spain)
Formatted: Spanish (Spain)
Formatted: Spanish (Spain)
Formatted: Spanish (Spain)
Formatted: Spanish (Spain)

$$w_s = \frac{R_s g D_{p,50}}{20\nu} \frac{R_s g \widetilde{D}_{p,50}}{20\nu} 0.306\eta(C_m\theta^2(1-\theta)^2)^{0.167}(\mathrm{Al/Si})^{-2.15}\Phi^{-0.0358}, \quad (~~6b~~7b)$$

$$D_f = 0.0180\eta(C_m\theta^2(1-\theta)^2)^{0.147}(\mathrm{Al/Si})^{-1.55}\Phi^{-0.360}, \quad (~~6c~~7c)$$

~~The~~The variables in the semi-empirical model (Eq. 7) describe the depth-averaged floc population because the floc calibration data are depth-averaged. Accordingly, depth-averaged mud volume concentration, C_m (dimensionless), is ~~assumed to be~~ the representative sediment concentration for flocculation because, although sand ~~grains are typically not observed~~can be incorporated in flocs (Whitehouse et al., 2000; Manning et al., 2010), mud is typically far more abundant (Lamb et al., 2020; Osborn et al., 2021). ~~The~~Depth-averaged median primary particle diameter, ~~$D_{p,50}$~~$\widetilde{D}_{p,50}$ (m), is ~~a~~taken as the primary particle ~~grain~~ size metric. Sediment Al/Si (molar ratio) represents ~~sediment~~ mineralogy because clay minerals ~~tend to be~~are enriched in Al/Si compared to feldspar and quartz (e.g., Galy et al., 2008; Bouchez et al., 2014). θ (dimensionless) is the organic cover fraction, the fraction of the sediment grain surface covered with organic matter (Smellie and LaMer, 1958). ~~The relative~~Relative charge density, Φ (dimensionless), quantifies the effect of salinity and sediment mineralogy on flocculation using diffuse double layer theory (Rommelfanger et al., 2022). Φ is the ratio of net cation ~~charges~~charge in solution and that at the surface of sediment grains. Flocculation is expected at higher values of Φ where the cation concentration overcomes the negative charges on the surfaces of clay minerals. ~~The semi-empirical model (Eq. 6) provides a complete set of floc predictions in freshwater and complements the explicit model because it relies on hydrodynamic and geochemical data, which are often more readily available than direct floc measurements. However, the semi-empirical model still needs to be verified using observations of floc diameter and settling velocity because they were inferred from sediment concentration-depth profiles to calibrate the model. In this study, we combined geochemical and floc measurements in the Wax Lake Delta to verify the semi-empirical model and constrain the explicit model parameters.~~

In this study, we combined floc and geochemical measurements in the Wax Lake Delta to constrain explicit model parameters and verify the semi-empirical model. Our objective for the explicit model is to evaluate primary particle diameter and floc permeability theory because these parameters have not been fully tested before for natural flocs. Our objective for the semi-empirical model is to validate it using direct observations of floc diameter and settling velocity.

3 Study Site

We conducted fieldwork in the Wax Lake Delta, a river-dominated freshwater delta in the Mississippi River Delta complex (Fig. 1ab). The lower Mississippi River conveys water and sediment to WLD via the Atchafalaya River and Wax Lake Outlet, which was dredged in 1942 (Fig. 1b; Latimer and Schweizer, 1951). The topset of WLD became subaerial after the 1973 Mississippi River flood and has since been aggrading and prograding into the Gulf of Mexico with little human intervention (Roberts et al., 1980; Jensen et al., 2022). Interactions between the river, tides, wind, and vegetation cause wide variability in delta island inundation, which can expose and submerge much of the levees along island margins (Geleynse et al., 2015).

Formatted: Spanish (Spain)
Formatted: Spanish (Spain)
Formatted: Spanish (Spain)
Formatted: Spanish (Spain)
Formatted: Spanish (Spain)
Formatted: Spanish (Spain)
Formatted: Spanish (Spain)
Formatted: Spanish (Spain)
Formatted: Spanish (Spain)
Formatted: Spanish (Spain)
Formatted: Spanish (Spain)
Formatted: Spanish (Spain)
Formatted: Spanish (Spain)
Formatted: Spanish (Spain)
Formatted: Spanish (Spain)
Formatted: Spanish (Spain)
Formatted: Spanish (Spain)
Formatted: Spanish (Spain)
Formatted: Spanish (Spain)
Formatted: Spanish (Spain)
Formatted: Spanish (Spain)
Formatted: Indent: First line: 0"

Despite the proximity of WLD to the Gulf of Mexico, the water remains fresh even during low river discharge (Holm and Sasser, 2001).

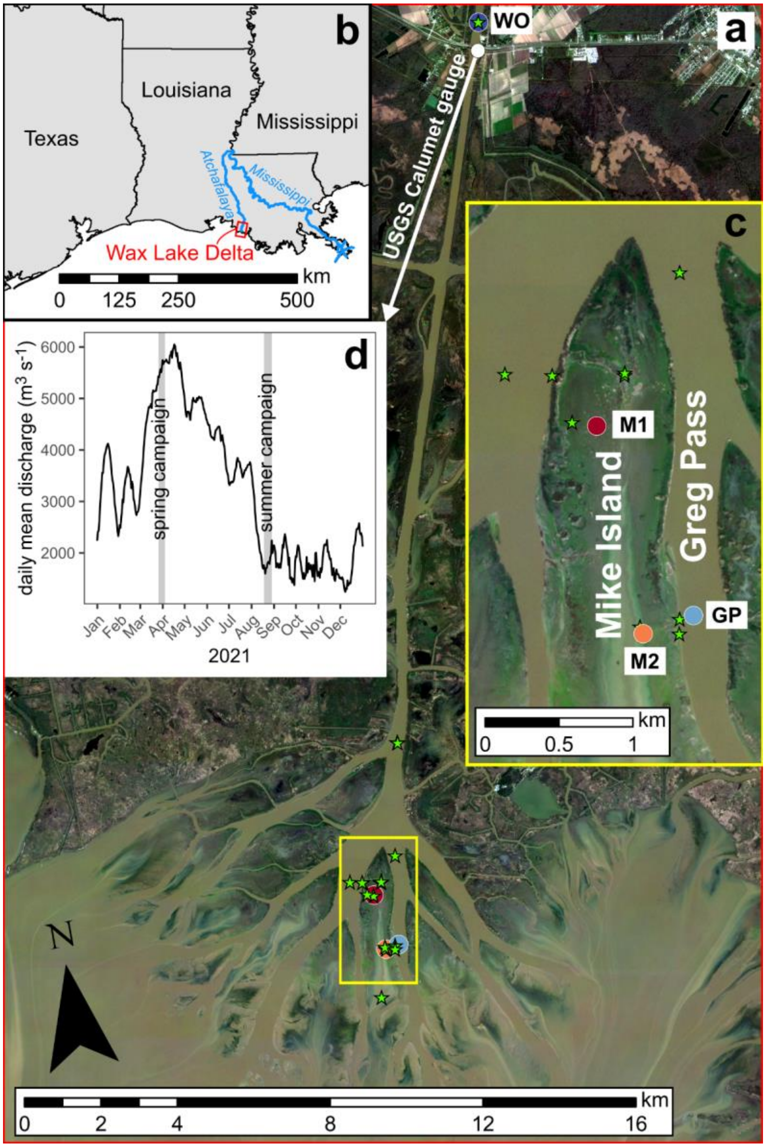

b
Louisiana
Mississippi
Texas
Atchafalaya
Mississippi
Wax Lake Delta
0 125 250 500 km
a
WO
USGS Calumet gauge
c
M1
Mike Island
Greg Pass
GP
M2
0 0.5 1 km
d
daily mean discharge (m³ s⁻¹)
6000
5000
4000
3000
2000
spring campaign
summer campaign
Jan Feb Mar Apr May Jun Jul Aug Sep Oct Nov Dec
2021
N
0 2 4 8 12 16 km

Figure 1: (a) Map of Wax Lake Delta, Louisiana with sample sites. ~~Colored circles~~Circles indicate main sample sites with sediment concentration-depth and LISST profiles. ~~Green stars~~Stars indicate additional sediment concentration-depth profile sites without LISST and floc cam measurements. Satellite image is from January 2021, Image © 2021 Planet Labs PBC~~.~~, at relatively low discharge and tide to highlight the full island extents. (b) Map of Louisiana coast region. (c) Inset map of Mike Island and Greg Pass. (d) 2021 hydrograph of Wax Lake Outlet at Calumet, LA (USGS stream gauge 07381590). Gray bands indicate fieldwork periods.

We completed fieldwork in WLD during March and April 2021 (spring campaign) and August 2021 (summer campaign) as part of the NASA Delta-X project. During the spring campaign, the discharge into WLD was ~5500 $m^3 s^{-1}$, which is near the peak for 2021 (Fig. 1d). During the summer campaign, the discharge was ~1800 $m^3 s^{-1}$ and close to the low discharge for the year. We studied four sites: Wax Lake Outlet (WO), Greg Pass (GP), northern Mike Island (M1), and southern Mike Island (M2) (Fig. 1ac). Site WO is about 20 km upstream of the delta apex. Site GP is near the center of Greg Pass, the distributary channel east of Mike Island. Sites M1 and M2 on Mike Island are in a tidally~~-~~ forced shallow wetland. We sampled all sites during the spring campaign, but only sampled site GP during the summer campaign. At each site, we collected vertical profiles of suspended sediment samples (i.e., concentration-depth profiles) and in situ particle size distributions and concentrations with a Sequoia Scientific LISST-200X (LISST) instrument. We collected 8 profiles with paired LISST and sample measurements. We took floc images with a camera system (floc cam) for 4 profiles. We sampled 16 additional concentration-depth profiles distributed throughout WLD without matching LISST or floc cam data, including one profile in October 2019 during a separate field campaign. We also collected water samples to measure major cation and anion concentrations at 20 profile sites and dissolved inorganic carbon (DIC) concentration at 15 profile sites.

4 Methods

~~We use systematic nomenclature throughout this paper to differentiate between mineral sediment grains, flocs, and a mixture of both. We use the terms "grain" and "sediment" throughout~~Herein we use the terms "grain" or "sediment" to mean the solid disaggregated mineral sediment, which might or might not have been flocculated in situ. As standard in the flocculation literature, we use "primary particle" to refer to the constituent sediment grains inside flocs. ~~In contrast, we~~We use "particle" alone (i.e., without "primary") to refer generically to the in situ suspended material, which includes flocs and unflocculated sediment. This nomenclature is standard throughout the paper and is critical for distinguishing between flocs, unflocculated sediment, and fully dispersed sediment.

~~We used three common floc measurement methods: (1) cameras, (2) in situ particle sizing, and (3) inversion of suspended sediment concentration-depth profiles using the Rouse-Vanoni equation. Flocs are sensitive to their local conditions, so measurements are designed to minimize disturbances.~~ We designed our field methods to measure all variables in the explicit and semi-empirical models and test their floc settling velocity predictions. We collected sediment concentration-depth profiles and acoustic Doppler current profiler (ADCP) flow velocity measurements (Sect. 4.1). We measured the major ion concentrations of the water, sediment organic matter concentration, and elemental sediment composition (Sect. 4.2). The

Formatted: Indent: First line: 0.5"

primary floc data sources are in situ particle sizing with LISST (Sect. 4.3), a camera (Sect. 4.4), and analysis of suspended sediment concentration-depth profiles (Sect. 4.5), each with different advantages and limitations.~~Cameras directly measure floc size and settling velocity (e.g., Mikkelsen et al., 2004; Benson and French, 2007; Osborn et al., 2021), but require reliable image processing algorithms and can be limited by the small number of identifiable flocs. Cameras also cannot detect flocs finer than the pixel resolution, but increasing resolution shrinks the field of view.~~ In situ particle sizing measures in situ particle size distribution and concentration using laser diffraction (e.g., Agrawal and Pottsmith, 2000; Guo and He, 2011), but cannot distinguish between flocs and unflocculated sediment. Although laser diffraction might be sensitive to primary particles within flocs (Graham et al., 2012), studies have found good agreement between floc size distributions measured by camera and laser diffraction (Mikkelsen and Pejrup, 2001; Mikkelsen et al., 2005). Cameras directly measure floc size and settling velocity (e.g., Mikkelsen et al., 2004; Benson and French, 2007; Osborn et al., 2021). However, camera methods require reliable image processing algorithms, can be limited by the small number of identifiable flocs, and cannot detect flocs finer than the pixel resolution. Depth-averaged floc settling velocity can be inferred from stratification in grain size-specific sediment concentration-depth profiles (Lamb et al., 2020; Nghiem et al., ~~Recent studies have fitted the Rouse-Vanoni equation to grain size-specific suspended sediment concentration-depth profile data to infer depth-averaged floc settling velocity and the grain sizes within flocs (Lamb et al., 2020; Nghiem et al., 2022). However, this technique relies on the sediment diffusivity ratio parametrization, is indirect, and cannot measure floc diameter~~2022), but this technique is indirect and does not reveal floc diameter. We combined these data sources in novel ways (Sect. 4.6) to derive floc variables (floc diameter, floc settling velocity, fractal dimension, effective primary particle diameter, drag ratio) required to test theory and the floc settling velocity models.

~~We used all three methods to measure floc diameter and settling velocity (Sect. 4.1-4.3). First, we identified the floc cutoff diameter by inverting grain size-specific concentration-depth profiles with the Rouse-Vanoni equation (Sect. 4.4). With these floc constraints, we combined the data sources to estimate explicit model variables (Table 1; Sect. 4.5): floc solid fraction, fractal dimension, drag ratio, and effective primary particle diameter. We collected a suite of water and sediment geochemistry data as inputs into the semi-empirical model (Sect. 4.6).~~

Table 1: Estimated floc variables and their data sources. The variables are listed by order in the data processing workflow. In ~~the~~ Data Source ~~column~~, “sediment” refers to sediment grain size distribution, concentration, and Rouse-Vanoni equation fitting ~~data from individual suspended sediment samples and sediment concentration-depth profiles.~~results. The primary data source (if any) is listed first. In ~~the~~ Description ~~column~~, the data sources are indicated in parentheses next to input variables ~~for variables with~~if there are multiple ~~data~~ sources.

Variable	Data Source	Description	Section or (Equation)

Formatted Table

Paired diameter (m) and settling velocity (m s^{-1}) of individual flocs	floc cam	Diameter: Extracted using image analysis Settling velocity: Calculated by manually tracking particles	4.~~3~~4
Floc cutoff diameter, D_t (m)	sediment	Selected by eye from grain diameter-settling velocity results from Rouse-Vanoni fitting of grain size-specific concentration-depth profiles	4.5~~.1~~
Floc size distribution (m) and concentration	LISST, sediment	Particle size distribution and concentration (LISST) removing the unflocculated sediment fraction in the classes coarser than D_t (sediment)	4.~~5~~6.1
Primary particle size distribution (m) and concentration	sediment	Grain size distribution and sediment concentration removing the fraction coarser than D_t	4.~~5~~6.1
Bulk solid fraction, $\bar{\varphi}$	sediment, LISST	Ratio of primary particle (sediment) and floc concentrations (LISST, sediment)	4.~~5~~6.1
Fractal dimension, n_f	LISST, sediment	Calculated ~~such that the bulk solid fraction across~~to ensure consistency between $\bar{\varphi}$ (sediment, LISST) and mean settling velocity over the floc size distribution (LISST, sediment)~~ equals the calculated $\bar{\varphi}$ (sediment, LISST)~~	4.~~5~~6.2 (~~10~~11)
Effective primary particle diameter, D_p (m)	LISST, sediment	Calculated using n_f (LISST, sediment) and $\bar{\varphi}$ (sediment, LISST)	4.~~5~~6.2 (~~8b~~9)
Drag ratio, Ω	floc cam, LISST, sediment	Calculated using floc cam-measured floc diameter and settling velocity (floc cam) by solving the floc settling velocity equation (Eq. 1) for Ω with the calculated n_f (LISST, sediment) and D_p (LISST, sediment)	4.~~5.2~~6.3 (1)
Floc settling velocity distribution (m s^{-1})	LISST, floc cam, sediment	Converted floc size distribution (LISST, sediment) using the floc settling velocity equation (Eq. 1) with calculated Ω (floc cam,	4.~~5.2~~6.4 (1)

		LISST, sediment), n_f, and D_p (both LISST, sediment)	

4.1 Suspended Sediment Sampling and Hydrodynamic Measurements

Nghiem et al. We briefly summarize(2021) describe our suspended sediment sampling methodsand lab analysis in full, which are documented in full in summarized here.Nghiem et al. (2021). For each profile, we collected suspended sediment samples at different heights above the bed from a boat with an 8.2- L Van Dorn sampler. Each profile took about 40-60 min to sample in full. At the channel sites (WO and GP), we collected samples whileisokinetically by drifting over the target location to sample isokinetically at the local current speed (Edwards and Glysson, 1999) and minimize sampling bias. In contrast, we). We sampled while stationary at the wetland sites (M1 and M2) because the airboat used for sampling could not drift with the current. We expect that these samples are still representative of the in situ suspended sediment because of the relatively slow depth-averaged flow velocities inside the wetland (~0.1 m s^{-1}). We also collected concurrent flow velocity profile measurements with a Teledyne RiverPro acoustic Doppler current profiler (ADCP) instrument. We filtered each sample through 0.2 µm pore size polyethersulfone filter paper (Sterlitech). We) and froze the filtered sediment until ready for lab analysis.. In the lab, we measured thedried and weighed samples to measure sediment concentration and grain size distribution of each suspended sediment sample. We oven-dried and weighed each sample to calculate the sediment concentration as the ratio of the sediment mass and total sample volume. We discarded data in which the calculated sediment concentration is anomalously low or high compared to other samples in the same profile because these samples are not representative of the in situ steady state sediment concentration.. We decarbonated, oxidized, and deflocculated an aliquot of each sediment sample for grain size analysis (following Douglas et al., . (2022).) to fully disperse the sediment. We measured the volume-based grain size distribution (i.e., fully dispersed sediment grains) using a Malvern Mastersizer 3000E laser diffraction particle size analyzer with the non-spherical scattering model from 0.2 to 2100 µm in 100 logarithmically spaced bins. For each concentration-depth profile, we calculated the depth-averaged grain size distribution by depth-averaging the concentration in each grain size class with the trapezoidal rule and renormalizing the depth-averaged concentrations. We extrapolated a constant concentration in the unmeasured regions below the deepest measurement and above the shallowest measurement for the integration. We summed the class-specific depth-averaged concentrations to obtain the total depth-averaged sediment concentration. To obtain depth-averaged mud concentration, C_m, for the semi-empirical model, we summed the concentrations in the mud classes only.

We measured flow velocity profiles using a Teledyne RiverPro ADCP instrument concurrent with suspended sediment sampling. We deployed the ADCP near the water surface looking downward. The ADCP measured the flow velocity profile to within 5 to 15 cm of the bed at a frequency of ~1 Hz. We averaged about 100 to 1000 velocity profiles in the island sites and about 50 in the channel sites to obtain the representative velocity profiles at the concentration-depth profiles. We averaged data within a radius of 1.5 times the flow depth from the concentration-depth profile location and within 10 s of collecting a suspended sediment sample. For the deeper flows (>10 m) in Wax Lake Outlet and the delta apex, the velocity profiles contain about 50 bins in the vertical. The shallow channel profiles (3 to 4 m depth) have about 10 to 30 bins. The island profiles, with depths of 1 m or less, have about 5 bins. The bin height is about 10 to 20 cm for the deeper flows and about 5 to 10 cm for the shallower flows. We did not observe any clear wind or vegetation signatures in the representative velocity profiles (e.g., Baptist et al., 2007).

We estimated the total boundary shear velocity, u_* (m s^{-1}),~~ for each profile~~ by fitting ~~the measured ADCP~~each representative flow velocity profile to the law of the wall (e.g., García, 2008). The law of the wall is ~~commonly used to model~~reasonable because the representative velocity profiles visually show a clear linear trend between flow velocity ~~profile through~~and the ~~entire depth, but is only strictly valid in the bottom 20~~logarithm of height. However, some data above 50% of the flow depth ~~(~~deviate from the linear trend likely due to tide and wake effects (Soulsby and Dyer, 1981; Nezu and Nakagawa, 1993). ~~ADCP~~We excluded this upper data ~~quality declines near the bed, so we~~and fitted the law of the wall using ~~both the full flow velocity and the truncated flow velocity profile in the bottom 20% depth. We chose the fit that had the higher coefficient~~a weighted least squares regression with weights equal to the reciprocal of the velocity variance. The coefficients of determination ~~and calculated~~ have a median of 0.90 and range from 0.17 to 0.99. We used the shear velocity ~~from the fitted coefficients. We calculated the~~to calculate the near-bed Kolmogorov microscale~~, η (m), using the shear velocity.~~. The Kolmogorov microscale ~~is~~ varies with height above the bed as η ~~$= (\nu^3/\varepsilon)^{1/4}$~~$(z) = (\nu^3/\varepsilon)^{1/4}$, where ε (m^2 s^{-3}) is the dissipation rate of turbulence kinetic energy per unit mass~~. We used~~, and $\varepsilon = (u_*^3/\kappa)(1/z - 1/h)$, where κ (dimensionless) is the von Kármán constant (= 0.41), z (m) is height above the bed, and h (m) is the water depth (Nezu and Nakagawa, 1993). Following Nghiem et al. (2022), we chose η as the value at 10% of the flow depth (i.e., near-bed value; Sect. 4.5).

4.2 Geochemical Measurements for Semi-Empirical Model

We measured sediment Al/Si using X-ray fluorescence (XRF) for 33 samples for the semi-empirical model. Due to sample mass limitations, we measured quantitative Al/Si using glass pellet fusion on a 4 kW Zetium Panalytical XRF analyzer for only 7 samples. For the remaining 26 samples, we measured semi-quantitative Al/Si using a Rigaku Primus IV XRF Spectrometer because it required less mass. We re-analyzed the samples that had been measured on the Zetium using the Rigaku to calibrate a linear equation (R^2 = 0.91) converting the semi-quantitative Al/Si to quantitative Al/Si. Using the converted quantitative Al/Si, we calibrated a linear equation between Al/Si and volume fraction finer than a certain grain size threshold so we could predict Al/Si for cases in which grain size distribution is known but we did not measure Al/Si. We calculated the coefficients of determination for many grain size thresholds and selected the model with the highest R^2 ($\mathrm{Al/Si} = 0.099 + 0.16[\text{volume fraction finer than } 19.2\ \mu\text{m}]$; R^2 = 0.88). We predicted Al/Si from the depth-averaged grain size distributions (Sect. 4.1) for all concentration-depth profiles using this grain size relationship.

We measured total organic carbon (TOC) concentration of suspended sediment samples to calculate θ in the semi-empirical model. Sediment aliquots were decarbonated by leaching with 2 M HCl at 80°C and dried. Samples were weighed before and after decarbonation to correct for the fraction of sediment mass lost during decarbonation. TOC concentration was measured using an Exeter Analytical CHN analyzer with uncertainties determined from repeat measurements of reference

Formatted: Indent: First line: 0"

Formatted: English (United Kingdom)

Formatted: English (United Kingdom)

Formatted: English (United Kingdom)

Formatted: English (United States)

materials. We depth-averaged TOC concentrations for each concentration-depth profile using the trapezoidal rule on measured TOC concentrations weighted by sediment concentration. We assumed all organic matter was cellulose to convert depth-averaged TOC concentration to organic matter concentration (Nghiem et al., 2022). We calculated θ using the computed organic matter concentration and depth-averaged median primary particle diameter (Sect. 4.6.1; Nghiem et al., 2022).

We used ion chromatography and cavity ring-down spectroscopy to measure the major ion concentrations (cations: Na^+, K^+, Ca^{2+}, Mg^{2+}; anions: Cl^-, HCO_3^-, SO_4^{2-}) of water samples and calculate Φ for the semi-empirical model (Nghiem et al., 2022; Rommelfanger et al., 2022). We measured dissolved inorganic carbon (DIC) concentrations using a Picarro Cavity-Ring Down Spectroscopy G2131-*i* and assumed that all DIC was HCO_3^- to calculate HCO_3^- concentrations. For DIC, about 6 mL of filtered river water was injected through a 0.2 μm syringe filter into an evacuated and pre-weighed 12 mL exetainer. Samples were acidified with 10% phosphoric acid. The resulting CO_2 was carried in a nitrogen stream for total carbon measurements (Dong et al., 2018). DIC concentration was calibrated against weighed and acidified optical calcite standard reference materials. Concentrations of the rest of the ions were measured by ion chromatography at the Department of Geography, Durham University and checked by regular measurements of the LETHBRIDGE-03 standard. We solved for the HCO_3^- concentration using charge balance for cases in which we had ion chromatography measurements but did not measure DIC concentration.

4.~~2~~3 In Situ Particle Size Distribution and Concentration Measurements

~~We briefly summarize our methods for measuring in situ particle size distribution and concentration, which are documented in Fichot and Harringmeyer (2021). We~~ We used a LISST~~-200X~~ instrument to measure in situ particle size distribution and concentration. We assumed that the particles measured by LISST were either flocs or unflocculated sediment. The LISST measures the particle volume concentration, including the pores within flocs, from 1 to 500 μm in 36 logarithmically spaced size bins ~~(1 to 500 μm)~~ using laser diffraction at a rate of 1 Hz (Sequoia Scientific, 2022). We deployed the LISST attached to a rope from a boat in drift and measured downcast profiles ~~to the bottom or the end of the rope~~ by lowering the LISST at a rate of about 0.1 m s^{-1}. ~~Angular~~Optical laser transmission was within recommended ranges (Sequoia Scientific, 2022). We inverted the angular scattering intensity of the laser ~~was inverted~~using the irregular shape model to calculate ~~suspended~~the particle size distribution ~~using the manufacturer-provided software set for non-spherical particles.~~(Agrawal et al., 2008). For each LISST cast, we averaged particle size distribution and concentration data into 12 bins uniformly spaced with height to improve data display. We calculated the depth-averaged particle size distribution using the trapezoidal rule with the binned concentrations as described in Sect. 4.1. Further LISST methods are documented in Fichot and Harringmeyer (2021).

4.~~3~~4 Floc Imaging

We measured floc diameters and settling velocities ~~of flocs~~ with a custom~~-built~~ imaging device called the "floc cam" (Fig. 2a). The floc cam is a frame on which we mounted a camera and a modified 2.2 L Van Dorn sampler. We installed a 7 cm diameter window on the side of the sampler through which a backlight illuminates the interior. On the opposite side, we installed a 3 cm diameter window through which a camera can take photos. ~~We painted the interior of the sampler black to minimize light reflection. We installed two 10 cm tall half-pipes of 1 in PVC pipe in the sampler to increase interior surface roughness and reduce turbulence of collected samples.~~ For each floc cam sample, we followed the same procedure for suspended sediment sampling up until the sample was retrieved from depth. ~~Then, we~~We then mounted the sampler in the floc cam frame and took photos of backlit particles within the sampler using a mounted camera (Nikon D750) equipped with an AF-S Micro NIKKOR 60 mm f/2.8G ED lens (Fig. 2a). We programmed the camera to take photos at a rate of 4 Hz ~~(0.25 s interval).~~. Once the sampler and camera were in place, we covered the ~~entire~~ frame with a black tarp to shield the camera from ambient light. The time between sample collection and the start of image collection was ~~typically ~~~about 1 min. We allowed the camera to take photos for a few minutes, yielding an image time series for each floc cam sample. We ~~calibrated one~~ measured a resolution of 6 µm per pixel ~~per 6 µm~~ in the focal plane of the camera by photographing a ruler.

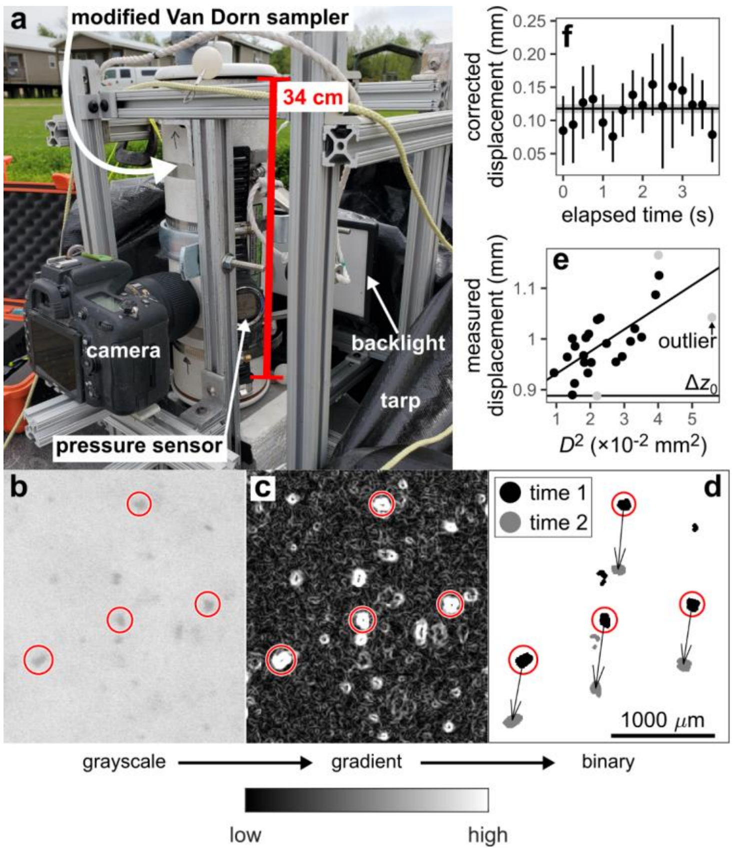

Figure 2: Floc cam data collection and processing. (a) Floc cam setup. During image collection, the black tarp covered the sampler and frame to block external light. (b) Example floc cam grayscale image ~~of particles.~~. (c) 2D gradient of the grayscale image. High-gradient pixels correspond to particle borders. (d) Binarized particles showing particle displacement between an image pair. Scale in panel d also applies to panels b and c. (e) Example scatterplot of squared diameter, *D*²$^{}$, and measured displacement. Δz_0 indicates the fitted background correction. (f) Time series of corrected displacement for a single tracked particle across multiple image pairs. The corrected displacement isolates the displacement due to gravitational settling from that due to background currents.

We detected particles in each image ~~time series~~ with the MATLAB Image Processing Toolbox following ~~a gradient-based method to detect and remove out-of-focus particles (~~Keyvani and Strom~~,~~ (2013). We converted each image ~~in a time~~

Formatted: Indent: First line: 0.5"

series to grayscale and cropped the image to a smaller area of interest. We rescaled the pixel values in the cropped image and applied a Gaussian smoothing filter (Fig. 2b). Next, weWe took the gradient of the image with a central difference method (Fig. 2c). We binarized the gradient image using an empirically-determined a gradient cutoff, determined by trial-and-error, to exclude any particles where the gradient was too small (i.e., the particle was out-of-focus; Fig. 2d).2d) but retain a sufficient number of detected particles. We applied morphological erosion and dilation on the binary image to remove noise speckles and connect fragments belonging to the same particle. Finally, we filled any holes within thedetected particles because the gradient method identifies particle edges.

WeTo calculate settling velocity, we tracked particles manually between successive frames using the processedin each binary imagesimage time series of in-focus particles (Fig. 2d) to calculate settling velocity.). We identified the same particle across frames according to particle size, shape, and displacement. We tracked 100 unique particles for each image time series over an image time span of 10 to 20 s and only recorded particles that could be tracked for at least three consecutive frames. The mean number of frames over which we tracked particles is 7.4. For each tracked particle, we calculated the diameter as the diameter of an equal-area circle using the second-largest measured particle area to limit the effect of exclude outliers. Background currents affected particle motion because settling velocities calculated with measured displacements were unrealistically high and, in some cases, particles moved upward. We used a regression method to remove the effect of background currents on observed particle motion and isolate particle displacement due to gravitational settling in which weonly. We assumed that background currents perfectly advected particles (Smith and Friedrichs, 2015). Under this assumption, theThe particle displacement between an image pair is $\Delta\hat{z} = \Delta z + \Delta z_0$ where $\Delta\hat{z}$ (m) is the observed vertical displacement of the particle, Δz (m) is the displacement due to gravitational settling, and Δz_0 is the displacement due to background currents. For a given time interval, Stokes law predicts that the gravitational displacement in a given time scales with the square of particle diameter, *D*. We assumed that Δz_0 is independent of particle size because the particles are sufficiently small. CombiningUsing the data of all tracked particles in an image pair, we regressed $\Delta\hat{z}$ against D^2 according to the equation $\Delta\hat{z} = cD^2 + \Delta z_0$ (Fig. 2e). We recovered Δz_0 as the intercept and solved for Δz (Fig. 2f) for all particles and consecutive image pairs. We discarded the data for which $\Delta\hat{z}$ fell into the 95% confidence interval of the estimated Δz_0 because the uncertainty relative to $\Delta\hat{z}$ precludes resolution of Δz for these data.. This filtering retained 222 out of an initial 400 total tracked particles remained (~(56%) after this filtering. Floc porosity and permeability might be responsible for the uncertainty because they also affect settling velocity. For each particle, we%). We calculated settling velocity for each particle as the mean of Δz divided by the time interval between images.(0.25 s).

4.45 Rouse-Vanoni equation inversionEquation Analysis of concentration-depth profilesSediment Concentration-Depth Profiles

Rouse-Vanoni equation fits to grain size-specific concentration-depth profiles provide inferred floc cutoff diameter and depth-averaged floc settling velocity estimates (Lamb et al., 2020; Nghiem et al., 2022). The Rouse-Vanoni equation models the suspended sediment concentration as a function of height from the bed, z, in a flow of depth h assuming a balance of gravitational sediment settling and upward turbulent sediment fluxes (Rouse, 1937):

$$\frac{C_i}{C_{bi}} = \left(\frac{\frac{h-z}{z}}{\frac{h-h_b}{h_b}}\right)^{p_i}, \qquad (78)$$

where C_i (dimensionless) is the sediment volume concentration, C_{bi} (dimensionless) is the sediment volume concentration at the near-bed height h_b (m), p_i (dimensionless) is the Rouse number, and the subscript i denotes the ith grain size class. Vertical concentration stratification increases with Rouse number, $p_i = w_{si}/(\kappa\beta u_*)$, where w_{si} (m s^{-1}) is the in situ grain size-specific settling velocity. The diffusivity ratio, β (dimensionless), is the ratio of turbulent sediment diffusivity and turbulent momentum diffusivity and accounts for the fact that sediment does not exactly follow turbulent eddies (e.g., García, 2008). Flux Richardson numbers, calculated using the settling velocities of flocs and unflocculated sediment (Sect. 5.8), have a median of 2.7×10^{-4} and maximum of 7.1×10^{-3}, indicating a negligible sediment-induced turbulence damping effect on flow velocity and concentration-depth profiles (Smith and McLean, 1977; Wright and Parker, 2004).

If β and u_* are known, then w_{si} can be calculated from the fitted p_i. Past studies using this method have interpreted the inferred settling velocity for fine silt and clay grain sizes as a depth-averagedthe floc settling velocity because it is much faster than the settling velocity theory prediction for individual grains (Lamb et al., 2020; Nghiem et al., 2022). β is an obstacle to calculating w_{si} because predicting β is still an open question (De Leeuw et al., 2020; Lamb et al., 2020). β is often assumed to be unity. Deviations from unity have been attributed to sediment-induced density stratification (Wright and Parker, 2004; Moodie et al., 2020) and grain size-dependent momentum effects (Carstens, 1952; Csanady, 1963; Graf and Cellino, 2002). Limited evidence shows that the diffusivity ratio for flocs, β_{fl}, might follow an existing formulation for solid grains (Izquierdo-Ayala et al., 2021, 2023), but still requires more investigation. For simplicity, we assumed $\beta = 1$ for flocs and sediment grains. We re-evaluate this assumption for flocs with independent floc settling velocity data in Sect. 5.92020; Nghiem et al., 2022). Nghiem et al. (2022) used these inferred floc settling velocities to calibrate the semi-empirical model and identify the floc cutoff diameter, D_c. Sediment finer than D_c is significantly flocculated, while sediment coarser than D_c is not significantly flocculated.

β is an obstacle to calculating w_{si} because its exact form is unknown (De Leeuw et al., 2020; Lamb et al., 2020). Prior studies invoked sediment-induced density stratification (Wright and Parker, 2004; Moodie et al., 2020) and grain size-dependent momentum effects to model β (Carstens, 1952; Csanady, 1963; Graf and Cellino, 2002). However, it is unknown whether these formulations for solid grains apply to the diffusivity ratio for flocs, β_{fl}. In past work, β_{fl} was extrapolated from relations for the sand diffusivity ratio for sand (De Leeuw et al., 2020; Lamb et al., 2020; Nghiem et al., 2022). Recent work showed that β_{fl} is typically smaller than 1 and increases with w_{si}/u_* (Izquierdo-Ayala et al., 2021, 2023; Egan et al., 2022), but is limited because the floc concentration was calibrated from acoustic backscatter data without partitioning by floc size and settling velocity.

Formatted: Indent: First line: 0.5"

Following Lamb et al. (2020) and Nghiem et al. (2022), we fitted the log-linearized Rouse-Vanoni equation to grain size-specific concentration-depth profiles (e.g., profiles of the dispersed, unflocculated sediment) from the concentrations and grain size distributions of the suspended sediment samples. grains), an example of which is depicted in Fig. 3a. We converted the sediment mass concentrations to volume concentrations assuming a sediment density of 2650 kg m^{-3} and used $h_b = 0.1h$ (De Leeuw et al., 2020). For each grain size class, we computed the grain size-specific concentration asis the total sediment concentration times the volume fraction in the size class from the grain size distribution (Sect. 4.1). We estimated the grain size-specific Rouse number, p_i, from the Rouse-Vanoni equation fits. We used shear velocity estimates (Sect. 4.1) and $\beta = 1$ to calculate w_{si}. Figure 3b shows grain diameter and calculated w_{si} for the concentration-depth profiles with corresponding LISST measurements. We identified the floc cutoff diameter, D_t, by eye for each concentration-depth profile as the diameter below which the inferred settling velocity begins to depart significantly from conventional settling velocity theory (grain settling velocity, $w_{sg} = \left(R_s g D_g^2\right)/\left(c_1 \nu + \sqrt{0.75 c_2 R_s g D_g^3}\right)$ for grain diameter, D_g, $c_1 = 20$, and $c_2 = 1.1$; Ferguson and Church, 2004). for each grain size class and each sediment concentration-depth profile. We used shear velocity estimates from ADCP flow velocity profiles (Sect. 4.1), assumed $\beta = 1$ as a starting point to approximate w_{si}, and identified D_t. We calculated the Rouse-estimated floc settling velocity as the median w_{si} within grain diameters finer than D_t (Nghiem et al., 2022).

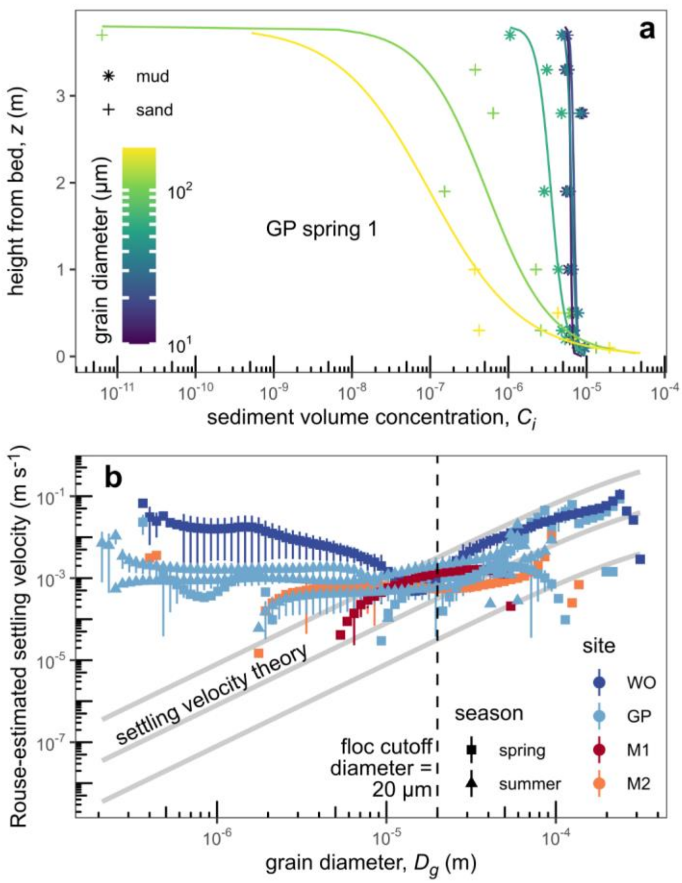

Figure 3: Rouse-Vanoni equation results. (a) Example of sediment volume concentration as a function of height above bed for profile GP spring 1. We used the full 100 grain size classes in all calculations, but reclassified the data into 6 classes for this panel only to improve readability. Curves represent the best-fit Rouse-Vanoni profiles (Eq. 8). Data scatter likely represents spatiotemporal variations in turbulence, bedforms, and/or other natural sources of variability. (b) Grain diameter and Rouse-estimated in situ settling velocity assuming $\beta = 1$ for concentration-depth profiles with LISST measurements. Gray settling velocity theory curves indicates the Ferguson and Church (2004) model with an order-of-magnitude above and below. Vertical bars represent the

propagated 68% confidence interval on the Rouse number estimates. Points without vertical bars have confidence intervals that overlap with 0.

4.~~5~~6 Estimating Floc Properties

Here we describe how we combined our floc data sources (Sect. 4.3-4.5) to calculate floc properties.

4.~~5~~6.1 Floc and Primary Particle Size Distribution and Concentration

Our first goal was to delineate the size distribution~~,~~ and concentration of flocs and primary particles. To do this, we paired LISST and sediment sample data because they record mixtures of different types of particles (Fig. 4). LISST measured the size distribution and concentration of flocs and unflocculated sediment grains together (i.e., in situ particles; Sect. 4.3). LISST particle concentration is expressed as volume concentration and includes both the volume of mineral sediment and that of pores between primary particles within flocs (Mikkelsen and Pejrup, 2001; Livsey et al., 2022). ~~, and bulk solid fraction~~

~~For each profile, we matched each~~ On the other hand, suspended sediment ~~sample (representing the~~data represent the size distribution and concentration of fully dispersed sediment grains~~) to a set of LISST measurements to obtain the coinciding in situ particle concentration and size distribution (representing the in situ suspended particles). For~~ , which might have been flocculated in situ. We paired each suspended sediment sample~~, we assigned all the LISST~~ from the concentration-depth profiles to a corresponding set of measurements from the concurrent LISST cast. LISST measurements were assigned when collected within 0.1 m (the sampler radius) of the sample collection depth. If there were no LISST measurements in this range, then we assigned the 3 ~~LISST~~ measurements closest in depth. ~~We combined the~~ We assumed that paired LISST and sediment data statistically represent the same suspended material, allowing direct comparison between the distributions and volume concentrations.

Figure 4 illustrates how we divided LISST particle sizes into three zones that either contain flocs only or both flocs and unflocculated grains to help isolate the floc and primary particle size distribution and concentration. Zone 1 is defined as particles measured by the LISST that were coarser than the maximum grain diameter of the dispersed sediment. We assume that all particles in zone 1 are flocs because they are larger than any dispersed sediment grains we measured. Zone 2 is defined as particles measured by the LISST that are finer than the floc cutoff diameter (Sect. 4.5; Fig. 3b). We inferred that particles in zone 2 were also flocs under the assumption that all sediment finer than the floc cutoff diameter was flocculated (Fig. 3b). In reality, some sediment finer than the floc cutoff diameter might have remained unflocculated. However, the enhanced settling velocities inferred from the concentration-depth profiles imply significant flocculation in these sizes, making complete flocculation a reasonable assumption. Finally, zone 3 lies between zones 1 and 2 and is defined as particles measured by LISST with sizes between the floc cutoff diameter and maximum grain diameter (Fig. 4). As such, zone 3 likely consists of a mixture of flocs and unflocculated grains.

Formatted: Font: 10 pt, Not Bold, English (United States)

Formatted: Font: Not Bold

Formatted: Heading 3

Formatted: Font: Not Bold

Formatted: Font: Not Bold

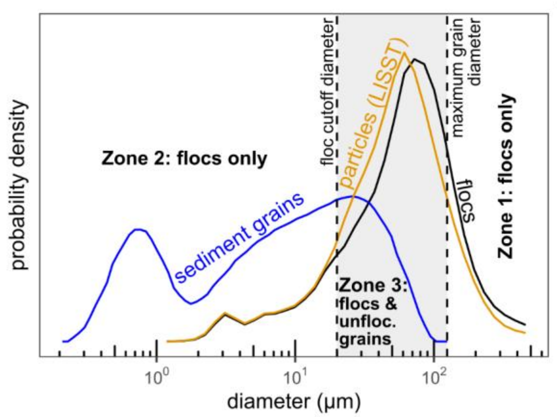

Figure 4: Example of calculating floc size distribution (black) from suspended sediment grain size distribution (blue) and LISST in situ particle size distribution (orange). Particles include flocs and unflocculated grains. Zones describe the particles in the LISST particle size distribution and are defined by the floc cutoff diameter and maximum grain diameter. We identified floc cutoff diameter as the grain diameter at which the Rouse-estimated settling velocity departs from settling velocity theory for single grains (Sect. 4.5). Maximum grain diameter is the maximum diameter of sediment grains measured by grain size analysis of fully dispersed sediment (Sect. 4.1). Data correspond to a suspended sediment sample collected at 1.9 m depth out of 3.8 m total depth from the GP spring 1 profile (Table 2).

We calculated the floc size distribution and concentration according to the LISST particle zones (Fig. 4). Floc concentration is the combined volume of primary particles and pores within flocs divided by the total measured volume. We used the volume concentration of sediment grains to compare the sediment and LISST concentrations because LISST reports particle volume concentration (Sect. 4.3). We calculated the LISST particle volume concentration in each LISST size class by multiplying the particle size fraction and the total particle concentration. We then calculated the corresponding sediment volume concentration by interpolating the grain size fraction to the LISST size class and multiplying by the total sediment concentration. According to our assumptions, LISST particle concentrations in zones 1 and 2 already represent floc concentrations and thus do not require any adjustment. This is not true in zone 3, so we calculated the floc concentration in each zone 3 size class by subtracting the particle and sediment volume concentrations. Finally, we renormalized the floc concentrations across size classes to compute the floc size distribution (Fig. 4). We calculated floc size distribution and concentration from each assigned LISST ~~measurements by taking the~~ measurement and averaged them to obtain the representative floc size distribution and concentration for each sediment sample. We took the floc diameter for each size class, D_{fi}, to be the geometric mean of the floc diameter at the lower and upper boundaries of the size class. For each concentration in each particle size class. For each -depth profile, we also composited the distributions over all samples to calculate calculated the depth-averaged distributions.

We removed the contribution of unflocculated sediment from the LISST particle size distributions, which measured both flocs and unflocculated sediment, to calculate floc size distributions (Table 1). We used the fact that sediment grains coarser than D_c are significantly unflocculated (Lamb et al., 2020; Nghiem et al., 2022). We identified D_c from the grain size-specific Rouse-Vanoni equation fitting results by eye (Sect. 4.4; Nghiem et al., 2022). For each LISST particle size class above the floc cutoff diameter, we calculated the volume concentration of unflocculated material in that class size distribution using the corresponding grain size distribution and sediment concentration (Sect. 4.1; Table 1). We subtracted the unflocculated concentrations from the LISST particle concentrations to isolate the floc volume concentration and normalized them to obtain floc size distributionstrapezoidal rule as described in Sect. 4.1.

We obtainedcomputed the primary particle volume concentration and size distribution usingand concentration by truncating the portion of the sediment grain size distribution and sediment volume concentrationto the fractions finer than the floc cutoff diameter (Table 1). We calculated the median Median primary particle diameter, $D_{p,50}$ (m), asis the median of the primary particle size distribution associated with each sediment sample. For the semi-empirical model (Eq. 7), we calculated the depth-averaged median primary particle diameter, $\widetilde{D}_{p,50}$, as the median grain size of the depth-averaged grain size distribution (Sect. 4.1) truncated with the floc cutoff diameter. We calculated the floc bulk solid fraction, $\bar{\varphi}$ (dimensionless), as the ratio of the primary particle and floc volume concentrations (e.g., Mikkelsen and Pejrup, 2001; Guo and He, 2011).

4.56.2 Fractal dimension, effective primary particle diameter,Dimension and drag ratioEffective Primary Particle Diameter

For each suspended sediment sample in the concentration-depth profiles, we identified the Our next goal was to estimate the fractal-related terms in the explicit model: fractal dimension, n_f, and effective primary particle diameter, D_p, for the integrated floc settling velocity across the floc size distribution to match the . Our strategy was to link both the explicit model (Eq. 1) and solid fraction theory (Eq. 2), in which n_f and D_p appear, to mean settling velocity (Table 1). The and solid fraction estimated from data. As follows, we solved for the n_f and D_p that ensure consistency between the bulk solid fraction and mean settling velocity and bulk solid fraction areover the floc size distribution (Sect. 4.6.1).

$$\overline{w_s} = \sum_{i=1}^{n} f_i w_{si}\,, \qquad (8a)$$

Estimating n_f and D_p requires two equations to calculate those two unknowns. The first equation is the bulk solid fraction over the floc size distribution using solid fraction theory (Eq. 2):

$$\bar{\varphi} = \sum_{i=1}^{n} f_i \left(\frac{D_{fi}}{D_p}\right)^{n_f-3} \sum_{i=1}^{n} \varphi_i = \sum_{i=1}^{n} f_i \left(\frac{D_{fi}}{D_p}\right)^{n_f-3}, \qquad (8b(9))$$

where f_i is the volume fraction in the i^{th} floc size class, from the floc size distribution, and n is the number of floc size classes (= 36), and $\overline{w_s}$ (m s^{-1})(36). We assumed that a single D_p applies across the floc size distribution, but primary particle diameter might vary with floc diameter (Nicholas and Walling, 1996). The second equation is the mean floc settling velocity over the floc size distribution using the explicit model (Eq. 1):

$$\overline{w_s} = \sum_{i=1}^{n} w_{si} = \sum_{i=1}^{n} f_i \frac{R_s g D_p^2}{b_1 \Omega_i \nu} \left(\frac{D_{fi}}{D_p}\right)^{n_f - 1}, \qquad (10a)$$

which we set equal to the explicit model settling velocity. For simplicity, we neglected inertial effects in the explicit model with mean values of input variables:

$$\overline{w_s} = \frac{R_s g \bar{\varphi} \overline{D_f}^2}{b_1 \bar{\Omega} \nu}, \qquad (10b)$$

where $\overline{D_f}$ (m) is the geometric mean floc diameter calculated from the floc size distribution and $\bar{\Omega}$ is the mean drag ratio. Although Eq. (9) and (10a) both use fractal solid fraction theory (Eq. 2), they represent distinct constraints because we calculated a typical floc Reynolds number of ~0.5, for which inertial effects are small (~5% increasethey integrate over different parameters (solid fraction in drag coefficient compared to the purely viscous model). As such, Eq. 9; settling velocity in Eq. 10). We substituted $\bar{\varphi}$ in Eq. (10b) with Eq. (9), set the resulting $\overline{w_s}$ follows the explicit model except with mean valuesequal to Eq. (10a), and rearranged terms to obtain:

$$\overline{w_s} = \frac{R_s g \bar{\varphi} \overline{D_f}^2}{b_1 \Omega \nu}, \qquad (9)$$

where $\overline{D_f}$ (m) is the mean floc diameter calculated logarithmically from the floc size distribution. We combined Eq. (8) and (9) to eliminate the unknown D_p and obtained

$$\frac{\sum f_i D_{fi}^{n_f-1}}{\sum f_i D_{fi}^{n_f-3}} \frac{\sum f_i \frac{\bar{\Omega}}{\Omega_i} D_{fi}^{n_f-1}}{\sum f_i D_{fi}^{n_f-3}} = \overline{D_f}^2, \qquad (10(11)$$

This approach assumes that a single D_p describes the primary particle diameter across the whole floc size distribution. In reality, the primary particle diameter probably varies with floc diameter (Nicholas and Walling, 1996), but the relationship is poorly known. For each sample, we solved Eq. (10) for fractal dimension with a root-finding algorithm and calculated the effective primary particle diameter using Eq. (8b) with the fitted n_f (Table 1).We assumed that the effect of $\bar{\Omega}/\Omega_i$ on the summation in Eq. (11) is small and neglected it (i.e., $\sum f_i (\bar{\Omega}/\Omega_i) D_f^{n_f-1} = \sum f_i D_f^{n_f-1}$). This assumption is justified because n_f estimates align well with typical n_f for natural flocs (Sect. 5.6). As such, n_f remains as the only unknown in Eq. (11) because the rest of the variables, f_i, D_{fi}, and $\overline{D_f}$, are all known from the floc size distribution (Sect. 4.6.1). We numerically solved Eq. (11) to calculate n_f for each sediment sample. We then solved Eq. (9) for D_p using f_i, n_f, and the known bulk solid fraction, $\bar{\varphi}$ (Sect. 4.6.1). We estimated uncertainty on floc concentration, n_f, and D_p as the 95% bounds on the bootstrap distribution from 1000 resamplingbootstrap replicates with replacement of resampling the matched set ofassigned LISST measurements (Sect. 4.5.1). We divided the floc settling velocity model prediction (Eq. 1 explicit model using the calculated D_p and n_f and setting $\Omega = 1$ and $b_1 = 20$) by the measured settling velocity for each floc cam observation to calculate Ω.that go into the floc size distribution and concentration (Sect. 4.6.1).

Formatted: Indent: First line: 0"

~~4.5.3 Testing effective primary particle diameter theory~~

~~We compared the calculated effective primary particle diameter and fractal primary particle diameter to~~ To test the fractal D_p model (Eq. ~~3). We evaluated the fractal D_p model using simulations of~~5), we compared its predictions to our effective primary particle ~~diameters contained within flocs~~diameter estimates. We used the number distribution, rather than the volume distribution, ~~of primary particle size~~to calculate the moments in Eq. (5) because ~~discrete~~primary particles are ~~the fundamental units in floc growth. For each suspended sediment sample, we~~ added one-by-one as flocs grow. We constructed the number distribution by dividing the volume fraction in each size class by the cube of the grain diameter and renormalizing ~~to ensure the fractions sum to 1. For~~the distribution.

4.6.3 Drag Ratio

The remaining parameter in the explicit model is the drag ratio, Ω. We solved the explicit model (Eq. 1) for Ω using n_f, D_p, and floc cam-measured floc diameter and settling velocity for each floc cam observation (Sect. 4.4). We used these Ω estimates to test permeability models presented in Sect. 2.1. For each permeability model, we identified the range of all possible Ω predictions as a function of fractal dimension, n_f, to test whether our Ω estimates fall within the range. If $D_f = D_p$, then the solid fraction is unity (Eq. 2) for all n_f leading to a maximum $\Omega = 1$ (i.e., impermeable floc). The minimum Ω, $\Omega_{\min}$, at a given n_f occurs at the maximal dimensionless permeability, $\xi_{\max}^{-2}$, because Ω and ξ^{-2} are inversely related (Eq. 3). Although $\xi_{\max}^{-2}$ depends on the permeability model, we present the Davies model only because the Brinkman model yielded similar results (Sect. 5.7). We differentiated the Davies model (Eq. 6) with respect to φ to find $\xi_{\max}^{-2}$ and, in turn, $\Omega_{\min} = \Omega(\xi^{-2} = \xi_{\max}^{-2})$ using Eq. (3):

$$\xi_{\max}^{-2} = \frac{1}{16}\left(\frac{1}{56}\frac{3n_f-5}{23-9n_f}\right)^{\frac{1}{3}\left(\frac{2}{3-n_f}-\frac{3}{2}\right)}, \qquad (12)$$

4.6.4 Floc Settling Velocity Distribution

To find the floc settling velocity distribution associated with each sediment sample, we used n_f, D_p, and Ω in the explicit model (Eq. 1) to convert the floc diameters in the floc size distribution into floc settling velocities. In this calculation, we used a best-fit constant drag ratio (Sect. 5.7), $\Omega = 0.51$, because we were unable to constrain Ω for concentration-depth profiles that lack floc cam observations. For the bins at the fine tail in which $D_{fi} < D_p$, we capped the solid fraction at 1 (Eq. 2) to ensure physically meaningful results. We took the floc settling velocity for each ~~sample, we simulated 10,000 flocs each containing a number of primary particles determined by fractal theory, $n_p = (D_f/D_p)^{n_f}$ (Kranenburg, 1994) where n_p is the number of primary particles in a floc. For each iteration, we first sampled a floc diameter from the number-based floc size distribution. Using the fitted n_f and D_p, we calculated and sampled n_p primary particle diameters from the number-based primary particle size distribution. We summarized the sampled primary particle diameters using Eq. (3) and the median and then further summarized each set of primary particle diameters with a volume-weighted mean. Equation (3) is limited because the number~~

of primary particles in a floc must class, w_{si}, to be known. As such, we tested a simplified fractal model in which we assumed the number of primary particles is sufficiently large for the central limit theorem to apply, yieldingthe geometric mean of the floc settling velocity at the lower and upper boundaries of the class. For each concentration-depth profile, we calculated the depth-averaged floc settling velocity distribution using the trapezoidal rule as described in Sect. 4.1.

$$D_p = \left(\overline{D_p^3} / \overline{D_p^{n_f}}\right)^{1/(3-n_f)}, \tag{11}$$

where the overbars denote taking the mean of the distribution (Gmachowski, 2003).

4.6 Geochemical Measurements

We measured the Al/Si and total organic carbon (TOC) of sediment and major ion concentrations and dissolved inorganic carbon (DIC) concentration of river water to calculate Al/Si, θ, and Φ in the semi-empirical model following Nghiem et al. (2022). We measured sediment Al/Si using X-ray fluorescence (XRF) for 33 samples (Appendix A). We calibrated a model between grain size and Al/Si ($R^2 = 0.88$) and used it to calculate Al/Si for each concentration profile using the depth-averaged grain size distribution (Fig. A1). We measured TOC in the suspended sediment samples to calculate θ. The sediment samples were leached with 2 M HCl at 80°C to remove carbonate and then oven-dried. TOC content was measured on the decarbonated samples using an Exeter Analytical CHN analyzer with uncertainties determined from repeat measurements of reference materials. Samples were weighed before and after decarbonation to determine the fraction of sediment mass lost during decarbonation. This fraction was used to convert the raw measured TOC concentrations to the corrected values for pre-decarbonated samples. We assumed the organic matter is cellulose to convert TOC concentration to organic matter concentration (Nghiem et al., 2022).

We used ion chromatography and cavity ring-down spectroscopy to measure the major ion concentrations (cations: Na^+, K^+, Ca^{2+}, Mg^{2+}; anions: Cl^-, HCO_3^-, SO_4^{2-}) of water samples as inputs to calculate Φ. Major cation (Na^+, K^+, Ca^{2+}, Mg^{2+}) and anion (Cl^-, SO_4^{2-}) concentrations were measured by ion chromatography at Durham University (Geography Department) and checked by regular measurements of the LETHBRIDGE-03 standard. The dissolved inorganic carbon (DIC) concentration was determined using a Picarro Cavity-Ring Down Spectroscopy (CRDS) G2131-*i* coupled to a modified AutoMate autosampler. About 6 mL of filtered river water was injected through a 0.2 µm syringe filter into an evacuated and pre-weighed 12 mL AutoMate exetainer. The AutoMate acidified the samples with 10% phosphoric acid. The resulting CO_2 was carried in a nitrogen stream into the Picarro CRDS for total carbon measurements (Dong et al., 2018). DIC concentration was calibrated against weighed optical calcite standard reference materials that were acidified in evacuated exetainers with 10% phosphoric acid overnight. We assumed that all DIC was HCO_3^- to convert the measured DIC concentrations to HCO_3^- concentrations. We solved for the HCO_3^- concentration using charge balance for cases in which we had ion chromatography measurements, but did not measure DIC concentration.

5 Results

First, we describe the basic hydrodynamics, sediment properties, and floc observations from the individual measurement methods (Sect. 5.1-5.4). ~~Then, we analyze the~~We then present floc variables derived from combining data sources (Sect. 5.5-5.8). We compare effective primary particle diameter and drag ratio ~~in the explicit model. To this end, we combine results from the multiple floc methods to derive floc variables (Sect. 5.5 and 5.6), which we use to estimate the effective primary particle diameter and drag ratio, compared them~~ to theory~~,~~ and validate them using floc settling velocity inferred from the Rouse-Vanoni equation fitting (Sect. 5.6-5.~~8~~9). Finally, we validate the semi-empirical model and use it ~~as a framework~~ to examine ~~the~~ environmental ~~factors responsible for the observed~~controls on floc properties ~~in WLD~~ (Sect. 5.~~9~~10).

5.1 Hydrodynamics

The sampled profiles span a wide hydrodynamic range in WLD because of discharge seasonality and environment (Fig. 1d; Table 2). The fastest flow occurred at site WO in the spring (~1.5 m s^{-1} depth-averaged) ~~far~~ upstream of the delta apex in the Wax Lake Outlet, where the water depth was ~~also the~~ greatest (30 m) among the ~~sampled~~ sites. Further down the delta, the distributary channel site GP had slower flow velocity (~0.~~58~~56 m s^{-1} depth-averaged in the spring) and shallower depth (~3 ~~to 4~~.7 m). At site GP, ~~the~~ depth-averaged flow velocity in ~~the~~ summer was about half (~0.2 to 0.3 m s^{-1}) of that in ~~the~~ spring ~~because of the discharge seasonality~~ (Fig. 1d). The island sites were sampled in the spring only. These sites had the slowest flow velocities (0.024 and 0.~~11~~12 m s^{-1}) out of the sampled sites ~~because the flow was unchannelized (~~with water ~~depth~~depths of ~0.6 m~~). The shear~~. Shear velocity generally increased with ~~the~~ flow velocity, ranging from ~0.~~3~~006 (in the island) to ~~~9 cm~~0.1 m s^{-1} (in Wax Lake Outlet ~~during spring high-flow conditions). The~~). Near-bed Kolmogorov microscale varied inversely with the shear velocity from ~~260~~130 to ~~1300~~590 μm. Water chemistry measurements show a median salinity of 0.25 ppt and a maximum of 0.29 ppt, confirming that the water was fresh (< 0.5 ppt).

Table 2: Metadata and hydrodynamic data of sampled profiles. Boldface profile name indicates that we collected floc cam images for the profile. Shear velocity uncertainty indicates the 95% confidence interval on the law of the wall fit (Sect. 4.1).

Profile name (Site + season + index)	Date (yyyy-mm-dd)	Number of suspended sediment samples	Water depth (m)	Depth-averaged flow velocity (~~c~~m s^{-1})	Shear velocity (~~c~~m s^{-1})	~~Depth-averaged~~Near-bed Kolmogorov microscale (μm)	Depth-averaged suspended sediment volume concentration (×10^{-5})

Formatted Table

GP spring 1	2021-03-27	8	3.8	~~58~~0.55	~~5.6 ±~~ 0.~~03~~081 ± 0.012	~~260~~130	5.2
WO spring	2021-03-30	4	30	~~150~~1.5	~~9.2 ±~~ 0.~~006~~097 ± 0.0096	~~290~~200	~~7.3~~6.9
M2 spring	2021-04-02	4	0.64	~~11~~0.12	~~1.7 ±~~ 0.~~07~~028 ± 0.013	~~400~~200	~~5~~7.3
M1 spring	2021-04-02	4	0.59	~~2.4~~0.024	0.~~34~~0063 ± 0.~~08~~0026	~~1300~~590	4.7
GP spring 2	2021-04-02	4	3.5	~~58~~0.57	~~4.8 ±~~ 0.~~03~~058 ± 0.012	~~280~~170	~~5.7~~6.2
GP summer 1	2021-08-18	4	3.4	~~26~~0.22	~~3.2 ±~~ 0.~~04~~029 ± 0.012	~~380~~290	0.~~73~~69
GP summer 2	2021-08-20	5	3.4	~~32~~0.34	~~1.6 ±~~ 0.~~06~~020 ± 0.0062	~~640~~390	0.~~61~~54
GP summer 3	2021-08-22	10	3.2	~~23~~0.25	~~2.4 ±~~ 0.~~02~~017 ± 0.0047	~~470~~420	0.61

5.2 Sediment Concentration-~~depth profiles~~Depth Profiles

~~The concentration-depth profile results inform the concentrations, grain size distributions, and flocculation state of the suspended sediment. In general, the depth~~Depth-averaged suspended sediment ~~is~~was muddy (~90% mud ~~by volume~~) and more concentrated in the spring (~~~5 to 7~~6×10^{-5} volume concentration) than in the summer (~~~5 to~~ 6×10^{-6}) because of ~~the~~ discharge seasonality (Table 2).

The grain size-specific ~~sediment~~ concentration-depth profiles reveal ~~a stratification trend of~~ higher concentration closer to the bed for ~~both mud and~~ sand ~~grain size classes~~, a pattern consistent with ~~the~~ Rouse-Vanoni ~~equation~~theory (Eq. 8; Fig. 3a).~~7).~~ ~~Figure 3a shows an example of the grain size-specific profiles for the profile GP spring 1. Sand tended to be more~~ Mud was also stratified ~~than mud, with the coarsest sand (~ 100 to 200 μm) so severely stratified that it was effectively absent in samples~~

Formatted: Indent: First line: 0"

higher in the water column. Mud was appreciably stratified compared todespite the expectation of a nearly uniform concentration profile from the Rouse-Vanoni equation for the slowly settling unflocculated mud. The vertical variability is depth profile if mud settled as individual grains (Eq. 8), indicating likely due to natural variability in sediment concentration and the fact that we collected samples over a period of 40 to 60 min (Fig. flocculation.3a).

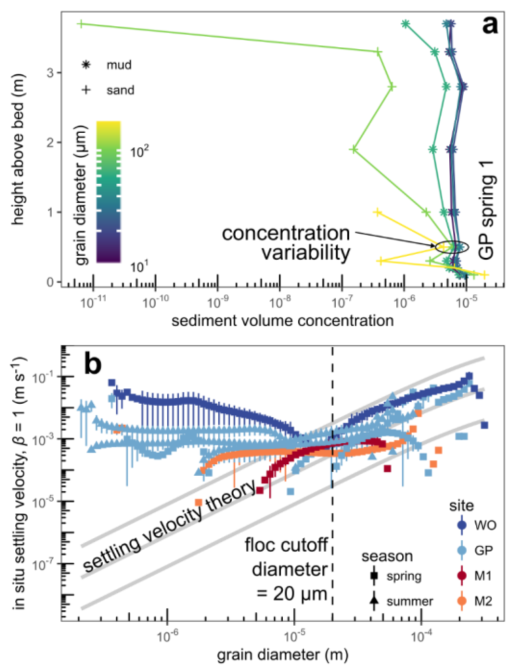

Figure 3: Rouse-Vanoni equation inversion results for profiles with paired suspended sediment samples and LISST measurements. (a) Example of sediment volume concentration as a function of height above bed for profile GP spring 1. We used the full 100 grain size classes in all calculations, but reclassified the data into 6 classes for this panel only to improve readability. The relatively high concentration at 0.5 m above the bed is an example of natural sediment concentration variability. (b) Grain diameter and Rouse-estimated in situ settling velocity using $\beta = 1$. The gray settling velocity theory curves indicates the Ferguson and Church (2004) model with an order-of-magnitude above and below. Vertical bars represent the propagated 68% confidence interval on the Rouse number estimates. Points without vertical bars have confidence intervals that overlap with 0.

Formatted: Font: 10 pt, Not Bold, English (United States)

The grain diameter versus in situ settling velocity trend from the Rouse-Vanoni equation fitting shows that sediment finer than ~20 µm (i.e., the floc cutoff diameter) was appreciably flocculated at the eight main sample profiles (Fig. 3b), assuming that the sediment and floc diffusivity ratios are unity. This floc cutoff diameter indicates the grain diameter at which the in situ mud; Table 1). Enhanced settling velocity departs from settling velocity theory prediction ($w_s = (R_s g D^2)/(c_1 \nu + \sqrt{0.75 c_2 R_s g D^3})$ for grain diameter, Din the grain sizes, $c_1 = 20$, and $c_2 = 1.1$; Ferguson and Church, 2004). The faster in situ velocity (than the prediction) in the sediment finer than the floc cutoff diameter is consistent with the results of Lamb et al. (2020) and Nghiem et al. (2022) indicating that and indicates the presence of flocculation is responsible.. Conversely, the in situ settling velocity follows settling velocity theory well for grain diameterdiameters larger than about 20 µm and indicates that this coarser sediment is not substantially flocculatedthe absence of flocculation. Although the $\beta = 1$ assumption makes the precise in situ settling velocity values inaccurate, we expect the floc cutoff diameter to be robust because it marks an abrupt change in the settling velocity pattern. We used 20 µm as the floc cutoff diameter to calculate floc size distributions for this set of profiles with corresponding LISST measurements (Sect. 4.5(Sect. 4.6.1).

5.3 LISST Particle Size Distribution and Concentration

The combined size distributions and concentrations of flocs and unflocculated sediment (i.e., in situ particles) from LISST profiles indicate limited vertical variation of median To demonstrate results prior to additional processing (Sect. 4.6.1), Figure 5 shows the raw LISST-measured in situ particle diameter and concentration, but the much larger median particle diameter compared to median grain diameter (3 to 30 times) supports the occurrence of flocculation (Fig. 4). The channel sites (WO and GP) had median particle diameters of ~50 to 90 µm, while the island sites (M1 and M2) had median particle diameters of ~35 µm (Fig. 4a). Although the vertical variation in total particle concentration was broadly limited, concentration and size distribution observations. The concentration profiles of flocs and unflocculated sediment (i.e., in situ particles) measured by LISST had little systematic vertical variation except for the site GP profiles in the spring in which the concentration increased slightly towardcloser to the bed in some profiles (Fig. 4b5a). In the spring, the particle volume concentration was about ~3×10^{-4} to 5×10^{-4} for all sites except for the site M1, which had a slightly smaller concentration of ~2×10^{-4} to 3×10^{-4}. In the summer, the particle volume concentration at site GP was much smaller, ~ at ~5×10^{-5} to 8×10^{-5}, because of the smaller summerrelatively lower discharge. However, the depth

Channel sites (WO and GP) had median particle diameters of ~50 to 90 µm, while island sites (M1 and M2) had median particle diameters of ~35 µm, all with minimal vertical variation (Fig. 5b). Depth-averaged particle size distributions were similar across the channel sites for both the spring and summer (Fig. 4c). Thewhile the island distributions were skewed toward finer particles. (Fig. 5c). The fraction of particles coarser than the floc cutoff diameter ranges(20 µm for these profiles) ranged from ~0.6 to 0.85, indicating that the concentration in most LISST size classes might need to be corrected for unflocculated sediment to retrieve the floc concentration and size distribution.. The median depth-averaged particle diameter

Formatted: English (United States)

Formatted: Superscript

Formatted: Indent: First line: 0.5"

from the LISST ranges from about 3 to 30 times larger than the median grain diameter ~~(Fig. 4d), an effect that we attribute to~~of the dispersed sediment (Fig. 5d), implying the presence of flocculation.

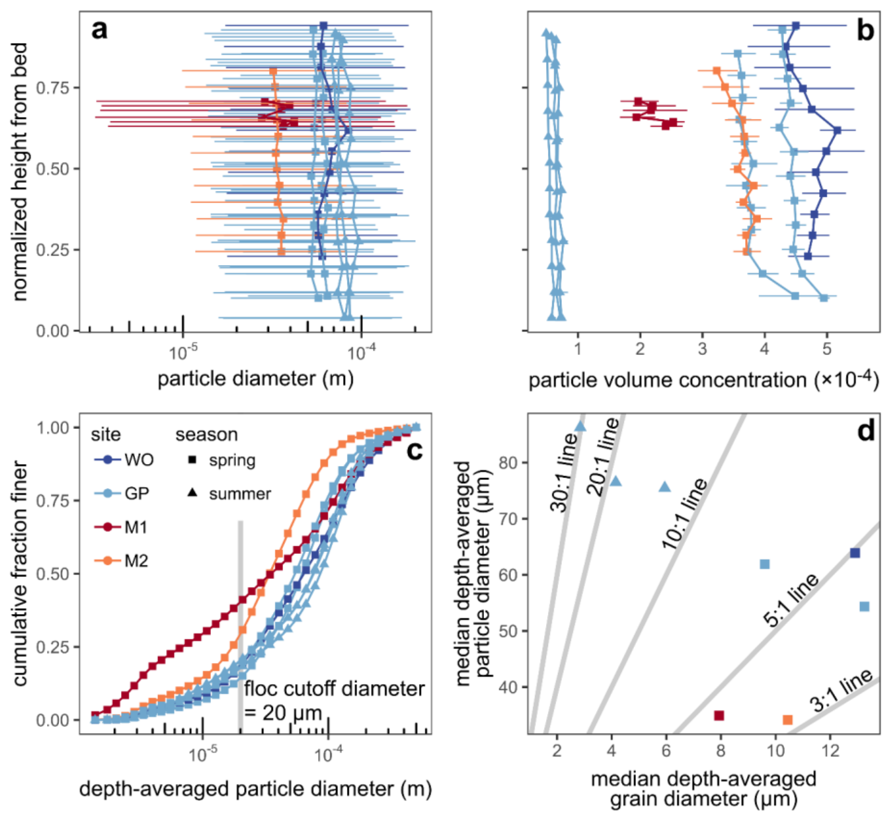

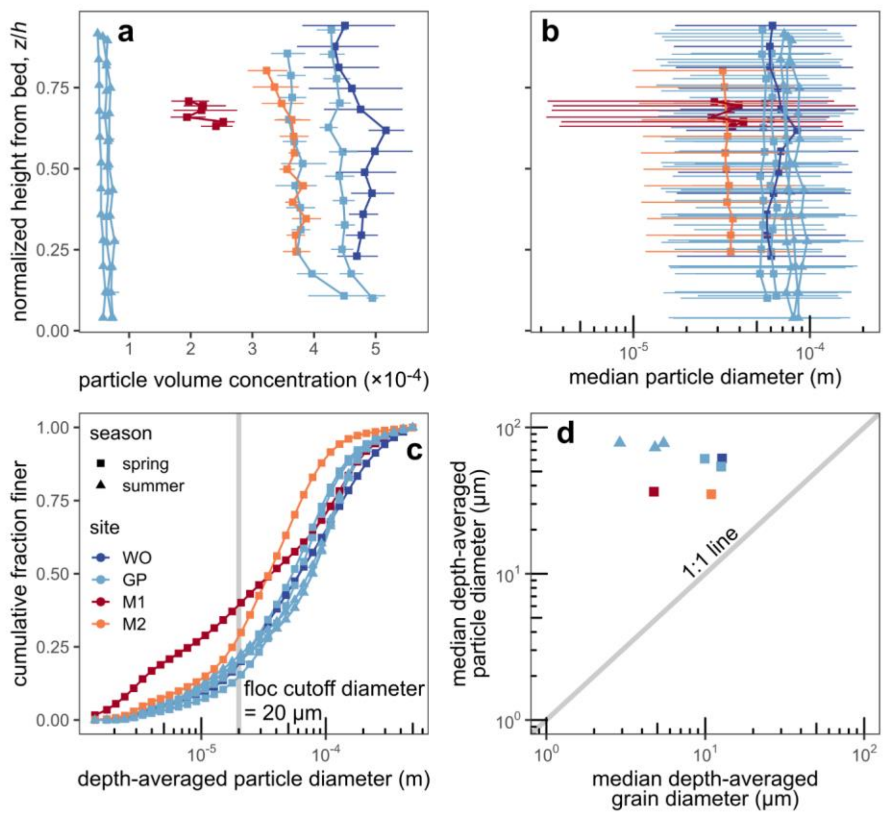

Figure 45: LISST results. for in situ particles, which include flocs and unflocculated sediment. (a) Profiles of in situ particle diameter. Pointsvolume concentration from LISST, binned into 12 vertical classes. Horizontal bars represent the 95% bootstrap uncertainty. (b) Profiles of median in situ particle diameter from LISST, binned into 12 vertical classes. Horizontal bars represent the span of the D_{16} and D_{84} particle diameters, the diameters for which 16% and 84% of particles are finer, respectively. (b) Profiles of in situ particle volume concentration. Horizontal bars represent the 95% bootstrap uncertainty. (c) Cumulative distribution functions of depth-averaged particle diameter from LISST. (d) Scatterplot of median grain diameter from sediment samples and median particle diameter from LISST. The legend in panel c applies for all panels.

5.4 Floc Cam

~~We extracted direct measurements of particle diameter and settling velocity from the~~ Tracked particles imaged by floc cam ~~images, with~~had diameters of ~70 to 200 μm and settling velocities of ~0.1 to 1 mm s^{-1}~~. We could not verify visually from the images whether the~~ (Fig. 6), but we did not know a priori whether these particles were flocs because the image quality did not permit a visual determination. To test whether tracked particles were flocs, ~~so we compared the relationship between~~Figure 6 compares diameter and settling velocity ~~measurements to~~because, unlike flocs, solid grains follow conventional settling velocity theory ~~for solid grains~~ (Ferguson and Church, 2004). ~~For~~We concluded that tracked particles were flocs because, for a given diameter, ~~the~~ measured settling velocities are slower than ~~the~~ settling velocity predictions of solid grains ~~as expected because~~ due to the fact that flocs are ~~porous and hence~~ less dense than sediment ~~(Fig. 5). Conversely, the measured floc~~grains. Measured settling velocities also are about one order-of-magnitude faster than the predicted settling velocity of a typical 5-μm mud primary particle~~. These comparisons confirm that the tracked particles were indeed flocs. The floc cam data show the expected trend of increasing floc settling velocity with floc diameter (Eq. 1), but there is considerable scatter probably because of density variations and inherent stochasticity of~~, also indicating flocculation ~~(see discussion in Strom and Keyvani, 2011).~~.

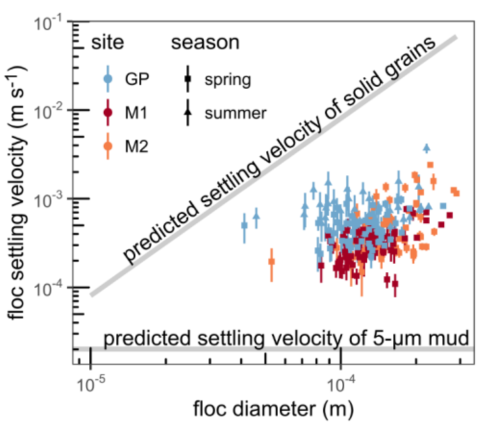

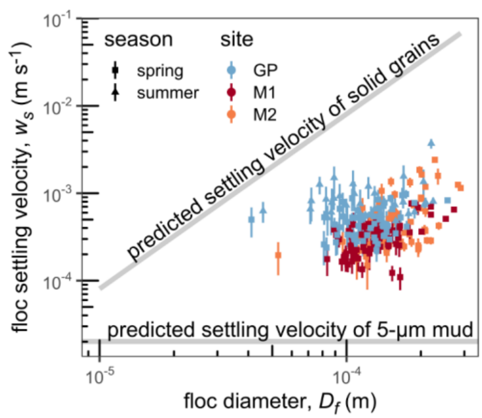

Figure ~~5: Floc cam-measured floc diameter~~6: Diameters and ~~floc~~ settling ~~velocity~~velocities of floc cam-measured particles, which we inferred to be flocs. Vertical bars indicate the propagated mean standard error on the background displacement estimate (Sect. 4.~~3~~4).

5.5 Floc Concentration, Size Distribution, and ~~Concentration~~Bulk Solid Fraction

~~We combined the individual data sources (~~As described in Sect. ~~5~~4.6.1~~-5.4) to compute floc variables, starting here with the floc~~, we paired concentration and size distribution~~. We assumed that the LISST particle concentration and size distribution (Sect. 5.3) include unflocculated~~ data for sediment and in ~~the~~situ particles ~~coarser than the floc cutoff diameter of 20 µm (Sect. 5.2). Thus, we removed the sediment concentration coarser than 20 µm from the LISST particle size distributions and concentrations~~ to isolate the floc concentration and size ~~distributions and concentrations~~distribution (Table 1).

~~The floc data show limited vertical variation of median diameter and concentration (similar to the raw LISST results) and indicate that flocs were ~1 to 100 µm in diameter and predominately smaller than the Kolmogorov microscale. The total floc concentration varied most substantially with discharge and sediment flux seasonality (Fig. 6a). The floc volume concentration was ~3~~ Floc volume concentration was ~3×10^{-4} to 5×10^{-4} for the sites in the spring except for site M1, which had a smaller concentration of ~2×10^{-4} to 3×10^{-4}~~.~~ (Fig. 7a). All floc concentrations in the summer were far smaller than the concentrations in the spring at ~5×10^{-5} to 8×10^{-5}~~. The median floc diameter, $D_{f,50}$ (m), was ~50 to 90 µm for the channel sites and ~35 µm for the island sites with little vertical variation (Fig. 6b). The floc and raw LISST results~~ because of the relatively lower discharge. These concentration trends are similar ~~because flocs composed most of the particle volume concentration. This is evident from the fact that the floc concentration far exceeds the primary particle concentration (order 10^{-4} versus 10^{-5}, respectively), implying the floc bulk solid fraction was ~0.1, which is typical for highly porous natural flocs (McCave, 1984; Gibbs, 1985; Eq. 2). We revisit the solid fraction in Sect. 5.7. The depth-averaged floc size distributions at the channel sites were similar for spring and~~

Formatted: Indent: First line: 0"

~~summer. In contrast, the floc size distributions at the two island sites were skewed toward finer flocs (Fig. 6c). Almost all flocs were smaller than the depth-averaged Kolmogorov microscale (Fig. 6d), a result consistent with the idea that the Kolmogorov microscale sets the maximum floc size (Van Leussen, 1988; Kuprenas et al., 2018~~to those for the particles (Sect. 5.3).

Formatted: English (United Kingdom)

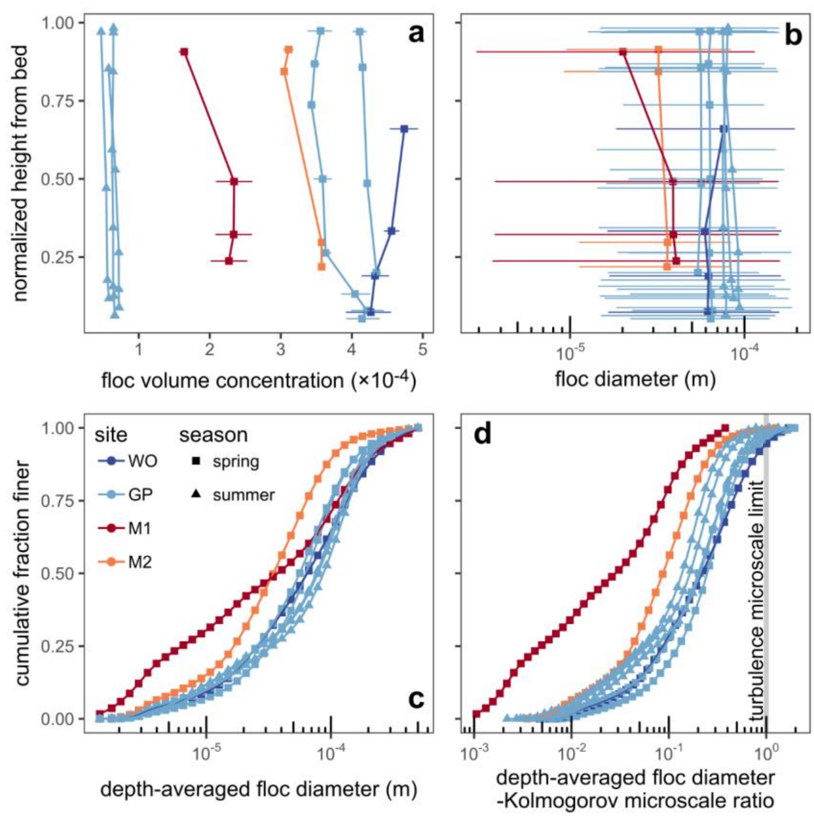

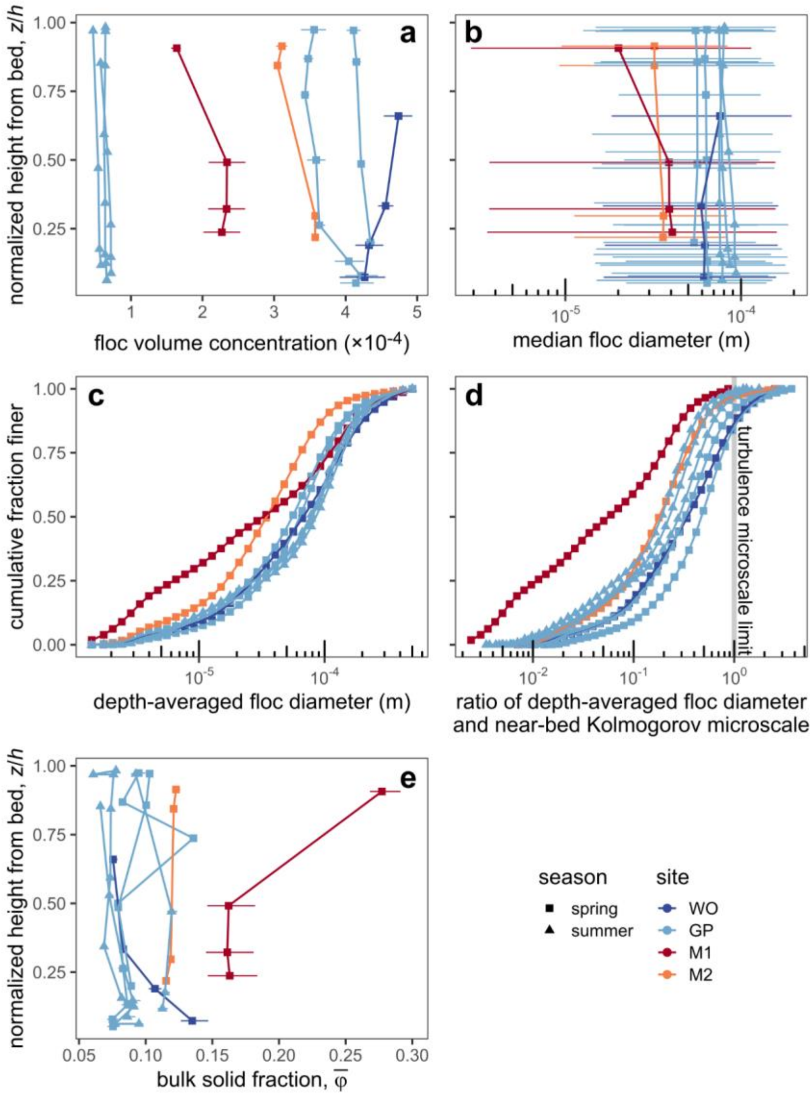

a
b
c
d
e
normalized height from bed, z/h
floc volume concentration (×10-4)
median floc diameter (m)
cumulative fraction finer
depth-averaged floc diameter (m)
ratio of depth-averaged floc diameter
and near-bed Kolmogorov microscale
turbulence microscale limit
bulk solid fraction, φ
season
spring
summer
site
WO
GP
M1
M2

820

Figure 67: Floc volume concentration, size, and diameterbulk solid fraction results. (a) Profiles of floc volume concentration. Horizontal bars represent the 95% bootstrap uncertainty. (b) Profiles of floc diameter. Points represent the median floc diameter. Horizontal bars represent the span of the D_{16} and D_{84} floc diameters. (c) Cumulative distribution functions of depth-averaged floc diameter. (d) Cumulative distribution functions of the ratio of depth-averaged floc diameter and near-bed Kolmogorov microscale. The legend in panel c applies for all panels(e) Profiles of bulk solid fraction. Horizontal bars represent the 95% bootstrap uncertainty.

Median floc diameter, $D_{f,50}$ (m), was ~50 to 90 µm for channel sites and ~35 µm for island sites with little vertical variation (Fig. 7b). Overall, flocs were ~1 to 100 µm in diameter (Fig. 7c). Depth-averaged floc size distributions at the channel sites were similar for spring and summer (Fig. 7c). In contrast, the floc size distributions at the island sites were enriched in finer flocs. About 85 to 100% of flocs (by volume) were smaller than the near-bed Kolmogorov microscale (Fig. 7d), consistent with the idea that the Kolmogorov microscale sets the maximum floc size (Van Leussen, 1988; Kuprenas et al., 2018). Flocs larger than the near-bed Kolmogorov microscale might either break up once they reach the elevated near-bed shear stress or, if they are sufficiently strong, withstand breakage and deposit on the bed (Mehta and Partheniades, 1975). Floc size distributions yield a typical floc Reynolds number of 0.5, indicating minor inertial effects and justifying neglect of the inertial term in the explicit model (Strom and Keyvani, 2011).

After isolating the primary particle and floc volume concentrations (Sect. 4.6.1), we took the ratio of the concentrations as the floc bulk solid fraction. Bulk solid fraction ranged from ~0.05 to 0.3, but mostly smaller than 0.15, and showed little systematic vertical variation (Fig. 7e). Bulk solid fraction in the island was typically higher (> 0.15 at M1; > 0.1 at M2) than that in the channel (< 0.1) because flocs in the island were finer (Fig. 7bc) and hence denser (Eq. 2) than those in the channel. Overall, these bulk solid fractions agree with prior floc density measurements (e.g., Van Leussen, 1988).
5.6 Fractal dimension and effective primary particle diameter

Next, we derived two key parameters of the explicit model,

5.6 Fractal Dimension and Effective Primary Particle Diameter

Figure 8a displays fractal dimension, n_f, and effective primary particle diameter, D_p, two key explicit model parameters that we derived using the floc size distribution and bulk solid fraction (Sect. 5.54.6.2; Table 1). We computed n_f and D_p to ensure consistency between the mean floc settling velocity and bulk solid fraction under fractal theory across the floc size distribution (Sect. 4.5.2; Table 1).

The fitted fractal dimension is narrowly constrained to ~2 to 2.15, which is well within the expected range of 1.7 to 2.3 for natural flocs (Fig. 7a; Tambo and Watanabe, 1979; Winterwerp, 1998). We deemed $n_f = 2.1$ to be representative for WLD flocs. Fractal dimension correlates strongly with median floc diameter despite the small range of fractal dimension (Fig. 7a), but the reason for the correlation is unclear. Some studies proposed that fractal dimension decreases with the ratio of floc and primary particle diameters, $D_{f,50}/D_{p,50}$ (Khelifa and Hill, 2006; Maggi et al., 2007; Kumar et al., 2010). In contrast, we found that the fractal dimension increases with $D_{f,50}/D_{p,50}$ according to a small, albeit statistically significant, power (p-value

855 = 8.7×10^{-5}; Fig. 7b)., Smaller n_f in the island compared to that in the channel might indicate floc restructuring in response to changes in factors like turbulence, sediment concentration, organic matter, and water chemistry. Effective primary particle diameter, D_p, is tightly constrained to ~2 μm with a range of ~1 to 3 μm. No clear trend is apparent between n_f and D_p.

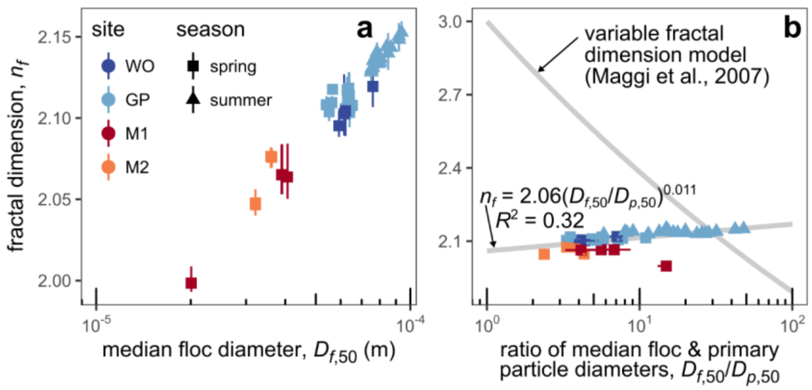

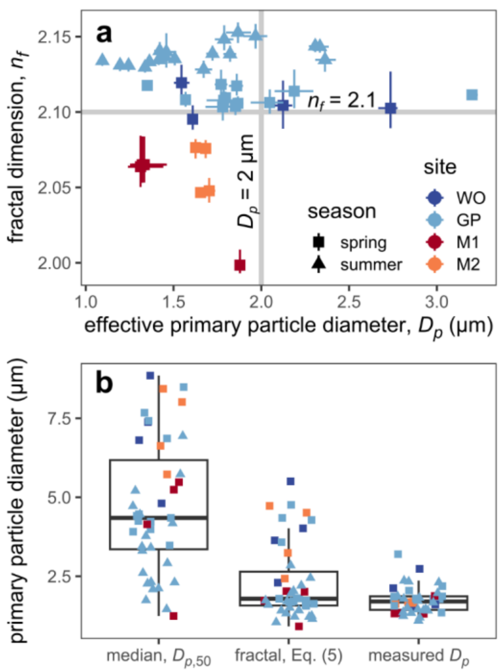

Figure ~~7: Fractal dimension results.~~8: (a) Fractal dimension and ~~median floc~~effective primary particle diameter. Horizontal and vertical bars represent the 95% bootstrap uncertainty. Bars are smaller than the points where they are not visible. (b) ~~Ratio of median floc and~~Effective primary particle ~~diameters and fractal dimension~~diameter, D_p, model comparison. We ~~used the~~calculated median primary particle ~~diameter, $D_{p,50}$, not the fitted effective~~diameters from primary particle ~~diameter for consistency with past studies. Horizontal and vertical bars represent the 95% bootstrap uncertainty.~~size distributions (Sect. 4.6.1). We calculated fractal D_p using Eq. (5) on number-based primary particle size distributions (Sect. 4.6.2). Measured D_p were estimated from data (Sect. 4.6.2).

We ~~tested two models for the effective primary particle diameter,~~ compared our D_p~~: (1) the~~ estimates, fractal ~~model~~D_p predictions (Eq. ~~3~~5), and ~~11) and (2) the~~ median primary particle ~~diameter, $D_{p,50}$. The fitted~~ diameters, $D_{p,50}$, to test whether the fractal model or the median better predicts the effective primary particle diameter (Fig. 8b). Figure 8b shows that the fractal D_p model reasonably reproduces measured effective primary particle ~~diameter is tightly constrained to ~2 µm with a range of ~1 to 3 µm (Fig. 8). To predict D_p, the full fractal model (Eq. 3; Bushell and Amal, 1998) requires knowledge of all primary~~

Formatted: Indent: First line: 0.5"

particle diameters within a floc. We simulated them by random draws from the primary particle size distribution (Sect. 4.5.3). The good agreement between the simulated and measured median primary particle diameter validates the simulation method (Fig. A2a). Alternatively, the fractal model can be simplified to depend directly on moments of the primary particle size distribution (Eq. 11). We used the simple form (Eq. 11) as the fractal model because it yields very similar predictions to the simulation results of the full model (Fig. A2b). The fitted primary particle diameters, D_p, in contrast to the median assumed in past studies (e.g., Syvitski et al., 1995; Strom and Keyvani, 2011). D_p values are about a factor of 2 on average (and up to a factor of 6) smaller than the median, indicating that the median is a poor representation of the effective primary particle diameter (Fig. 8a). The fractal model better predicts the effective primary particle diameter (Fig. 8b), supporting the hypothesis that, in the case of many primary particle sizes, D_p should be specified to satisfy fractal constraints. HoweverD_p. But in some cases, the fractal model still overestimates D_p by a factor of about 2- to 3 in some cases. Potential error in converting a volume-based size distribution to a number-based distribution might be responsible for the misfit. Nevertheless, the fractal model predicts a range more representative of the effective primary particle estimates than the median (Fig. 8c). If one assumed D_p is the median, then one would overestimate the solid fraction and floc settling velocity by a factor dependent on the fractal dimension (Eq. 1 and 2). In our data, this overestimation factor ranges from 1 (no effect) to 5 and has a median of 2.2 (Fig. 8d).

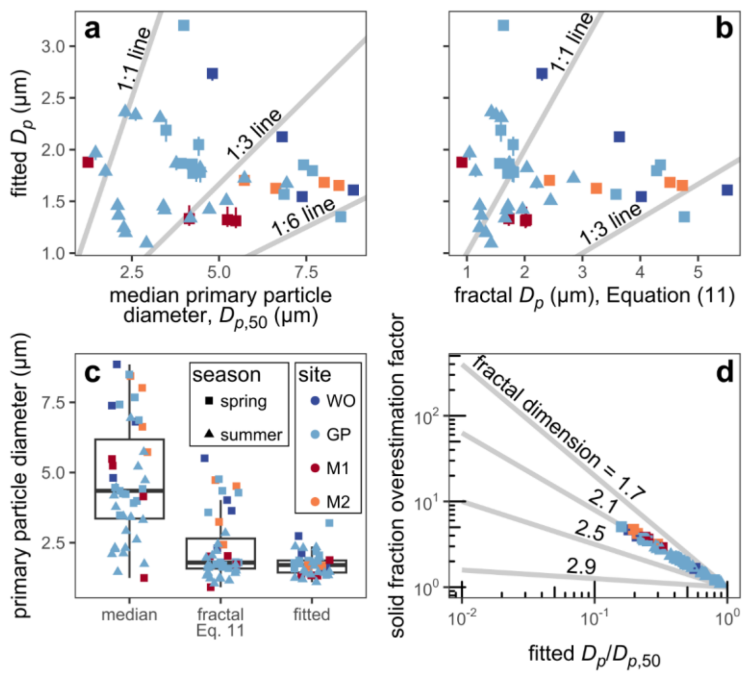

890

~~**Figure 8: Effective primary particle diameter, D_p, results from primary particle size distributions (Sect. 4.5.1), fitted D_p (Sect. 4.5.2), and the fractal D_p model (Sect. 4.5.3). (a) Median primary particle diameter and fitted effective primary particle diameter. Vertical bars indicate the 95% bootstrap uncertainty on the fitted effective primary particle diameter. (b) Fractal (Eq. 11) and fitted effective primary particle diameters. (c) Boxplots of primary particle diameters. For each boxplot, the lower, central, and upper hinges indicate the 25, 50, and 75th percentiles, respectively. (d) Ratio of fitted effective and median primary particle diameters and the solid fraction overestimation factor. The lines represent contours of constant fractal dimension. The legend in panel c applies to all panels.**~~

~~**5.7 Drag ratio, floc solid fraction, and settling velocity distribution**~~

5.7 Drag Ratio

We estimated the final unknown in the explicit model, the drag ratio, Ω, ~~as the ratio of~~ by solving the explicit model ~~settling velocity (~~(Eq. 1) with ~~fitted~~ n_f, D_p, ~~and Ω = 1)~~ and floc cam-measured diameter and settling velocity (Sect. 4.~~5.2~~6.3; Table 1~~)~~ ~~and evaluated the values against floc permeability theory. The best-fit constant Ω is 0.51 with lower and upper error~~). Overall, Ω estimates ~~of 0.39 and 0.71, respectively,~~span a wide range from ~0.15 to 1 (Fig. 9a), indicating ~~substantial~~that permeability enhances floc settling velocity and reduces floc drag force ~~reduction due to permeability (Fig. 9a).~~by up to a factor of 7. High variability in Ω exists even within the same floc cam deployment. Although some Ω values exceed 1, ~90% of the data fall between 0 and 1 indicating that our estimates are physically reasonable.

~~We compared drag ratio estimates initially to two models, the Brinkman model (Eq. 4) and the Li and Logan modification of the Brinkman model. The Brinkman model, which assumes uniform porosity and a single primary particle size, is incompatible with the data because ~92% of the data (excluding Ω > 1 data) lie below the predicted minimum Ω (i.e., maximum permeability) for the given n_f (Fig. 9a). The Li and Logan variant (Sect. 2.1), which uses a larger cluster diameter, D_c, in place of the effective primary particle diameter, also cannot explain the data because replacing D_p with D_c does not alter Brinkman's minimum Ω, which is solely a function of n_f. Instead, we propose a new empirical "permeable cluster model," in which we preserve the original solid fraction in the Brinkman model (unlike Li and Logan), but use D_c instead of D_p in the diameter ratio term (like Li and Logan). The model is so named because it implies that the clusters are themselves permeable (Sect. 6.2). We calculated D_c for each drag ratio estimate to test the permeable cluster model. Differences in the cluster diameter can explain the full variability in the relationship between the solid fraction and drag ratio (Fig. 9b). In contrast, the Brinkman model, setting fractal dimension to 2.1, predicts drag ratio very close to 1 (impermeable floc) across all solid fractions and is inconsistent with the data. The ratio of cluster and floc diameters, D_c/D_f, has a median of 0.11 and 16th and 84th percentiles of 0.047 and 0.22. However, the permeable cluster model is limited because we could not determine how to predict D_c.~~

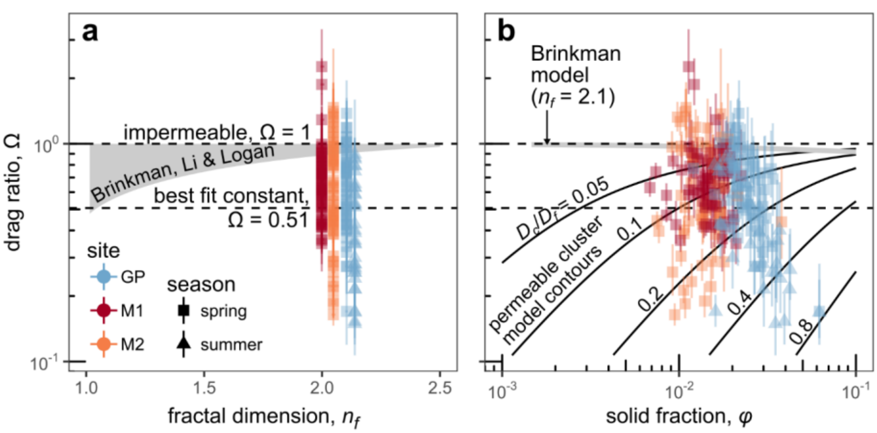

We used our Ω measurements to test the ability of permeability models to predict drag ratio. We first tested four existing models, the Brinkman and Davies models and their Li and Logan variants (Sect. 2.1), but only present the Davies model and its Li and Logan modification because the other models yielded similar results. Figure 9a shows fractal dimension and drag ratio for each floc cam observation against the field of all possible model predictions defined by the zone between $\Omega_{\min}$ (Eq. 12) and 1 for the Davies model and its Li and Logan variant. The zone is the same for the two models because $\Omega_{\min}$ only depends on fractal dimension (Eq. 3; Eq. 12). As a result, the Li and Logan strategy, replacing D_p with a larger cluster diameter, D_c, does not affect the range of Ω predictions. Both models are largely incompatible with the data because ~88% of the data (excluding $\Omega > 1$ data) lie below the zone of possible Ω.

The discordance between our measured values of Ω and the Davies model is probably because natural flocs violate the model assumptions of uniform porosity and a single primary particle size. However, a complete 3-D rendering of floc structure is generally not known or practical, making a full model of non-uniform flow paths difficult to implement. Instead, we explored an empirical approach to modify the Davies model (Eq. 6) by replacing φ with a permeable solid fraction, φ_r, but keeping the same D_p/D_f. That is,

$$\xi^{-2} = \left(\frac{D_p}{D_f}\right)^2 [16\varphi_r^{1.5}(1 + 56\varphi_r^3)]^{-1}, \qquad (13)$$

where the permeable solid fraction, $\varphi_r = (D_f/D_p)^{n_r-3}$, and n_r is the permeable fractal dimension (analogous to Eq. 2). This permeable solid fraction model gives another degree of freedom, φ_r or n_r, to capture potential impacts of non-uniform porosity and primary particle size distribution on permeability. Unfortunately, we could not predict φ_r independent of Ω. Instead, we inverted our Ω estimates for values of φ_r and n_r that yield a perfect match between theory for Ω (Eq. 3 and 13) and observations (Fig. 9a). Figure 9b shows the values of φ_r that cause agreement between theory and data. In most cases, φ_r is smaller than φ (median φ_r/φ = 0.12; IQR/2 = 0.10). We interpreted this result to indicate that φ_r represents the subset of primary particles that set the main through-flow conduits because not all primary particles contribute to through-flow and drag (see Sect. 6.3 for more discussion). n_r estimates range between 1.06 and 2.80 with a median of 1.57. The fact that all n_r values fall within the physically meaningful range of 1 to 3 supports using the permeable solid fraction model (Eq. 13) to overcome the assumptions in the Davies model.

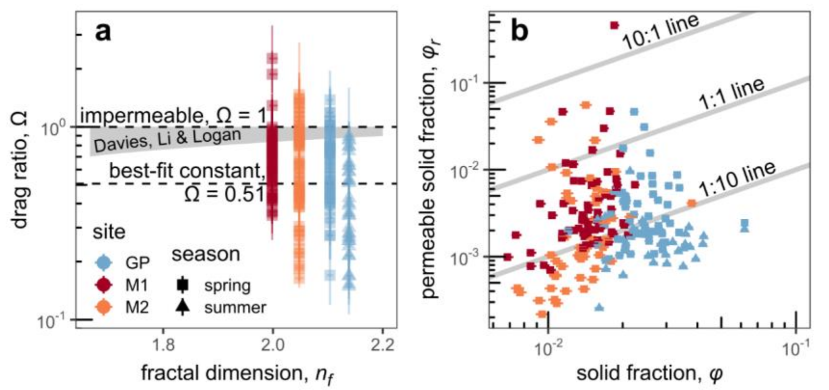

Figure 9: Drag ratio~~, Ω,~~ results from combining the explicit model and floc cam-measured floc settling velocity ~~measured from floc cam images~~. (a) Fractal dimension and measured drag ratio. The shaded area indicates the field of all possible ~~Ω~~drag ratios under the ~~Brinkman~~Davies model (Eq. ~~4~~6) and ~~the~~its Li and Logan modification. ~~(b) Solid fraction and drag ratio. The black curves are contours of the permeable cluster model at different values of cluster-floc diameter ratio, D_c/D_f. Vertical bars~~ Drag ratio bars indicate the propagated ~~95% confidence interval of floc cam-measured settling velocity.~~

~~Turning to the remaining floc properties, the bulk~~**mean standard error on the background displacement estimate (Sect. 4.4) and propagated 95% bootstrap uncertainty on n_f and D_p. (b) Solid fraction and permeable solid fraction according to the permeable solid fraction** ~~and settling velocity ranged from ~0.05 to 0.15 (excepting higher fractions at site M1; Fig. 10a) and ~0.1 to 1 mm s^{-1} (Fig. 10b), respectively, and once again varied little in the vertical (Fig. 10ab). The bulk solid fractions are in line~~**model based on the Davies model. Horizontal bars represent the propagated 95% bootstrap uncertainty on n_f and D_p. The legend in panel a applies for all panels.**

Formatted: Font: 9 pt, Bold

5.8 Floc Settling Velocity

To ~~with prior floc density measurements (e.g., Van Leussen, 1988). We applied the fitted n_f, D_p, and $\Omega = 0.51$ in the explicit model to~~ calculate floc settling velocity distributions ~~from~~, we used the measured n_f, D_p, and Ω in the explicit model to convert the floc size distributions (Sect. 4.~~5.2~~6.4). We used a best-fit constant ~~Ω for simplicity~~$\Omega = 0.51$ because we ~~could not predict cluster diameter. The median~~ only had Ω estimates associated with only four concentration-depth profiles that had floc cam measurements (Table 1; Fig. 9a). Median floc settling velocities at the channel sites in spring and summer were ~0.2~~-~~ to 0.5 mm s^{-1} (Fig. ~~10bc). The island~~10a). Island sites had median floc settling velocities of about 0.1 mm s^{-1}, with a substantial fraction of floc settling velocity of order 0.01 mm s^{-1}. ~~The smaller fractal dimension and finer floc size distribution~~No vertical trends in median settling velocity were apparent. Depth-averaged floc settling velocity broadly ranged from ~0.1 to 1 mm s^{-1} (Fig. 10b). Finer floc sizes (Fig. 7c), despite larger bulk solid fractions (Fig. 7e), in the island caused slower floc settling velocity in the island compared to that in the channels (Fig. ~~6; Fig. 7).~~10b).

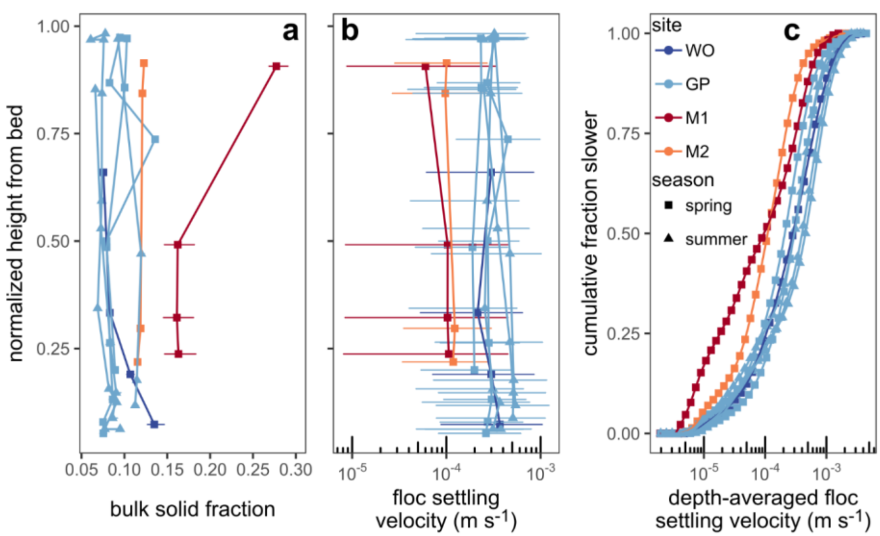

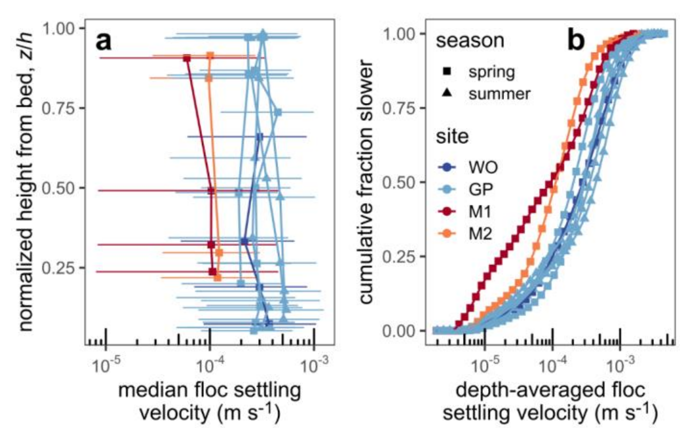

Figure 10: Floc ~~bulk solid fraction and~~ settling velocity results. (a) Profiles of ~~bulk solid fraction. Horizontal bars represent the 95% bootstrap uncertainty. (b) Profiles of floc settling velocity. Points represent the~~ median floc settling velocity. Horizontal bars represent the span of the 0.16 and 0.84 quantile floc settling velocities. (~~c~~b) Cumulative distribution functions of depth-averaged floc settling velocity. The legend in panel c applies for all panels.

~~Flocculation ultimately caused an order 10- to 100-fold increase in in situ diameter and settling velocity compared to those of primary particles according to the distribution quantiles (Fig. 11). The floc diameter quantile is systematically larger than the corresponding primary particle quantile for all profiles by a typical factor of 10 (Fig. 11a). The median floc diameter is at least 4 times greater than the median primary particle diameter for all profiles and at least 10 times for five profiles. The floc settling velocity quantile relative to the primary particle settling velocity quantile is distributed across a wide range of factors from ~1, for the coarsest fractions of the primary particle distribution, to >100, for the finest fractions of the primary particle distribution (Fig. 11b). This pattern shows that flocculation more strongly enhanced the settling velocity of fine grains than that of coarser (but still flocculated) grains because the settling velocities of the coarsest flocculated grains approach the floc settling velocity (Lamb et al.,~~ 5.9 ~~2020; Nghiem et al., 2022). On average, the floc settling velocity quantiles are one order of magnitude faster than the corresponding primary particle settling velocity quantiles.~~

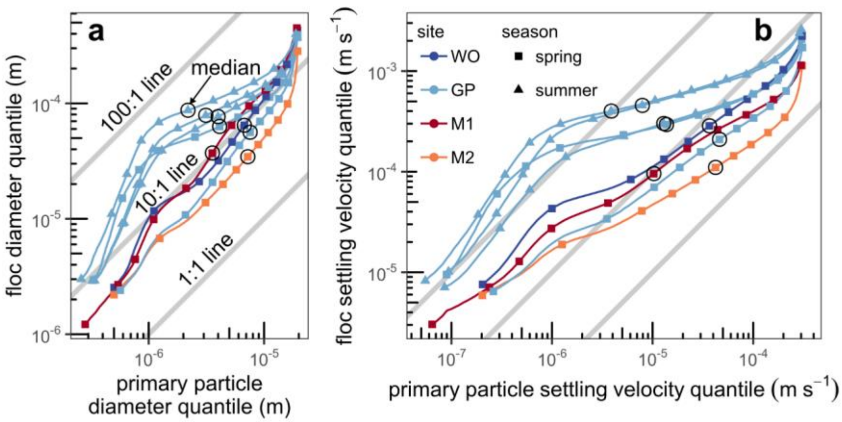

Figure 11: Floc and primary particle quantile-quantile plots for the depth-averaged profiles. (a) Floc and primary particle diameters. 100:1, 10:1, and 1:1 lines are displayed for reference. The median for each profile is circled. (b) Floc and primary particle settling velocities. The annotations in panel a also apply to panel b. The legend in panel b also applies to panel a.

Finally, we summarize the relationships between the bulk floc properties (diameter, solid fraction, and settling velocity) measured in WLD. Floc diameter decreased with primary particle diameter for channel sites (Fig. 12a). No trend is apparent for the island sites. There is little correlation between bulk solid fraction and primary particle diameter (Fig. 12b). The relationship between floc settling velocity and primary particle diameter (Fig. 12c) resembles the relationship between floc and primary particle diameters (Fig. 12a). Floc diameter and bulk solid fraction scale inversely as expected from fractal theory (Fig. 12d; Eq. 4), indicating a fractal dimension of 2.4 which is close to the fitted global value of 2.1 (Sect. 5.6). Floc settling velocity also scales inversely with bulk solid fraction (Fig. 12e) as predicted by the explicit model. The floc diameter and settling velocity scale well with each other as expected (Fig. 12f) because we calculated floc settling velocity following the explicit model. In the channels, median floc diameter in the summer tended to be slightly larger (~80 versus ~60 μm) than that in the spring (Fig. 12d). However, the seasonal difference in floc settling velocity is negligible (Fig. 12f) because solid fraction decreases with floc diameter and partly compensates for the diameter difference.

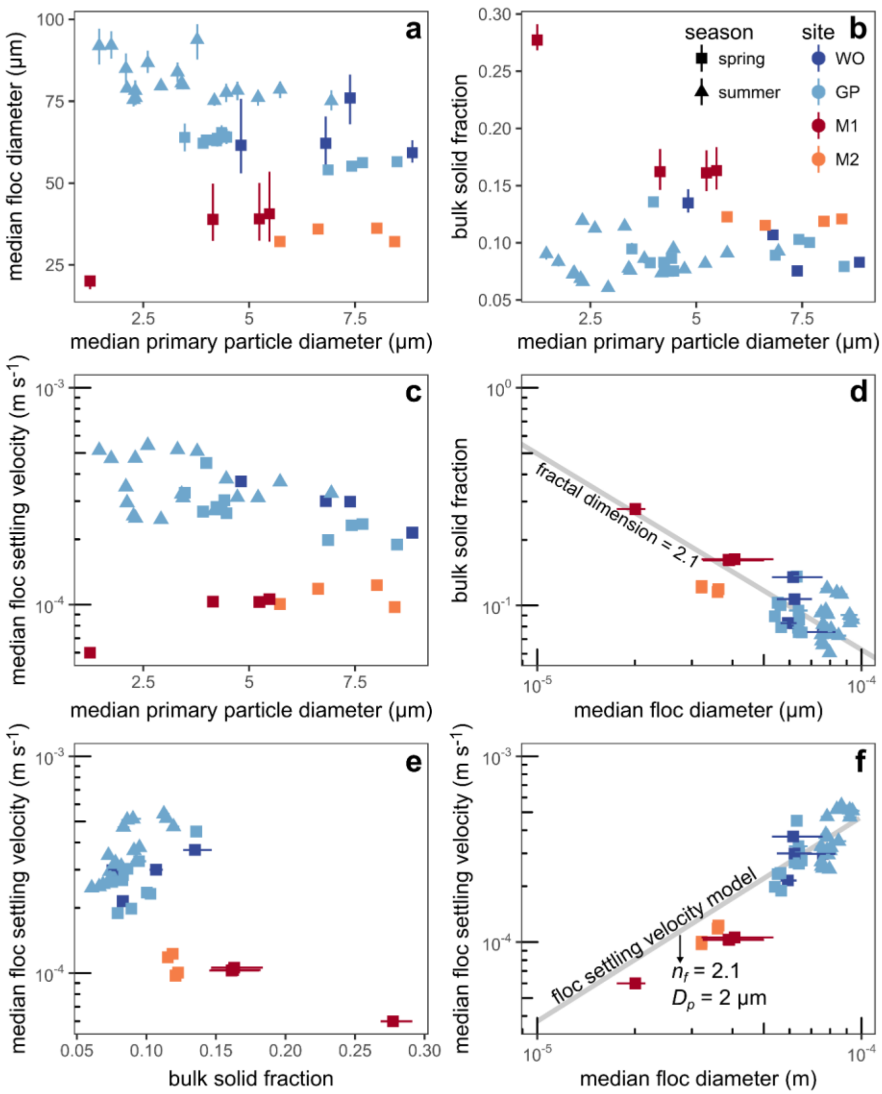
a
median floc diameter (µm)
median primary particle diameter (µm)
b
season
spring
summer
site
WO
GP
M1
M2
bulk solid fraction
median primary particle diameter (µm)
c
median floc settling velocity (m s-1)
median primary particle diameter (µm)
d
fractal dimension = 2.1
bulk solid fraction
median floc diameter (µm)
e
median floc settling velocity (m s-1)
bulk solid fraction
f
floc settling velocity model
nf = 2.1
Dp = 2 µm
median floc settling velocity (m s-1)
median floc diameter (m)

~~**Figure 12: Bulk floc property results. (a) Median primary particle and floc diameters. (b) Median primary particle diameter and bulk solid fraction. (c) Median primary particle diameter and floc settling velocity. (d) Median floc diameter and bulk solid fraction. The line indicates a fractal dimension of 2.4. (e) Bulk solid fraction and median floc settling velocity. (f) Median floc diameter and settling velocity. The line indicates a floc settling velocity model using typical values of the constrained parameters: fractal dimension of 2, an effective primary particle diameter of 2 μm, $b_1 = 10.14$, and $\Omega = 0.51$. The legend in panel b applies for all panels. Horizontal and vertical bars indicate the 95% bootstrap uncertainty.**~~

~~5.8~~ Validating ~~explicit model parameters~~the Explicit Model

We compared ~~the~~ Rouse-estimated floc settling velocities ~~of the Rouse-Vanoni equation inversion method~~(Sect. 4.5) and explicit model predictions as ~~a holistic~~an integrated test of the ~~plausibility of the~~ estimated n_f, D_p~~,~~ (Sect. 5.6), and Ω (Sect. 5.7) because these settling velocity estimates are independent. ~~Since the~~ Figure 11 shows that Rouse-~~estimated~~ estimate floc settling velocity ~~depends on the choice of~~ displays a strong linear trend with the median from the explicit model excepting the data point at site WO. Although we assumed a floc diffusivity ratio, β_{fl}, ~~(Sect. 4.4), we used three~~ of unity to calculate the Rouse-estimated floc settling velocities (Sect. 4.5), the data indicate that $\beta_{fl} = 0.32$ optimizes the correlation between the settling velocities well within error. $\beta_{fl} = 0.32$ is realistic because it matches previously estimated diffusivity ~~ratio models to test sensitivity assuming that they apply to flocs: constant (β_{fl} = 1), the quadratic equation of Van Rijn (1984),~~ratios (Nghiem et al., 2022) and ~~the empirical best-fit one-parameter equation of~~ranges predicted by diffusivity ratio models (e.g., De Leeuw et al.~~, (~~., 2020). ~~The Van Rijn~~As a result, we concluded that the Rouse-estimated settling velocity validates well our parametrization of the explicit model.

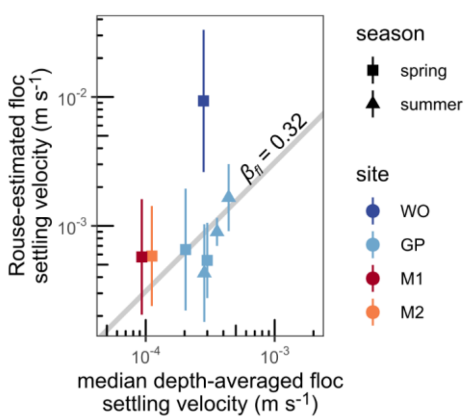

Figure 11: Rouse-estimated floc settling velocity, using $\beta_{fl} = 1$, and De Leeuw models are functions of the ratio of settling and shear velocities. The constant and Van Rijn diffusivity ratio models cause the Rouse-estimated floc settling velocity to be systematically larger than median depth-averaged floc settling velocity from the floc settling velocity distributions ranging from equal to a factor of ~30 faster (Fig. 13). The De Leeuw model yields Rouse-estimated floc settling velocities slower and faster than the median, but the average across all data points indicates approximately equal settling velocities (Fig. 13). The large scatter reflects uncertainty in predicting the diffusivity ratio and that the range of diffusivity ratio is unrestricted in the De Leeuw equation (De Leeuw et al., 2020). In contrast, the diffusivity ratio must be greater than or equal to 1 in the Van Rijn equation and is prescribed to be 1 in the constant case. Although the constant and Van Rijn models suggest that the floc settling velocity of the explicit model might be biased low, we judged that the estimated computed using estimates of n_f, D_p, and Ω in the explicit model are reliable because of. $\beta_{fl} = 0.32$ indicates the favorable comparison to the De Leeuw model, which is based on a large global river data compilation.

Formatted: Font: 9 pt, Bold

Formatted: Font: 9 pt, Bold

Formatted: Font: 9 pt, Bold

Formatted: Font: 9 pt, Bold

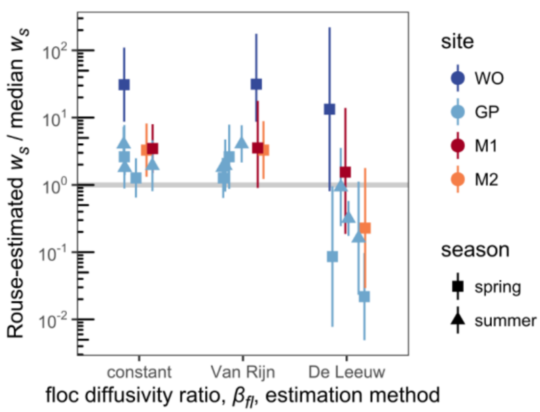

1040 Figure 13: Ratio of Rouse-estimated and median floc settling velocities bybest-fit floc diffusivity ratio estimation method. The median floc settling velocity is the median of the depth-averaged floc settling velocity distribution (Fig. 10).. Vertical bars indicate the 95% confidence interval on shear velocity (Sect. 4.1) and standard deviation of Rouse-estimated floc settling velocity with $\beta_{fl} = 1$.(Sect. 4.5).

5.9 10 Validating the Semi-empirical model controls on floc propertiesEmpirical Model

1045 The previous sections focused on constraining floc parameters and testing theory for the explicit model. We use the direct floc measurements to validate Figure 12 shows the validation of the semi-empirical model, in which all parameters are known through geochemical measurements (Sect. 4.6) and calculations in the prior sections, and use the model to examine

~~environmental controls on flocs in WLD.~~. We compared the semi-empirical model predictions (Eq. ~~6~~7; Nghiem et al., 2022) and the observed floc cutoff diameter (sediment concentration-depth profiles, Rouse-Vanoni theory; Sect. 4.5), floc settling velocity (floc cam, LISST combined with sample data; Sect. 4.6.4), and floc diameter (LISST combined with sample data; Sect. 4.6.1). We used the median of the depth-averaged distribution for floc settling velocity and floc diameter in the comparison because the semi-empirical model was calibrated on depth-averaged data (Nghiem et al., 2022). The semi-empirical model predicts the floc cutoff diameter well within a factor of ~2 of measurements and capture the overall data trend (Fig. 12a). ~~14a). As a note, the~~The measured floc cutoff diameter is not simply equal to 20 μm because the extra profiles without LISST and floc cam data have varying floc cutoff diameters from 20 to 50 μm. ~~The~~ Floc settling velocity predictions of the semi-empirical model ~~floc settling velocity~~ agree well in a factor of 2 with the floc cam median and ~~the fully calibrated~~LISST-based floc settling velocity measurements (Fig. 12b). ~~of the~~ Since we used the explicit model ~~(indicated as the LISST data points) agree well (Fig. 14b). The~~to calculate floc settling ~~velocities from~~velocity distribution (Sect. 4.6.4), Fig. 12b also confirms the ~~floc cam have inherent variability at the individual floc scale, but the median shows good agreement with the~~ consistency between the semi-empirical ~~model within a factor of 2 (Sect. 5.7).~~and explicit models. The floc diameter results indicate that the semi-empirical model predicts adequately within a factor of ~2, albeit with a limited number of data points (Fig. ~~14c~~12c). The ~~fact that the floc cutoff diameter model performs the best is expected because it required the fewest assumptions to derive (Nghiem et al., 2022). Overall, the~~ reasonable performance of the semi-empirical model against direct measurements in WLD validates the model ~~for predicting floc properties in freshwater. Additionally, the good agreement between the semi-empirical and explicit floc settling velocity models confirms that they are consistent with each other (Fig. 14b).~~.

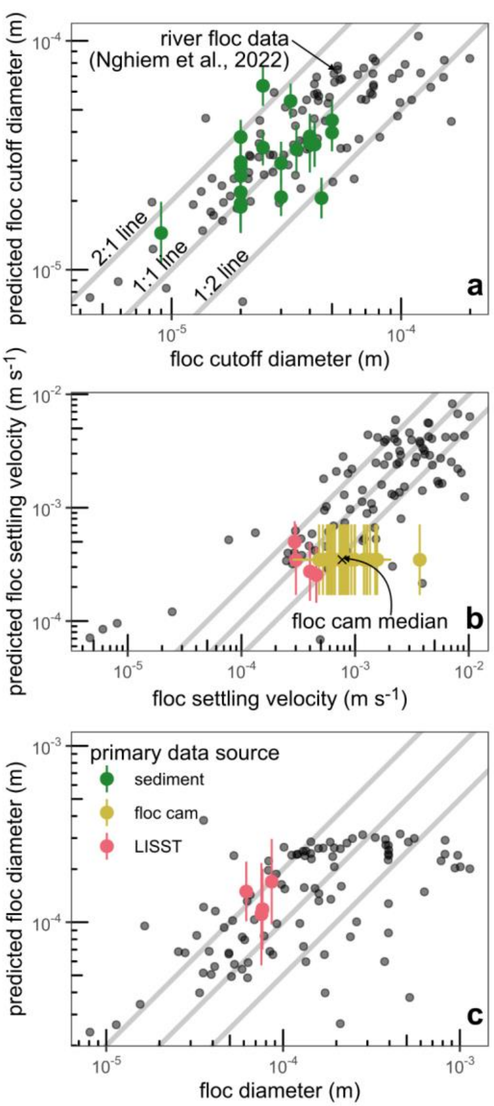

river floc data
(Nghiem et al., 2022)
2:1 line
1:1 line
1:2 line
a
predicted floc cutoff diameter (m)
floc cutoff diameter (m)
b
floc cam median
predicted floc settling velocity (m s-1)
floc settling velocity (m s-1)
primary data source
sediment
floc cam
LISST
c
predicted floc diameter (m)
floc diameter (m)

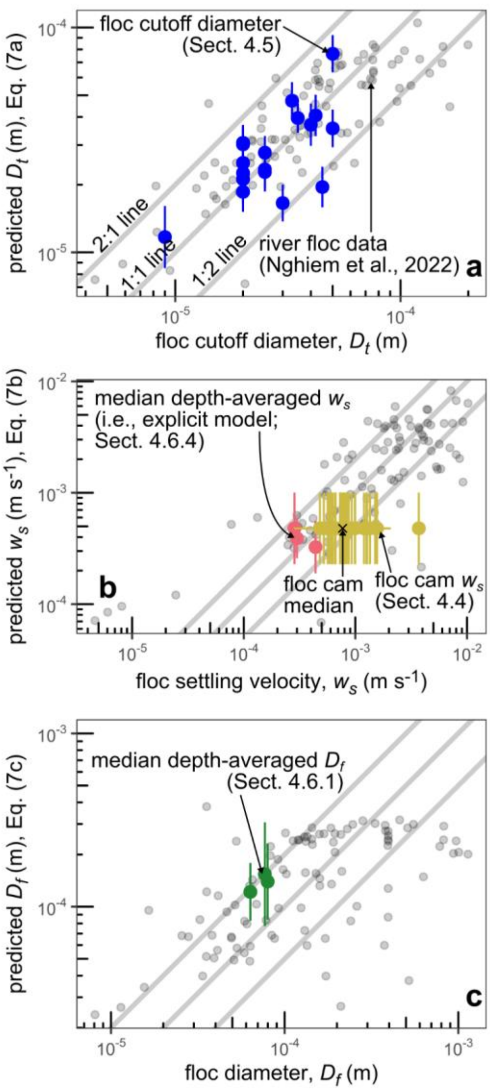

floc cutoff diameter
(Sect. 4.5)
river floc data
(Nghiem et al., 2022)
2:1 line
1:1 line
1:2 line
a
predicted D_t (m), Eq. (7a)
floc cutoff diameter, D_t (m)
median depth-averaged w_s
(i.e., explicit model;
Sect. 4.6.4)
floc cam
median
floc cam w_s
(Sect. 4.4)
b
predicted w_s (m s^{-1}), Eq. (7b)
floc settling velocity, w_s (m s^{-1})
median depth-averaged D_f
(Sect. 4.6.1)
c
predicted D_f (m), Eq. (7c)
floc diameter, D_f (m)

Figure ~~14~~12: Measured ~~floc properties~~ and semi-empirical model predictions of (a) floc cutoff diameter~~,~~, (Eq. 7a), (b) floc settling velocity~~,~~, (Eq. 7b), and (c) floc diameter ~~colored by primary data source (Table 1). Black~~(Eq. 7c). Gray points are the data ~~from~~that Nghiem et al. (2022) ~~that were~~ used to calibrate the semi-empirical model. Vertical bars represent the 95% confidence interval of predictions. ~~The labels and legend in panels a and c, respectively, apply to all panels. Sediment data include data from profiles without paired LISST and floc cam data.~~ The floc cam data have the same predicted floc settling velocity because they represent a single floc cam deployment. Data for which water chemistry was not measured are omitted because they lack semi-empirical model predictions, which explains the absence of floc cam data in panel c.

~~The agreement between the semi-empirical model and floc properties shows that turbulence, sediment concentration and mineralogy, organic matter, and water chemistry control~~To demonstrate environmental effects on flocculation ~~in WLD (Eq. 6;~~, we followed Nghiem et al.~~,~~. (2022~~). We~~) and plotted the predictors in the semi-empirical model against the floc cutoff diameter~~,~~ (normalized to remove the effects of other variables and by the median~~,~~) because the floc cutoff diameter model (Eq. ~~6a~~7a) displays the best correlation with measurements (Fig. ~~14~~12). We expect similar patterns for floc settling velocity and diameter because the floc variables correlate with each other~~.~~ (Nghiem et al., 2022). Turbulence, through the Kolmogorov microscale, limits floc size and settling velocity (Fig. ~~15a~~13a) because the semi-empirical model assumes that floc growth and breakage rates are balanced (Fig. ~~6d~~7d). As depth-averaged median primary particle diameter increases, coarser and faster settling grains can be added to flocs (Fig. ~~15b~~13b). Higher sediment concentration enhances flocculation by increasing particle collision rate (Fig. ~~15c~~13c). The effect of organic matter, as quantified by the organic cover fraction, θ, promotes flocculation at low values, but is predicted to have an opposite effect once $\theta > 0.5$ because high organic coverage stabilizes sediment surfaces from aggregation (Fig. ~~15d~~13d). Sediment Al/Si and relative charge density, Φ, vary inversely with floc properties because they might preferentially cause clay flocculation and exclude faster settling silt grains from flocs (Fig. ~~15ef). We detected little systematic variation in floc cutoff diameter with season and location in channel or island.~~13ef). These trends for WLD are similar to those found for global rivers (Nghiem et al., 2022).

Formatted: Indent: First line: 0.5"

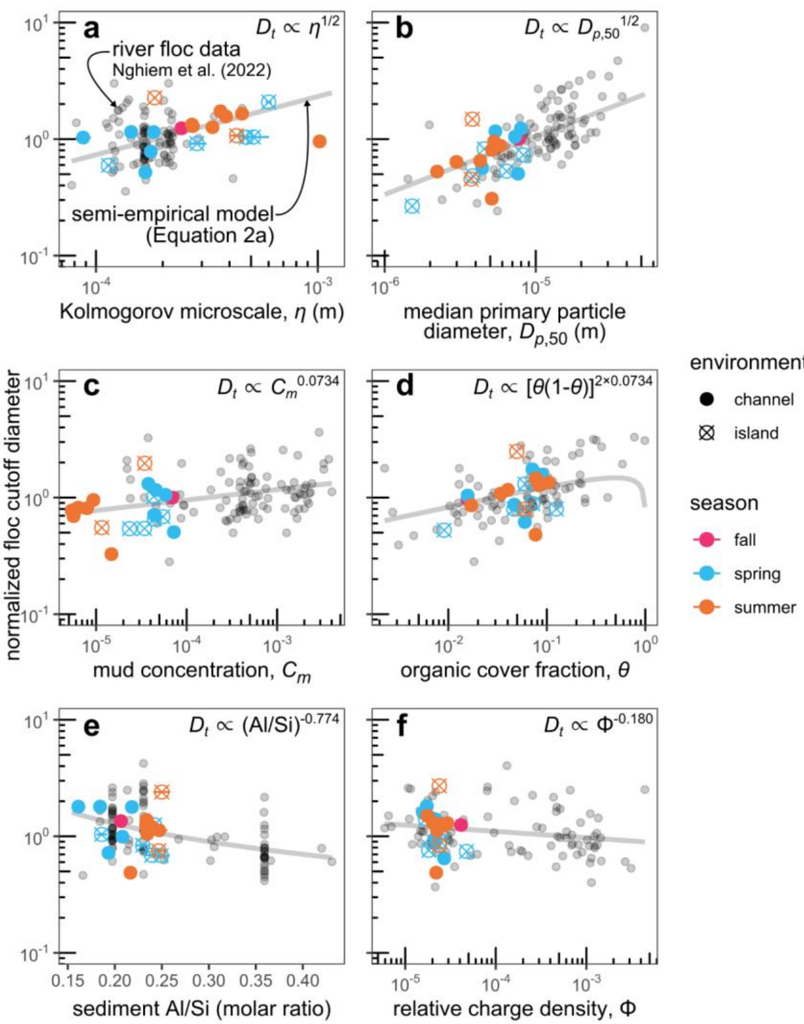

a
$D_t \propto \eta^{1/2}$
river floc data
Nghiem et al. (2022)
semi-empirical model
(Equation 2a)
Kolmogorov microscale, η (m)
b
$D_t \propto D_{p,50}{}^{1/2}$
median primary particle diameter, $D_{p,50}$ (m)
normalized floc cutoff diameter
c
$D_t \propto C_m{}^{0.0734}$
mud concentration, C_m
d
$D_t \propto [\theta(1-\theta)]^{2\times0.0734}$
organic cover fraction, θ
e
$D_t \propto (\mathrm{Al/Si})^{-0.774}$
sediment Al/Si (molar ratio)
f
$D_t \propto \Phi^{-0.180}$
relative charge density, Φ
environment
channel
island
season
fall
spring
summer

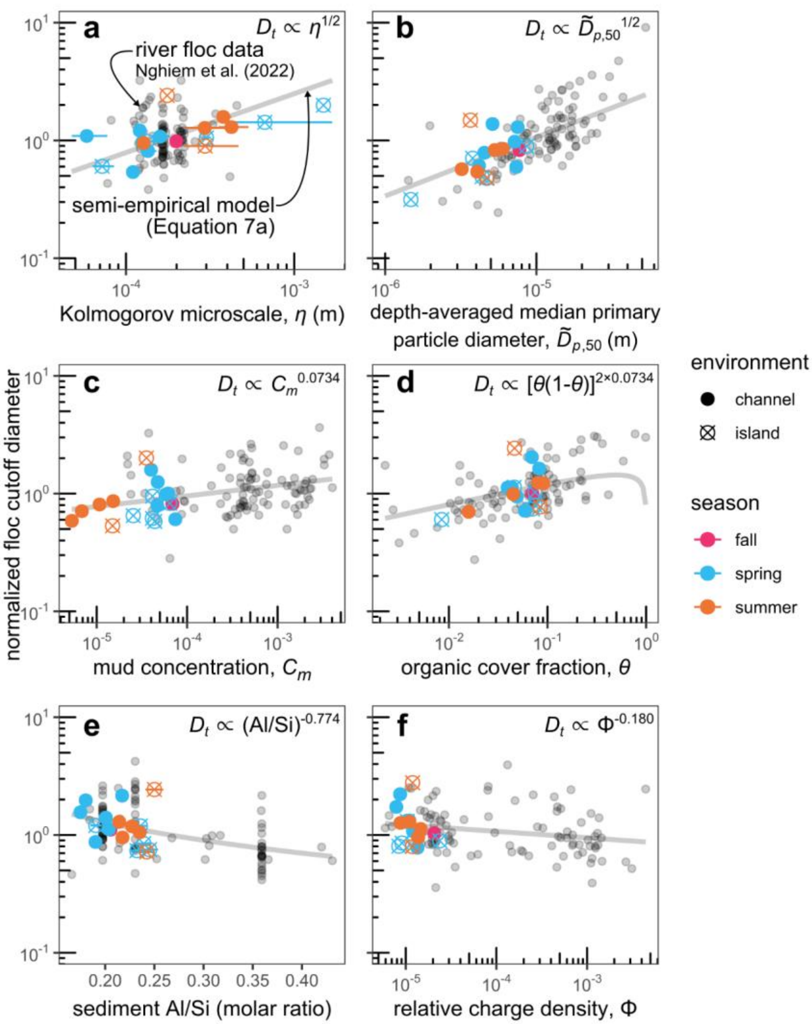

Figure ~~15~~13: Semi-empirical model predictors plotted against floc cutoff diameter, D_t, normalized by the effects of all other predictors in the floc model (Eq. ~~6a~~7a). Gray curves indicate the model prediction. Horizontal ~~error~~ bars indicate the (a) 95%

confidence interval on shear velocity, (d) 1-σ error on percent weight organic carbon, or (e) 95% confidence interval on Al/Si estimates. The labels in panel a apply to all panels.

6 Discussion

~~Trends~~ 6.1 Leveraging Multiple Floc Data Sources

By combining three floc data sources (in ~~Kolmogorov microscale, primary particle diameter, and mud~~ situ laser diffraction, camera, sediment concentration ~~indicate~~ -depth profiles), we overcame the ~~potential importance~~limitations of ~~turbulence in reducing~~ the ~~variability~~individual data sources and derived a nearly complete accounting of floc properties, including floc diameter, solid fraction, floc settling velocity, fractal dimension, effective primary particle diameter, and drag ratio. In situ laser diffraction data alone are limited because they record a mixture of flocs and unflocculated sediment grains (e.g., Livsey et al., 2022). We developed a technique to isolate floc concentration and size distribution by separating flocs and unflocculated grains (Fig. 4) using in situ laser diffraction data and sediment concentration-depth profiles (Sect. 4.6.1). From this technique, we also computed primary particle concentration and size distribution and floc bulk solid fraction (i.e., ratio of primary particle and floc concentrations).

In past studies, a key knowledge gap was the role of effective primary particle diameter and drag ratio on floc settling velocity in the explicit model (e.g., Strom and Keyvani, 2011) because camera-measured floc diameter and settling velocity data were insufficient to separate those variables. We leveraged floc size distribution and bulk solid fraction to compute fractal dimension and effective primary particle diameter (Sect. 4.6.2). With an independent estimate of effective primary particle diameter, we could then use floc cam-measured floc diameter and settling velocity and fractal dimension to estimate drag ratio (Sect. 4.6.3). Our ability to disentangle effective primary particle diameter and drag ratio thus paved the way to test theory.

Although our data synthesis proved successful at furnishing many floc properties and holds good potential for future field studies, it still has limitations. We could only estimate a single effective primary particle diameter for each floc size distribution, but the effective primary particle diameter might vary within the floc size distribution especially at the fine tail where floc and effective primary particle diameters might be on a similar scale. There is some uncertainty combining LISST and suspended sediment sample data. We assumed that they measured statistically equivalent material because they did not strictly measure the exact same material. We assumed that all sediment finer than the floc cutoff diameter was flocculated across the water column (Sect. 4.5), but some fraction of this sediment could actually be unflocculated. We could not determine this fraction with our data.

6.2 Predicting Floc Settling Velocity

The explicit and semi-empirical floc settling velocity models are consistent with each other (Fig. 12b), indicating that model choice depends on the scale of interest and data availability. The explicit model is at the scale of the individual floc whereas the semi-empirical model is depth-averaged. We were able to compare the models because the depth-averaged floc settling velocity distributions represent a depth-averaging of the explicit model, which was used to calculate floc settling velocity distributions (Sect. 4.6.4). The semi-empirical model has the advantage of relying on geochemical data that can be easier to measure compared to the floc-specific parameters in the explicit model.

Although we used joint camera, in situ particle sizing, and suspended sediment concentration and grain size distribution profiles to constrain effective primary particle diameter and drag ratio in the explicit model, we suggest that the explicit model can still be used to predict floc settling velocity given only suspended sediment grain size distribution and floc diameter (e.g., through camera or in situ particle sizing data). The primary particle size distribution can be obtained from the suspended sediment grain size distribution by choosing a floc cutoff diameter (in the range of ~20 to 50 µm; Nghiem et al., 2022) and removing coarser sediment from the distribution (Sect. 4.6.1). The fractal dimension of natural flocs can be assumed to be 2 (Winterwerp, 1998). The fractal dimension and primary particle size distribution feed into Eq. (5) to predict effective primary particle diameter. Predicting drag ratio remains a challenge because prior analytical permeability models were inconsistent with our drag ratio estimates (Fig. 9a). For simplicity, Ω can be assumed to be an appropriate constant based on additional field measurements or left as a tuning parameter.

The semi-empirical model predicts floc cutoff diameter, diameter, and settling velocity as a semi-empirical function of water chemistry, organic matter, sediment mineralogy and concentration, and turbulence in the absence of a purely mechanistic theory to link these factors. The full unsteady form of the semi-empirical model, along with existing dynamic flocculation models (e.g., Xu et al., 2008; Son and Hsu, 2011; Shen et al., 2018), can be used to predict floc settling velocity through time and space in a sediment transport model. However, this approach can be computationally expensive and require parameters that are difficult to constrain. Our analysis suggests the assumption of local equilibrium is a reasonable simplification to predict floc properties because our observations are consistent with the equilibrium semi-empirical model (Fig. 12). This fact implies that flocs quickly adjust to their local conditions, a behavior that has some experimental evidence (Tran et al., 2018). In fact, we suggest that using a single constant floc settling velocity for the mud settling velocity (Roberts et al., 2000; Braat et al., 2017) might be reasonable in alluvial channels because tradeoffs between turbulence, sediment concentration, and primary particle size and mineralogy might offset each other (Sect. 6.4).

6.3 Role of Effective Primary Particle Diameter and Drag Ratio on Floc Settling Velocity

Our results indicate that the effective primary particle diameter should follow a fractal theory that conserves the volume and fractal space of the original primary particles (Bushell and Amal, 1998; Eq. 5; Fig. 8b) in contrast to past work that treated D_p as an average length scale of primary particles (Syvitski et al., 1995; Strom and Keyvani, 2011). If one assumed D_p is the median, then one would overestimate the solid fraction and floc settling velocity by a factor dependent on the fractal dimension (Eq. 1 and 2). In our data, this factor ranges from 1 (no effect) to 5 and has a median of 2.2. We expect the fractal model to hold in saline environments too because it is based on geometric principles.

We used a new permeable solid fraction model to determine the physical reason our drag ratio estimates are incompatible with existing permeability models. Natural flocs are distinct because they have non-uniform porosity (Eq. 2) and a primary particle size distribution. These features probably caused the much smaller drag ratios (higher permeability) than could be predicted by prior permeability models (Fig. 9a). The Li and Logan strategy attempts to account for non-uniform porosity by replacing the effective primary particle diameter with a larger cluster diameter representing the clusters that form the main flow paths through the floc. However, this approach is very limited because, as recognized by Kim and Stolzenbach (2002), the increase in permeability caused by the Li and Logan modification is small because an effective increase in the solid fraction partially offsets larger pores caused by primary particle clustering. Kim and Stolzenbach (2002) found that the original Davies model (Eq. 6) performed well at predicting the hydrodynamic drag on fractal aggregates with non-uniform porosity, suggesting that the Davies model is suitable for flocs in contrast to our findings (Fig. 9a). If non-uniform porosity caused by fractal structure is not the source of the discrepancy between our drag ratio estimates and the Davies model, then it is likely the primary particle size distribution because Kim and Stolzenbach (2002) did not test aggregates containing many primary particle sizes. The permeable solid fraction model offers a physical explanation because the permeable solid fraction is, on average, 12% of the true solid fraction (Fig. 9b). This result suggests that a subset of the primary particles composes the portion of the floc structure (characterized by the permeable fractal dimension) responsible for conducting flow through the floc. The rest of the primary particles might be shielded from the flow because of their configuration with respect to adjacent larger particles and do not contribute to permeability. The configuration of organic matter within flocs might also affect permeability by controlling flow paths. It is difficult to study all these effects because the complete floc structure must be known, but recent advances in 3-D floc imaging might facilitate more detailed studies (Lawrence et al., 2022; Lawrence et al., 2023).

Although the drag ratio estimates depend on the assumed floc shape, floc shape is not responsible for the inability of existing permeability models to reproduce the drag ratio. Floc shape affects the shape factor, b_1, in the explicit model. Larger values of b_1 cause smaller drag ratio estimates (Sect. 4.6.3). Stokes law shows that $b_1 = 18$ (Stokes, 1851) for an impermeable sphere ($\Omega = 1$). Strom and Keyvani (2011) suggested that $b_1 \sim 20$ is suitable for flocs with $n_f < 2$, but $b_1 = 120$ for flocs with $n_f \geq 2.5$. Regardless of the precise value of b_1, particle shape effects only cause $b_1 > 18$ because shape irregularities induce more drag ~~characteristics in delta channels. The~~(McNown and Malaika, 1950; Dietrich, 1982). We used a relatively low value of $b_1 = 20$ (Ferguson and Church, 2004) to calculate the drag ratio. Higher b_1 would only further amplify floc permeability and widen the discrepancy with theory.

6.4 Environmental Controls on Flocculation

The semi-empirical model trends in Fig. 13 show the major environmental controls on flocs in WLD and globally. However, these variables are not independent. We hypothesize that turbulence causes correlation and feedbacks between these factors through sediment entrainment and settling dynamics in alluvial systems. To test this hypothesis, Figure 14 compares Kolmogorov microscale, which scales inversely with turbulence intensity, and semi-empirical model parameters. For rivers and WLD channels, Kolmogorov microscale correlates with finer ~~median~~ primary particle diameter and higher Al/Si because more turbulent flows (smaller microscale and higher shear velocity) entrain and suspend coarser sediment (Fig. ~~16ab).~~14ab). Coarser primary particles have distinct mineralogy (lower Al/Si) than finer grains. Higher mud concentration ~~in channels~~ corresponds to smaller Kolmogorov microscale because higher fluid stress entrains more sediment from the bed (Fig. ~~16c). These feedbacks show that finer primary particles, larger Al/Si, and smaller mud concentration (corresponding to smaller floc cutoff diameter) offset the effect of larger~~ 14c). Flows with higher turbulent energy can also maintain faster-settling flocs, if conditions permit their formation, in the water column (Eq. 8; Dunne et al., 2024). All else equal, these interactions indicate that higher turbulence intensity correlates with larger floc cutoff diameter, faster floc settling velocity, and larger floc diameter (Eq. 7) in alluvial channels. However, increases in turbulence intensity offset these effects because they cause floc breakage at equilibrium, leading to a negative feedback. These patterns are not evident in the WLD island because variables are poorly correlated with Kolmogorov microscale ~~on increasing floc cutoff diameter~~(Fig. 14) potentially owing to more complicated two-dimensional and unsteady effects on sediment transport (Geleynse et al., 2015; Bevington et al., 2017). ~~ultimately limit variability~~ We argue that turbulence is the overriding variable controlling flocculation in ~~floc cutoff diameter in delta~~ global rivers and the channels~~. The pattern does~~ of WLD because it not ~~hold~~only directly affects particle collisions, floc breakage (Winterwerp, 1998), and flow competence with respect to flocs, but also sets concentration and primary particle size and mineralogy. The negative feedback demonstrates that flocculation can buffer partially against spatiotemporal changes in turbulence, a mechanism that might explain observations of limited floc settling velocity variation (~0.2 to 0.6 mm s^{-1}) across seasons in the ~~island where the predictors are uncorrelated with~~ Mississippi River (Osborn et al., 2023) and, more broadly, the limited global variation of ~0.1 to 1 mm s^{-1} (e.g., Hill et al., 2000; Mikkelsen et al., 2007; Nghiem et al., 2022).

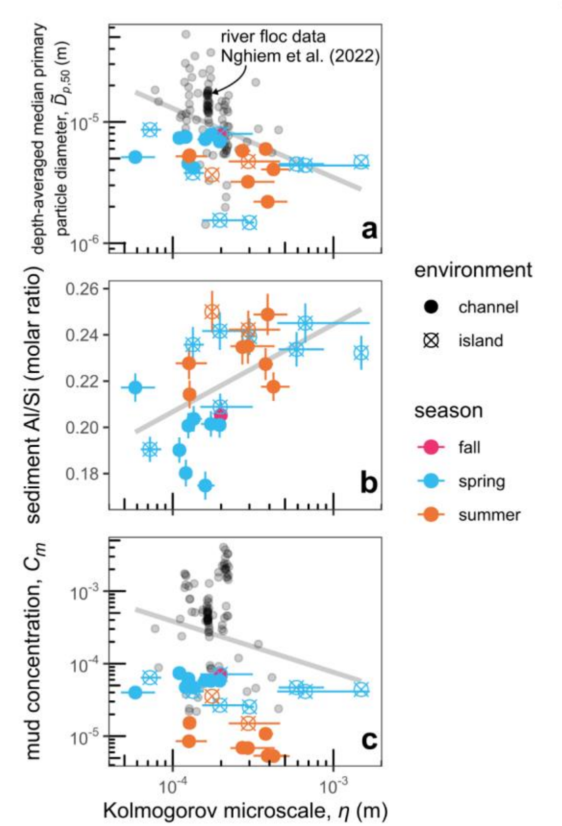

Figure 14: Kolmogorov microscale. The remaining variables, organic cover fraction and relative charge density, do not show clear trends by season and location (Fig. 15ef).

Formatted: Font: 9 pt, Bold

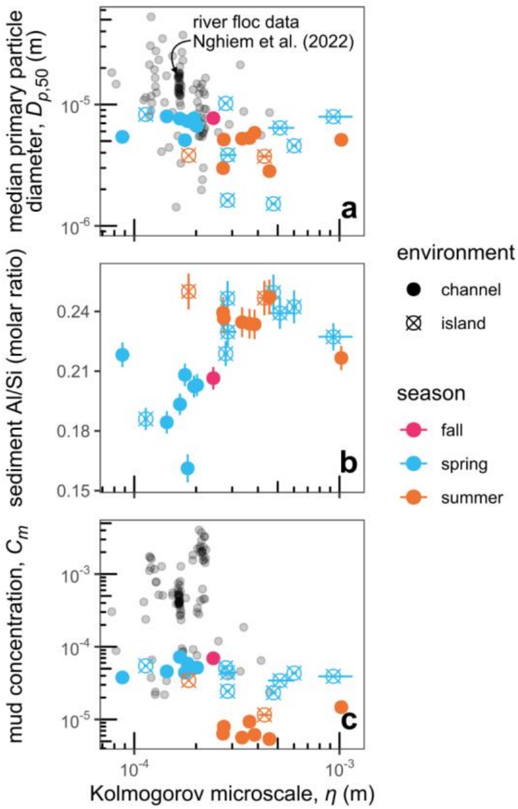

~~Figure 16: Kolmogorov microscale~~ and (a) <u>depth-averaged</u> median primary particle diameter, (b) sediment Al/Si, and (c) mud volume concentration. <u>In each panel, the gray line indicates the fitted power law for reference.</u> Horizontal error bars indicate the 95% confidence interval on shear velocity. In panel b, vertical error bars indicate the 95% confidence interval on Al/Si estimates.
1220 **River floc data are omitted in panel b because most Al/Si data were compiled from separate data sources in Nghiem et al. (2022).**

In contrast to the other semi-empirical model inputs, organic cover fraction and relative charge density vary less and are not responsible for the bulk of the variability in floc parameters (Fig. 136 Discussion

6.1 Predicting Floc Settling Velocity

The explicit and semi-empirical floc settling velocity models yield consistent predictions (Fig. 14b), suggesting that, in practice, the model choice depends on data availability. The explicit model has conventionally been used to predict the floc settling velocity given the floc diameter, but suffered from uncertainty in the effective primary particle diameter and drag ratio. Although we used joint camera, in situ particle sizing, and suspended sediment concentration and grain size distribution profiles to constrain effective primary particle diameter and drag ratio, we suggest that the explicit model can still be used to predict floc settling velocity given only suspended sediment grain size distribution and floc diameter (e.g., through camera or in situ particle sizing data). The primary particle size distribution can be obtained from the suspended sediment grain size distribution by choosing a floc cutoff diameter (in the range of ~20 to 50 µm; Nghiem et al., 2022) and removing coarser sediment from the distribution. The fractal dimension of natural flocs can be assumed to be 2 (Winterwerp, 1998). The fractal dimension and primary particle size distribution feed into the simplified fractal model (Eq. 11) to predict effective primary particle diameter. Predicting drag ratio remains a challenge because prior analytical permeability models perform poorly for WLD flocs (Fig. 9). Although a new permeable cluster model can capture the full range of drag ratios (Fig. 9b), it is difficult to use because a model for cluster diameter is missing. For simplicity, Ω can be assumed to be an appropriate constant based on field measurements or the values reported here.

The semi-empirical model has the advantage of relying on geochemical factors that can be easier to estimate, especially as functions of space and time, compared to the floc parameters in the explicit model. The consistency between the models indicates that the effects of D_p and Ω are implicitly captured in the semi-empirical model. The full unsteady form of the semi-empirical model, along with a host of other existing dynamic models (e.g., Xu et al., 2008; Son and Hsu, 2011; Shen et al., 2018), can be used to predict floc settling velocity through time and space in a sediment transport model. However, this approach can be computationally expensive and require parameters that are difficult to constrain. Our analysis suggests the assumption of local equilibrium is a reasonable simplification to predict floc properties because our observations are consistent with the equilibrium semi-empirical model (Fig. 14). This fact implies that flocs quickly adjust to their local conditions, a behavior that has some experimental evidence (Tran et al., 2018). We suggest that an even simpler treatment, using a single constant floc settling velocity for the mud settling velocity as is common in sediment transport models (Roberts et al., 2000; Braat et al., 2017), is reasonable in alluvial channels because tradeoffs between turbulence and primary particle size and mineralogy can compensate for each other and limit the variability in floc settling velocity (Sect. 5.9 and 6.3).

6.2 Role of effective primary particle diameter and drag ratio on floc settling velocity

Our results indicate that the effective primary particle diameter should be calculated using a fractal equation that conserves the volume and fractal space of the original primary particles (Bushell and Amal, 1998; Eq. 3 and 11; Fig. 8) in contrast to past work that treated D_p as a characteristic length scale of primary particles (Syvitski et al., 1995; Strom and Keyvani, 2011). The median primary particle diameter tends to overestimate the effective primary particle diameter, solid fraction, and floc settling velocity (Fig. 8d). The simplified fractal equation (Eq. 11) is suitable to predict D_p given the number-based primary particle size distribution because flocs contain sufficiently many primary particles for the central limit theorem to hold (Fig. A2b). We expect the fractal model to also hold in saline environments.

A new permeable cluster model explains our drag ratio estimates better than the Brinkman model likely because it empirically allows for clusters to be permeable. In the Brinkman model, flow through the floc is assumed to impart drag on the primary particles (Brinkman, 1947). By using a larger cluster diameter instead of primary particle diameter, the Li and Logan variant causes a relatively small increase in permeability because the increase in solid fraction partially offsets the effect of larger pores caused by reorganization of primary particles into clusters (Kim and Stolzenbach, 2002). The permeable cluster model is essentially a middle ground because, like the Li and Logan model, it uses a cluster diameter relative to the floc diameter as the key length scale in the permeability equation (e.g., Eq. 4). However, like the Brinkman model, it uses the original solid fraction and hence assumes primary particles are subject to the drag, a behavior that implies that the clusters themselves are permeable because primary particles are still able to experience the flow.

On the other hand, the classic Brinkman model underestimates floc settling velocity and floc permeability (i.e., overestimates drag ratio) in our data because one or both assumptions of uniform porosity and single primary particle size are violated. Although typical permeability equations have the same assumptions, a different permeability equation among the many available (see review in Kim and Stolzenbach, 2002) might be consistent with the drag ratio estimates. Indeed, Kim and Stolzenbach (2002) found that many models, including Brinkman, underestimated the permeability of fractal aggregates (albeit with a single primary particle diameter), but the Davies (1953) model performed well. However, we found that the Davies model likewise is not compatible with our drag ratio estimates using the same analysis as in Sect. 5.7. If fractal structure is not the source of the discrepancy, then the presence of multiple primary particle sizes might be responsible because it can control the pore size and structure distribution (e.g., Li and Logan, 2001; Kim and Stolzenbach, 2002). In addition, the configuration of organic matter within flocs might also affect permeability by controlling flow paths. Clearly, it is difficult to account for all these effects using a general theory because the complete floc structure and composition must be known. The cluster diameter in the permeable cluster model empirically encapsulates the combination of these effects, making it difficult to link the cluster diameter to a physical measurement.

Although the drag ratio estimates depend on the assumed floc shape, floc shape is not responsible for the inability of the Brinkman model and the Li and Logan method to reproduce the observed drag ratios. Floc shape affects the shape factor, b_1, in the explicit model. Larger values of b_1 cause smaller drag ratio estimates (Sect. 4.5.2). Stokes law shows that $b_1 = 18$ (Stokes, 1851) for an impermeable sphere ($\Omega = 1$), so $b_1 = 20$ is commonly assumed as done here because natural particles are not perfect spheres (Ferguson and Church, 2004). Strom and Keyvani (2011) suggested that $b_1 \sim 20$ is suitable for flocs with $n_f < 2$, but $b_1 = 120$ for flocs with $n_f \geq 2.5$. Regardless of the precise value of b_1, particle shape effects only cause $b_1 > 18$ because shape irregularities induce more drag and slow the settling velocity (McNown and Malaika, 1950; Dietrich, 1982). We used a relatively low value of $b_1 = 20$ to calculate the drag ratio, so higher b_1 would only further amplify floc permeability and exacerbate the discrepancy with theory.

6.3 Environmental Controls on Flocculation

We argue that turbulence is the overriding variable controlling flocculation in the distributary channels of WLD because it not only directly affects particle collision rates and floc breakage (Winterwerp, 1998), but also sets concentration and primary particle size and mineralogy (Fig. 16). Sediment entrainment scales nonlinearly with boundary shear velocity and, along with settling and bed grain size distribution, sets the sediment concentration (e.g., García, 2008; De Leeuw et al., 2020). More turbulent flows can source larger primary particles that have distinct mineralogy (via Al/Si) than finer grains. All else equal, these effects correlate to coarser floc cutoff diameter, faster floc settling velocity, and coarser floc diameter (Eq. 6). However, increases in turbulence intensity cause floc breakage at equilibrium, thereby compensating against these. These negative feedbacks demonstrate that flocculation can buffer partially against spatiotemporal changes in turbulence, a mechanism that might explain the limited seasonal floc settling velocity variation of 0.2-0.6 mm s^{-1} in the lower Mississippi River (Osborn et al., 2023) and, more broadly, the limited global variation of 0.1 to 1 mm s^{-1} (e.g., Hill et al., 2000; Mikkelsen et al., 2007; Nghiem et al., 2022). In contrast to flocs in channels, floc predictions in wetlands appear to be more uncertain because, in the islands, Kolmogorov microscale is uncorrelated with primary particle diameter, Al/Si, and mud concentration (Fig. 16). These patterns might be because sediment dynamics are more complicated in these shallow island wetlands where two-dimensional unsteady tidal, wave, and hysteresis effects might be important (Geleynse et al., 2015; Bevington et al., 2017).

In contrast to the other factors, organic cover fraction and relative charge density vary less and are not responsible for the bulk of the variability in floc parameters (Fig. 15). This does not imply that they are unimportant for flocculation. Instead, we propose that they are allogenic catchment-wide controls on flocculation and vary over longer time scales. For example, tectonic activity and climate change can alter biological productivity and chemical weathering intensity on the catchment scale (Geider et al., 2001; West et al., 2005), altering the organic cover fraction and relative charge density through changes in organic carbon loading on sediment and water chemistry (e.g., Galy et al., 2008). The fact that theseThese effects are not directly linked to turbulence feedbacks implies that, despite their longer time scale,, implying that they can cause persistent changes in floc properties that are not simultaneously offset. In fact, organic matter might modulate turbulence and force a positive feedback that increases floc size and settling velocity because biological cohesion can limit bedform size and hence reduce the turbulent shear (i.e., increase Kolmogorov microscale) associated with bedforms (Malarkey et al., 2015; Parsons et al., 2016). In contrast, Kolmogorov microscale, sediment concentration, Al/Si, and primary particle size vary autogenically on shorter flood-to-seasonal discharge time scales. Their effects on flocculation can be considered autogenic because they adjust together in response to discharge and sediment supplydynamics within the alluvial system (e.g., Phillips et al., 2022).

7 Conclusion

Flocculation controls the transport and distribution of mud across rivers and wetlands by increasing the effective mud settling velocity. ~~Using~~To test theory controlling floc settling velocity, we combined multiple ~~techniques —~~floc data sources—a camera, in situ LISST particle size and concentration, and ~~Rouse-Vanoni~~sediment concentration-depth ~~profile inversion—we~~ profiles—in the freshwater Wax Lake Delta, LA. We not only calculated commonly constrained floc properties like diameter, settling velocity, and fractal dimension, but also made novel field measurements. Key advances of the data synthesis include isolating floc concentration and size distribution in in situ laser diffraction data and computing hitherto poorly constrained variables: effective primary particle diameter and drag ratio. We observed flocs in ~~Wax Lake Delta, LA,~~WLD with median diameters of 30 to 90 µm, bulk solid fraction of 0.05 to 0.3, and settling velocities on the order of 0.1 to 1 mm s^{-1} with little vertical variation. Flocs included~~ silt~~ grains up to 20 to 50 µm in diameter. Flocs in channels tended to be larger and lighter, while flocs in an island wetland tended to be smaller and denser. On average, floc diameter and settling velocity were an order-of-magnitude larger than those of primary particles. We used this data to validate and calibrate an explicit floc settling velocity model based on Stokes law and a semi-empirical model, which relies on hydrodynamic and geochemical data.

~~We constrained~~Using the new complete dataset of floc attributes, we tested theory for two key unknowns, effective primary particle diameter and drag ratio, in the explicit model. ~~For the first time for natural flocs, we~~Effective primary particle diameter varied between 1 and 3 µm and had a typical value of 2 µm. We verified a fractal model for effective primary particle diameter that conserves the volume and fractal space of the original primary particles~~. This result shows~~ (Fig. 8b), demonstrating that~~, assuming flocs are fractal aggregates,~~ the effective primary particle diameter is not a simple characteristic length scale ~~like the~~(i.e., median) as previous studies assumed. The median primary particle diameter systematically overestimates the effective primary particle diameter by an average factor of 2 and up to a factor of 6, leading to overestimates of floc solid fraction and settling velocity. Floc permeability, quantified by the drag ratio, has been little explored for natural flocs. ~~Measured flocs were appreciably permeable, increasing the~~The mean drag ratio was 0.51, but drag ratio ranged between 0.15 and 1 (Fig. 9a). These drag ratios indicate enhanced floc settling velocity by a mean factor of ~~about~~ 2~~.~~ and up to a factor of 7. The drag ratio estimates do not conform to ~~classic~~prior permeability theory because the theory does not consider ~~fractal structure, the~~a primary particle size distribution~~, and the presence of organic matter.~~. Instead, a new ~~permeability~~ permeable solid fraction model~~, in which permeable clusters of~~ suggests that only some primary particles ~~enhance permeability, can explain the estimates using an empirical cluster diameter that absorbs the unknowns.~~are relevant for permeability because primary particle size interactions might shield other primary particles from the main flow paths (Fig. 9b).

We ~~also verified~~tested the semi-empirical model for the first time using direct measurements of flocs. Our data validate the semi-empirical model because it predicts floc cutoff diameter, floc settling velocity, and floc diameter ~~data and~~all within a factor of 2 of the measured field data. We also showed that its floc settling velocity predictions are consistent with those of the explicit model. The semi-empirical model reveals that turbulence, sediment concentration and mineralogy, organic matter, and water chemistry control flocculation in WLD and suggests that flocs can be reasonably modeled in local equilibrium. Results ~~emphasize the importance of~~ indicate that turbulence ~~feedbacks~~controls a negative feedback on floc settling velocity because higher turbulence intensity causes higher sediment concentration, lower Al/Si (a sediment mineralogy~~,~~ proxy), and higher primary particle diameter ~~for mitigating~~through sediment entrainment dynamics (Sect. 6.4). These factors correlate with faster floc settling velocity, but are offset by shear breakage of flocs. This feedback might mitigate changes in floc ~~size and~~ settling velocity in alluvial channels on the flood and seasonal time scales~~. Changes in organic~~ over which flow turbulence typically varies. Organic matter binding and sediment surface charge interactions might affect flocculation at longer time scales because they are set by allogenic catchment-to-continental scale processes~~.~~ like biological productivity and chemical weathering of rock. Overall, the semi-empirical and explicit models are both viable options for predicting floc settling velocity in rivers and freshwater wetlands~~,~~ but require knowledge of different predictors and operate at different scales.

~~**Appendix A**~~

~~We performed X-ray fluorescence (XRF) analysis to measure sediment Al/Si on two different instruments because of sample mass limitations. We measured the absolute concentrations of Al and Si using the glass pellet fusion method on a 4 kW Zetium Panalytical XRF analyzer for 7 samples and calculated the quantitative Al/Si. However, this method requires ~1 g of sediment, which is larger than the total mass of most of our suspended sediment samples. For 20 samples with less mass, we measured the relative abundances of Al and Si using a Rigaku Primus IV XRF Spectrometer, which directly scans powder samples, and calculated the semi-quantitative Al/Si using its semi-quantitative package, SQX. We also re-analyzed the samples that had been measured on the Zetium using the Rigaku to calibrate a relationship to convert the semi-quantitative Al/Si to quantitative Al/Si ($R^2 = 0.91$; Fig. A1a). Next, we developed a linear model between sediment Al/Si and volume fraction finer than a certain grain size threshold. We tested the model coefficient of determination for many grain size thresholds (Fig. A1b). We selected a linear model between Al/Si and the volume fraction finer than 19.2 µm ($\mathrm{Al/Si} = 0.099 + 0.16[\text{fraction finer than } 19.2\ \mu\mathrm{m}]$) because this threshold yielded the highest R^2 of 0.88. We predicted Al/Si from the depth-averaged grain size distributions for all concentration profiles using this grain size relationship.~~

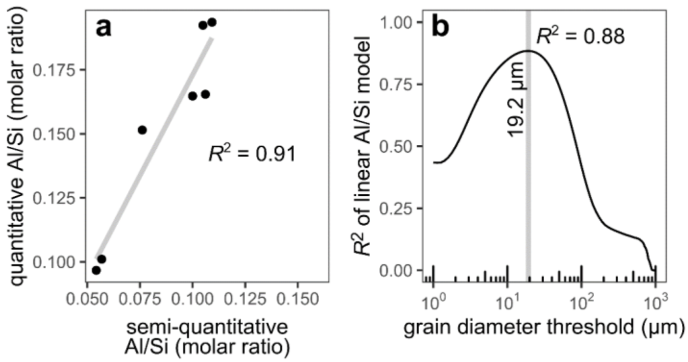

Figure A1: Sediment Al/Si calibrations. (a) Scatterplot of semi-quantitative Al/Si and quantitative Al/Si. (b) Coefficient of determination, R^2, of a linear model between Al/Si and volume fraction finer than a grain diameter threshold as a function of the threshold.

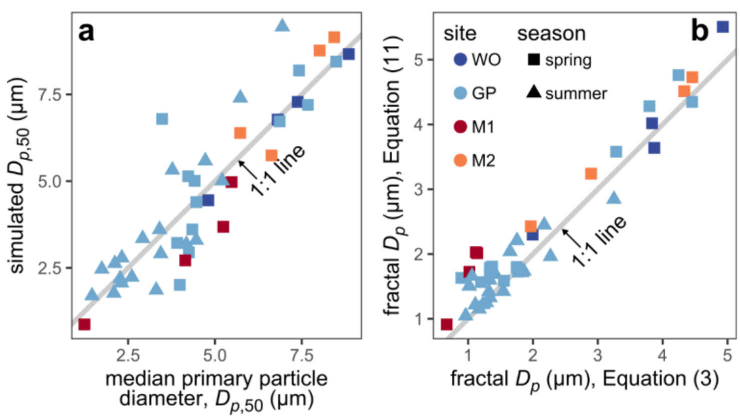

Figure A2: Fractal D_p model validation (Sect. 4.5.3 and 5.6). (a) Measured and simulated median primary particle diameter. Simulations represent random draws from the primary particle size distribution for 10,000 flocs for each data point (Sect. 4.5.3). (b) Fractal effective primary particle diameter using the full (Eq. 3) and simplified equations (Eq. 11). The legend in panel b applies to all panels.

Finally, we emphasize that the workflow of combining multiple floc methods (camera, in situ laser diffraction, sediment concentration-depth profiles) presented in this study is a powerful tool that can be used to provide a more complete description of flocs than previously done with only one or two of the individual methods.

Notation

Al/Si	Sediment Al-Si ~~ratio, ~~molar ratio
b_1	Settling velocity model constant ~~(= ~~(20), dimensionless
C_{fl}	Floc volume concentration, dimensionless
C_i	Sediment volume concentration for *i*th grain size class, dimensionless
C_{bi}	Near-bed sediment volume concentration for *i*th grain size class, dimensionless
C_m	Depth-averaged mud volume concentration, dimensionless
D_c	Cluster diameter, m
D_f	Floc diameter, m
$D_{f,50}$	Median floc diameter, m
D_p	Effective primary particle diameter, m
$D_{p,50}$	Median primary particle diameter, m
$\widetilde{D}_{p,50}$	Depth-averaged median primary particle diameter, m
D_t	Floc cutoff diameter, m
g	Gravitational acceleration ~~(= ~~(9.81 m s^{-2}), m s^{-2}
h	Local water depth, m
h_b	Near-bed height ~~(= ~~(0.1h), m
k	Floc permeability, m^2
n_f	Floc fractal dimension, dimensionless
n_r	Permeable fractal dimension, dimensionless
p_i	Rouse number for *i*th grain size class, dimensionless
R_s	Submerged specific gravity of sediment ~~(= ~~(1.65), dimensionless
u_*	Shear velocity, m s^{-1}
w_s	Floc settling velocity, m s^{-1}
w_{si}	In situ particle settling velocity for *i*th grain size class, m s^{-1}
β	Sediment diffusivity ratio, dimensionless
β_{fl}	Floc diffusivity ratio, dimensionless
η	Kolmogorov microscale, m
θ	Organic cover fraction, dimensionless

Formatted: French (France)

κ	Von Kármán constant ~~(= ~~(0.41), dimensionless
ν	Kinematic viscosity of water ~~(= ~~(10^{-6}), $m^2\ s^{-1}$
ξ^{-2}	Dimensionless floc permeability, dimensionless
ρ	Water density ~~(= ~~(1000), kg m^{-3}
ρ_s	Sediment density ~~(= ~~(2650), kg m^{-3}
Φ	Relative charge density, dimensionless
φ	Floc solid fraction, dimensionless
$\bar{\varphi}$	Bulk floc solid fraction, dimensionless
φ_r	Permeable solid fraction, dimensionless
Ω	Drag ratio, dimensionless

Code availability

NA

Data availability

NASA Delta-X data are available online at https://daac.ornl.gov/cgi-bin/dataset_lister.pl?p=41. Additional data will be uploaded to an online repository on manuscript acceptance.

Author contribution

JAN and MPL conceived the study. JAN, GKL, JPH, GS, CGF, and MPL collected samples and made measurements in the field. JAN, GKL, and GS analyzed samples in the lab. JAN analyzed data and wrote the original paper with supervision by MPL. All authors contributed to data interpretation, review, and editing.

Competing interests

The authors declare that they have no conflict of interest.

Acknowledgements

The NASA Delta-X project is funded by the Science Mission Directorate's Earth Science Division through the Earth Venture Suborbital-3 Program NNH17ZDA001N-EVS3. JAN acknowledges funding from NASA FINESST Grant 80NSSC20K1645. The authors thank Mathieu Dellinger and Amanda Hayton for conducting the ion chromatography at Durham University. We thank Sijia Dong for measuring DIC concentrations. We thank Claire Bucholz, Youli Li, Juliet Ryan-Davis, and Miguel Zepeda-Rosales for assistance with XRF analysis. We thank John Bourg, Madison Douglas, Paola Passalacqua, Eric Prokocki, Maryn Sanders, Adam Songy, ~~and~~ Kyle Wright~~ for field assistance in the Delta-X field campaigns. We also thank participants in~~, and Caltech's fall 2019 Ge 121a class for field ~~support in the 2019 field campaign~~assistance.

References

Agrawal, Y. C. and Pottsmith, H. C.: Instruments for particle size and settling velocity observations in sediment transport, Marine Geology, 168, 89–114, https://doi.org/10.1016/S0025-3227(00)00044-X, 2000.

Agrawal, Y. C., Whitmire, A., Mikkelsen, O. A., and Pottsmith, H. C.: Light scattering by random shaped particles and consequences on measuring suspended sediments by laser diffraction, Journal of Geophysical Research: Oceans, 113, https://doi.org/10.1029/2007JC004403, 2008.

Baptist, M. J., Babovic, V., Rodríguez Uthurburu, J., Keijzer, M., Uittenbogaard, R. E., Mynett, A., and Verwey, A.: On inducing equations for vegetation resistance, Journal of Hydraulic Research, 45, 435–450, https://doi.org/10.1080/00221686.2007.9521778, 2007.

Benson, T. and French, J. R.: InSiPID: A new low-cost instrument for in situ particle size measurements in estuarine and coastal waters, Journal of Sea Research, 58, 167–188, https://doi.org/10.1016/j.seares.2007.04.003, 2007.

Bevington, A. E., Twilley, R. R., Sasser, C. E., and Holm Jr, G. O.: Contribution of river floods, hurricanes, and cold fronts to elevation change in a deltaic floodplain, northern Gulf of Mexico, USA, Estuarine, Coastal and Shelf Science, 191, 188–200, https://doi.org/10.1016/j.ecss.2017.04.010, 2017.

Blair, N. E. and Aller, R. C.: The Fate of Terrestrial Organic Carbon in the Marine Environment, Annual Review of Marine Science, 4, 401–423, https://doi.org/10.1146/annurev-marine-120709-142717, 2012.

Blum, M. D. and Roberts, H. H.: Drowning of the Mississippi Delta due to insufficient sediment supply and global sea-level rise, Nature Geoscience, 2, 488–491, https://doi.org/10.1038/NGEO55, 2009.

Bouchez, J., Galy, V., Hilton, R. G., Gaillardet, J., Moreira-Turcq, P., Pérez, M. A., France-Lanord, C., and Maurice, L.: Source, transport and fluxes of Amazon River particulate organic carbon: Insights from river sediment depth-profiles, Geochimica et Cosmochimica Acta, 133, 280–298, https://doi.org/10.1016/j.gca.2014.02.032, 2014.

Braat, L., van Kessel, T., Leuven, J. R., and Kleinhans, M. G.: Effects of mud supply on large-scale estuary morphology and development over centuries to millennia, Earth Surface Dynamics, 5, 617–652, https://doi.org/10.5194/esurf-5-617-2017, 2017.

Brinkman, H. C.: A calculation of the viscous force exerted by a flowing fluid on a dense swarm of particles, Applied Scientific Research, A1, 27–34, https://doi.org/10.1007/BF02120313, 1947.

Bushell, G. and Amal, R.: Fractal aggregates of polydisperse particles, Journal of colloid and interface science, 205, 459–469, https://doi.org/10.1006/jcis.1998.5667, 1998.

Bushell, G. and Amal, R.: Measurement of fractal aggregates of polydisperse particles using small-angle light scattering, Journal of colloid and interface science, 221, 186–194, https://doi.org/10.1006/jcis.1999.6532, 2000.

Carstens, M. R.: Accelerated motion of a spherical particle, Eos, Transactions American Geophysical Union, 33, 713–721, https://doi.org/10.1029/TR033i005p00713, 1952.

Chase, R. R.: Settling behavior of natural aquatic particulates, Limnology and Oceanography, 24, 417–426, https://doi.org/10.4319/lo.1979.24.3.0417, 1979.

Cohen, S., Syvitski, J., Ashley, T., Lammers, R., Fekete, B., and Li, H.-Y.: Spatial trends and drivers of bedload and suspended sediment fluxes in global rivers, Water Resources Research, 58, e2021WR031583, https://doi.org/10.1029/2021WR031583, 2022.

Craig, M. J., Baas, J. H., Amos, K. J., Strachan, L. J., Manning, A. J., Paterson, D. M., Hope, J. A., Nodder, S. D., and Baker, M. L.: Biomediation of submarine sediment gravity flow dynamics, Geology, 48, 72–76, https://doi.org/10.1130/G46837.1, 2020.

Csanady, G. T.: Turbulent diffusion of heavy particles in the atmosphere, Journal of Atmospheric Sciences, 20, 201–208, https://doi.org/10.1175/1520-0469(1963)020%3C0201:TDOHPI%3E2.0.CO;2, 1963.

Davies, C. N.: The separation of airborne dust and particles, Proceedings of the Institution of mechanical engineers, 167, 185–213, https://doi.org/10.1177/002034835316701b13, 1953.

De Leeuw, J., Lamb, M. P., Parker, G., Moodie, A. J., Haught, D., Venditti, J. G., and Nittrouer, J. A.: Entrainment and suspension of sand and gravel, Earth Surface Dynamics, 8, 485–504, https://doi.org/10.5194/esurf-8-485-2020, 2020.

Deng, Z., He, Q., Manning, A. J., and Chassagne, C.: A laboratory study on the behavior of estuarine sediment flocculation as function of salinity, EPS and living algae, Marine Geology, 459, 107029, https://doi.org/10.1016/j.margeo.2023.107029, 2023.

Derjaguin, B. V. and Landau, L.: Theory of the stability of strongly charged lyophobic sol and of the adhesion of strongly charged particles in solutions of electrolytes, Acta Physico Chimica URSS, 14, 633, 1941.

Dietrich, W. E.: Settling velocity of natural particles, Water Resources Research, 18, 1615–1626, https://doi.org/10.1029/WR018i006p01615, 1982.

Dong, S., Subhas, A. V., Rollins, N. E., Naviaux, J. D., Adkins, J. F., and Berelson, W. M.: A kinetic pressure effect on calcite dissolution in seawater, Geochimica et Cosmochimica Acta, 238, 411–423, https://doi.org/10.1016/j.gca.2018.07.015, 2018.

Douglas, M. M., Li, G. K., Fischer, W. W., Rowland, J. C., Kemeny, P. C., West, A. J., Schwenk, J., Piliouras, A. P., Chadwick, A. J., and Lamb, M. P.: Organic carbon burial by river meandering partially offsets bank-erosion carbon fluxes in a discontinuous permafrost floodplain, Earth Surface Dynamics ~~Discussions~~, 10, ~~1–24~~421–435, https://doi.org/10.5194/esurf-10-421-2022, 2022.

Droppo, I. G. and Ongley, E. D.: Flocculation of suspended sediment in rivers of southeastern Canada, Water Research, 28, 1799–1809, https://doi.org/10.1016/0043-1354(94)90253-4, 1994.

Dunne, K. B. J., Nittrouer, J. A., Abolfazli, E., Osborn, R., and Strom, K. B.: Hydrodynamically-driven deposition of mud in river systems, Geophysical Research Letters, 51, e2023GL107174, https://doi.org/10.1029/2023GL107174, 2024.

Dyer, K. R. and Manning, A. J.: Observation of the size, settling velocity and effective density of flocs, and their fractal dimensions, Journal of sea research, 41, 87–95, https://doi.org/10.1016/S1385-1101(98)00036-7, 1999.

Edwards, T. K. and Glysson, G. D.: Field methods for measurement of fluvial sediment, US Geological Survey Denver, CO, 1999.

~~Egan, G., Chang,~~Eisma, D.: Flocculation~~ G., Manning, A. J., Monismith, S.,~~ and ~~Fringer, O.: On the variability~~de-flocculation of ~~floc characteristics~~suspended matter in ~~a shallow estuary,~~estuaries, Netherlands Journal of ~~Geophysical Research: Oceans, 127, e2021JC018343~~sea research, 20, 183–199, https://doi.org/10.~~1029/2021JC018343, 2022~~1016/0077-7579(86)90041-4, 1986.

Eisma, D., Cadée, G. C., Laane, R., and Kalf, J.: Preliminary results of AURELIA-and NAVICULA Cruises in the Rhine-and Ems-estuaries, January-February, 1982, Mitteilungen aus dem Geologisch-Paläontologischen Institut der Universität Hamburg, 633–654, 1982.

Ferguson, R. I. and Church, M.: A Simple Universal Equation for Grain Settling Velocity, Journal of Sedimentary Research, 74, 933–937, https://doi.org/10.1306/051204740933, 2004.

Fichot, C. and Harringmeyer, J.: Delta-X: In situ Beam Attenuation and Particle Size from LISST-200X, 2021, ORNL DAAC, https://doi.org/10.3334/ORNLDAAC/2077, 2021.

Galy, V., Beyssac, O., France-Lanord, C., and ~~Lartiges, B.: Loading and fate~~Eglinton, T.: Recycling of ~~particulate organic~~graphite during Himalayan erosion: a geological stabilization of carbon ~~from~~in the ~~Himalaya to the Ganga-Brahmaputra delta, Geochimica et Cosmochimica Acta, 72, 1767–1787~~crust, Science, 322, 943–945, https://doi.org/10.~~1016/j.gca.2008.01.027~~1126/science.1161408, 2008.

~~García~~Garcia, M~~. H.: Sediment Transport and Morphodynamics,~~.: Sedimentation Engineering: Processes, Measurements, Modeling, and Practice, ~~21–163,~~ https://doi.org/10.1061/9780784408148~~.ch02~~, 2008.

Geider, R. J., Delucia, E. H., Falkowski, P. G., Finzi, A. C., Grime, J. P., Grace, J., Kana, T. M., La Roche, J., Long, S. P., and Osborne, B. A.: Primary productivity of planet earth: biological determinants and physical constraints in terrestrial and aquatic habitats, Global Change Biology, 7, 849–882, https://doi.org/10.1046/j.1365-2486.2001.00448.x, 2001.

Geleynse, N., Hiatt, M., Sangireddy, H., and Passalacqua, P.: Identifying environmental controls on the shoreline of a natural river delta, Journal of Geophysical Research: Earth Surface, 120, 877–893, https://doi.org/10.1002/2014JF003408, 2015.

Gibbs, R. J.: Estuarine flocs: their size, settling velocity and density, Journal of Geophysical Research: Oceans, 90, 3249–3251, https://doi.org/10.1029/JC090iC02p03249, 1985.

Gmachowski, L.: Mass–radius relation for fractal aggregates of polydisperse particles, Colloids and Surfaces A: Physicochemical and Engineering Aspects, 224, 45–52, https://doi.org/10.1016/S0927-7757(03)00318-2, 2003.

Graf, W. H. and Cellino, M.: Suspension flows in open channels; experimental study, Journal of Hydraulic Research, 40, 435–447, https://doi.org/10.1080/00221680209499886, 2002.

Graham, G. W~~. and Nimmo Smith, W. A. M.: The application of holography to the analysis of size and settling velocity of suspended cohesive sediments, Limnology and Oceanography: Methods, 8, 1–15, https://doi.org/10.4319/lom.2010.8.1, 2010.~~

Graham, G. W., Davies, E. J., Nimmo-Smith, W. A. M., Bowers, D. G., and Braithwaite, K. M.: Interpreting LISST-100X measurements of particles with complex shape using digital in-line holography, Journal of Geophysical Research: Oceans, 117, https://doi.org/10.1029/2011JC007613, 2012.

Gregory, J. and Barany, S.: Adsorption and flocculation by polymers and polymer mixtures, Advances in colloid and interface science, 169, 1–12, https://doi.org/10.1016/j.cis.2011.06.004, 2011.

Guo, L. and He, Q.: Freshwater flocculation of suspended sediments in the Yangtze River, China, Ocean Dynamics, 61, 371–386, https://doi.org/10.1007/s10236-011-0391-x, 2011.

Hill, P. S., Milligan, T. G., and Geyer, W. R.: Controls on effective settling velocity of suspended sediment in the Eel River flood plume, Continental Shelf Research, 20, 2095–2111, https://doi.org/10.1016/S0278-4343(00)00064-9, 2000.

Hill, P. S., Voulgaris, G., and Trowbridge, J. H.: Controls on floc size in a continental shelf bottom boundary layer, Journal of Geophysical Research: Oceans, 106, 9543–9549, https://doi.org/10.1029/2000JC900102, 2001.

Holm, G. O. and Sasser, C. E.: Differential salinity response between two Mississippi River subdeltas: implications for changes in plant composition, Estuaries, 24, 78–89, https://doi.org/10.2307/1352815, 2001.

Izquierdo–Ayala, K., Garcia–Aragon, J. A., Castillo–Uzcanga, M. M., and Salinas-Tapia, H.: Freshwater flocculation dependence on turbulence properties in the Usumacinta river, Journal of Hydraulic Engineering, 147, 05021009, https://doi.org/10.1061/(ASCE)HY.1943-7900.0001940, 2021.

Izquierdo-Ayala, K., García-Aragón, J. A., Castillo-Uzcanga, M. M., Díaz-Delgado, C., Carrillo, L., and Salinas-Tapia, H.: Flocculation Patterns Related to Intra-Annual Hydrodynamics Variability in the Lower Grijalva-Usumacinta System, Water, 15, 292, https://doi.org/10.3390/w15020292, 2023.

Jarvis, P., Jefferson, B., and Parsons, S. A.: Measuring floc structural characteristics, Reviews in Environmental Science and Bio/Technology, 4, 1–18, https://doi.org/10.1007/s11157-005-7092-1, 2005.

Jensen, D. J., Cavanaugh, K. C., Thompson, D. R., Fagherazzi, S., Cortese, L., and Simard, M.: Leveraging the historical Landsat catalog for a remote sensing model of wetland accretion in coastal Louisiana, Journal of Geophysical Research: Biogeosciences, 127, e2022JG006794, https://doi.org/10.1029/2022JG006794, 2022.

Johnson, C. P., Li, X., and Logan, B. E.: Settling velocities of fractal aggregates, Environmental science & technology, 30, 1911–1918, https://doi.org/10.1021/es950604g, 1996.

Keyvani, A. and Strom, K.: A fully-automated image processing technique to improve measurement of suspended particles and flocs by removing out-of-focus objects, Computers & Geosciences, 52, 189–198, https://doi.org/10.1016/j.cageo.2012.08.018, 2013.

Khelifa, A. and Hill, P. S.: Models for effective density and settling velocity of flocs, Journal of Hydraulic Research, 44, 390–401, https://doi.org/10.1080/00221686.2006.9521690, 2006.

Kim, A. S. and Stolzenbach, K. D.: The permeability of synthetic fractal aggregates with realistic three-dimensional structure, Journal of colloid and interface science, 253, 315–328, https://doi.org/10.1006/jcis.2002.8525, 2002.

Kranck, K.: The role of flocculation in the filtering of particulate matter in estuaries, The estuary as a filter, 159–175, https://doi.org/10.1016/B978-0-12-405070-9.50014-1, 1984.

Kranck, K. and Milligan, T.: Macroflocs: production of marine snow in the laboratory, Marine Ecology - Progress Series, 3, 19–24, 1980.

Kranenburg, C.: The fractal structure of cohesive sediment aggregates, Estuarine, Coastal and Shelf Science, 39, 451–460, https://doi.org/10.1016/S0272-7714(06)80002-8, 1994.

Krishnappan, B. G.: In situ size distribution of suspended particles in the Fraser River, Journal of Hydraulic Engineering, 126, 561–569, https://doi.org/10.1061/(ASCE)0733-9429(2000)126:8(561), 2000.

~~Kumar, R. G., Strom, K. B., and Keyvani, A.: Floc properties and settling velocity of San Jacinto estuary mud under variable shear and salinity conditions, Continental Shelf Research, 30, 2067–2081, https://doi.org/10.1016/j.csr.2010.10.006, 2010.~~

Kuprenas, R., Tran, D., and Strom, K.: A Shear-Limited Flocculation Model for Dynamically Predicting Average Floc Size, Journal of Geophysical Research: Oceans, 123, 6736–6752, https://doi.org/10.1029/2018JC014154, 2018.

Lamb, M. P., De Leeuw, J., Fischer, W. W., Moodie, A. J., Venditti, J. G., Nittrouer, J. A., Haught, D., and Parker, G.: Mud in rivers transported as flocculated and suspended bed material, Nature Geoscience, 13, 566–570, https://doi.org/10.1038/s41561-020-0602-5, 2020.

Larsen, L. G., Harvey, J. W., and Crimaldi, J. P.: Morphologic and transport properties of natural organic floc, Water Resources Research, 45, https://doi.org/10.1029/2008WR006990, 2009.

Latimer, R. A. and Schweizer, C. W.: The Atchafalaya River Study: a report based upon engineering and geological studies of the enlargement of Old and Atchafalaya Rivers, 1951.

Lawrence, T. J., Carr, S. J., Wheatland, J. A. T., Manning, A. J., and Spencer, K. L.: Quantifying the 3D structure and function of porosity and pore space in natural sediment flocs, Journal of Soils and Sediments, 22, 3176–3188, https://doi.org/10.1007/s11368-022-03304-x, 2022.

Lawrence, T. J., Carr, S. J., Manning, A. J., Wheatland, J. A. T., Bushby, A. J., and Spencer, K. L.: Functional behaviour of flocs explained by observed 3D structure and porosity, Frontiers in Earth Science, 11, 1264953, https://doi.org/10.3389/feart.2023.1264953, 2023.

Lee, B. J., Kim, J., Hur, J., Choi, I. H., Toorman, E. A., Fettweis, M., and Choi, J. W.: Seasonal Dynamics of Organic Matter Composition and Its Effects on Suspended Sediment Flocculation in River Water, Water Resources Research, 55, 6968–6985, https://doi.org/10.1029/2018WR024486, 2019.

Li, X. and Logan, B. E.: Collision frequencies of fractal aggregates with small particles by differential sedimentation, Environmental science & technology, 31, 1229–1236, https://doi.org/10.1021/es960771w, 1997.

Li, X.-Y. and Logan, B. E.: Permeability of fractal aggregates, Water research, 35, 3373–3380, https://doi.org/10.1016/S0043-1354(01)00061-6, 2001.

~~Maggi, F., Mietta, F~~Livsey, D. N., Crosswell, J. R., Turner, R. D. R., Steven, A. D. L., and ~~Winterwerp, J. C.: Effect~~Grace, P. R.: Flocculation of ~~variable fractal dimension on~~Riverine Sediment Draining to the ~~floc size distribution~~Great Barrier Reef, Implications for Monitoring and Modeling of ~~suspended cohesive sediment~~Sediment Dispersal Across Continental Shelves, Journal of ~~Hydrology, 343, 43–55~~Geophysical Research: Oceans, 127, e2021JC017988, https://doi.org/10.~~1016/j.jhydrol.2007.05.035, 2007~~1029/2021JC017988, 2022.

~~Matsuo, T. and Unno, H.: Forces acting on floc and strength of floc, Journal of the Environmental Engineering Division, 107, 527–545, https://doi.org/10.1061/JEEGAV.0001174, 1981.~~

Malarkey, J., Baas, J. H., Hope, J. A., Aspden, R. J., Parsons, D. R., Peakall, J., Paterson, D. M., Schindler, R. J., Ye, L., and Lichtman, I. D.: The pervasive role of biological cohesion in bedform development, Nature communications, 6, 6257, https://doi.org/10.1038/ncomms7257, 2015.

Manning, A. J., Baugh, J. V., Spearman, J. R., and Whitehouse, R. J.: Flocculation settling characteristics of mud: sand mixtures, Ocean dynamics, 60, 237–253, https://doi.org/10.1007/s10236-009-0251-0, 2010.

Mayer, L. M.: Surface area control of organic carbon accumulation in continental shelf sediments, Geochimica et Cosmochimica Acta, 58, 1271–1284, https://doi.org/10.1016/0016-7037(94)90381-6, 1994.

McCave, I. N.: Size spectra and aggregation of suspended particles in the deep ocean, Deep Sea Research Part A. Oceanographic Research Papers, 31, 329–352, https://doi.org/10.1016/0198-0149(84)90088-8, 1984.

McNown, J. S. and Malaika, J.: Effects of particle shape on settling velocity at low Reynolds numbers, Eos, Transactions American Geophysical Union, 31, 74–82, https://doi.org/10.1029/TR031i001p00074, 1950.

Mehta, A. J. and Partheniades, E.: An investigation of the depositional properties of flocculated fine sediments, Journal of Hydraulic Research, 13, 361–381, https://doi.org/10.1080/00221687509499694, 1975.

Mietta, F., Chassagne, C., Manning, A. J., and Winterwerp, J. C.: Influence of shear rate, organic matter content, pH and salinity on mud flocculation, Ocean Dynamics, 59, 751–763, https://doi.org/10.1007/s10236-009-0231-4, 2009.

Mikkelsen, O. and Pejrup, M.: The use of a LISST-100 laser particle sizer for in-situ estimates of floc size, density and settling velocity, Geo-Marine Letters, 20, 187–195, https://doi.org/10.1007/s003670100064, 2001.

Mikkelsen, O. A., Milligan, T. G., Hill, P. S., and Moffatt, D.: INSSECT—an instrumented platform for investigating floc properties close to the seabed, Limnology and Oceanography: Methods, 2, 226–236, https://doi.org/10.4319/lom.2004.2.226, 2004.

Mikkelsen, O. A., Hill, P. S., Milligan, T. G., and Chant, R. J.: In situ particle size distributions and volume concentrations from a LISST-100 laser particle sizer and a digital floc camera, Continental Shelf Research, 25, 1959–1978, https://doi.org/10.1016/j.csr.2005.07.001, 2005.

Mikkelsen, O. A., Hill, P. S., and Milligan, T. G.: Seasonal and spatial variation of floc size, settling velocity, and density on the inner Adriatic Shelf (Italy), Continental Shelf Research, 27, 417–430, https://doi.org/10.1016/j.csr.2006.11.004, 2007.

Moodie, A. J., Nittrouer, J. A., Ma, H., Carlson, B. N., Wang, Y., Lamb, M. P., and Parker, G.: Suspended-sediment induced stratification inferred from concentration and velocity profile measurements in the lower Yellow River, China, Water Resources Research, e2020WR027192, https://doi.org/10.1029/2020WR027192, 2020.

Neale, G., Epstein, N., and Nader, W.: Creeping flow relative to permeable spheres, Chemical Engineering Science, 28, 1865–1874, https://doi.org/10.1016/0009-2509(73)85070-5, 1973.

Nelson, C. H. and Lamothe, P. J.: Heavy metal anomalies in the Tinto and Odiel river and estuary system, Spain, Estuaries, 16, 496–511, https://doi.org/10.2307/1352597, 1993.

Nezu, I. and Nakagawa, H.: Turbulence in open-channel flows, AA Balkema, Rotterdam, 1–281, 1993.

Nghiem, J., Salter, G., and Lamb, M. P.: Delta-X: Bed and Suspended Sediment Grain Size, MRD, LA, USA, 2021, Version 2, ORNL DAAC, https://doi.org/10.3334/ORNLDAAC/2135, 2021.

Nghiem, J. A., Fischer, W. W., Li, G. K., and Lamb, M. P.: A Mechanistic Model for Mud Flocculation in Freshwater Rivers, Journal of Geophysical Research: Earth Surface, e2021JF006392, https://doi.org/10.1029/2021JF006392, 2022.

Nicholas, A. P. and Walling, D. E.: The significance of particle aggregation in the overbank deposition of suspended sediment on river floodplains, Journal of Hydrology, 186, 275–293, https://doi.org/10.1016/S0022-1694(96)03023-5, 1996.

Osborn, R., Dillon, B., Tran, D., Abolfazli, E., Dunne, K. B., Nittrouer, J. A., and Strom, K.: FlocARAZI: an in-situ, image-based profiling instrument for sizing solid and flocculated suspended sediment, Journal of Geophysical Research: Earth Surface, e2021JF006210, https://doi.org/10.1029/2021JF006210, 2021.

Osborn, R., Dunne, K. B., Ashley, T., Nittrouer, J. A., and Strom, K.: The flocculation state of mud in the lowermost freshwater reaches of the Mississippi River: spatial distribution of sizes, seasonal changes, and their impact on vertical concentration profiles, Journal of Geophysical Research: Earth Surface, e2022JF006975, https://doi.org/10.1029/2022JF006975, 2023.

Parsons, D. R., Schindler, R. J., Hope, J. A., Malarkey, J., Baas, J. H., Peakall, J., Manning, A. J., Ye, L., Simmons, S., and Paterson, D. M.: The role of biophysical cohesion on subaqueous bed form size, Geophysical research letters, 43, 1566–1573, https://doi.org/10.1002/2016GL067667, 2016.

Partheniades, E.: Erosion and deposition of cohesive soils, Journal of the Hydraulics Division, 91, 105–139, https://doi.org/10.1061/JYCEAJ.0001165, 1965.

Phillips, C. B., Masteller, C. C., Slater, L. J., Dunne, K. B., Francalanci, S., Lanzoni, S., Merritts, D. J., Lajeunesse, E., and Jerolmack, D. J.: Threshold constraints on the size, shape and stability of alluvial rivers, Nature Reviews Earth & Environment, 3, 406–419, https://doi.org/10.1038/s43017-022-00282-z, 2022.

Pizzuto, J. E.: Long-term storage and transport length scale of fine sediment: Analysis of a mercury release into a river, Geophysical Research Letters, 41, 5875–5882, https://doi.org/10.1002/2014GL060722, 2014.

Roberts, H. H., Adams, R. D., and Cunningham, R. H. W.: Evolution of sand-dominant subaerial phase, Atchafalaya Delta, Louisiana, AAPG Bulletin, 64, 264–279, https://doi.org/10.1306/2F918964-16CE-11D7-8645000102C1865D, 1980.

Roberts, W., Le Hir, P., and Whitehouse, R. J. S.: Investigation using simple mathematical models of the effect of tidal currents and waves on the profile shape of intertidal mudflats, Continental Shelf Research, 20, 1079–1097, https://doi.org/10.1016/S0278-4343(00)00013-3, 2000.

Rommelfanger, N., Vowinckel, B., Wang, Z., Dohrmann, R., Meiburg, E., and Luzzatto-Fegiz, P.: A simple criterion and experiments for onset of flocculation in kaolin clay suspensions, arXiv preprint arXiv:2203.15545, https://doi.org/10.48550/arXiv.2203.15545, 2022.

Rouse, H.: Modern conceptions of the mechanics of fluid turbulence, Transactions of the American Society of Civil Engineers, 102, 463–505, https://doi.org/10.1061/TACEAT.0004872, 1937.

Schindler, R. J., Parsons, D. R., Ye, L., Hope, J. A., Baas, J. H., Peakall, J., Manning, A. J., Aspden, R. J., Malarkey, J., and Simmons, S.: Sticky stuff: Redefining bedform prediction in modern and ancient environments, Geology, 43, 399–402, https://doi.org/10.1130/G36262.1, 2015.

Sequoia Scientific: LISST-200X Particle Size Analyzer User's Manual, 2022.

Shen, X., Lee, B. J., Fettweis, M., and Toorman, E. A.: A tri-modal flocculation model coupled with TELEMAC for estuarine muds both in the laboratory and in the field, Water research, 145, 473–486, https://doi.org/10.1016/j.watres.2018.08.062, 2018.

Smellie, R. H. and La Mer, V. K.: Flocculation, subsidence and filtration of phosphate slimes: VI. A quantitative theory of filtration of flocculated suspensions, Journal of Colloid Science, 13, 589–599, https://doi.org/10.1016/0095-8522(58)90071-0, 1958.

Smith, S. J. D. and Friedrichs, C. T.: Size and settling velocitiesMcLean, S. R.: Spatially averaged flow over a wavy surface, Journal of cohesive flocs and suspended sediment aggregates in a trailing suction hopper dredge plume, Continental ShelfGeophysical Research, 31, S50–S6382, 1735–1746, https://doi.org/10.1016/j.csr.2010.04.002, 20111029/JC082i012p01735, 1977.

Smith, S. J. and Friedrichs, C. T.: Image processing methods for in situ estimation of cohesive sediment floc size, settling velocity, and density, Limnology and Oceanography: Methods, 13, 250–264, https://doi.org/10.1002/lom3.10022, 2015.

Son, M. and Hsu, T.-J.: The effects of flocculation and bed erodibility on modeling cohesive sediment resuspension, Journal of Geophysical Research: Oceans, 116, https://doi.org/10.1029/2010JC006352, 2011.

Soulsby, R. L. and Dyer, K. R.: The form of the near-bed velocity profile in a tidally accelerating flow, Journal of Geophysical Research: Oceans, 86, 8067–8074, https://doi.org/10.1029/JC086iC09p08067, 1981.

Soulsby, R. L., Manning, A. J., Spearman, J., and Whitehouse, R. J. S.: Settling velocity and mass settling flux of flocculated estuarine sediments, Marine Geology, 339, 1–12, https://doi.org/10.1016/j.margeo.2013.04.006, 2013.

Spencer, K. L., Wheatland, J. A., Bushby, A. J., Carr, S. J., Droppo, I. G., and Manning, A. J.: A structure–function based approach to floc hierarchy and evidence for the non-fractal nature of natural sediment flocs, Scientific reports, 11, 1–10, https://doi.org/10.1038/s41598-021-93302-9, 2021.

Stokes, G. G.: On the effect of the internal friction of fluids on the motion of pendulums, Transactions of the Cambridge Philosophical Society, 1851.

Strom, K. and Keyvani, A.: An explicit full-range settling velocity equation for mud flocs, Journal of Sedimentary Research, 81, 921–934, https://doi.org/10.2110/jsr.2011.62, 2011.

Syvitski, J. P., Asprey, K. W., and Leblanc, K. W. G.: In-situ characteristics of particles settling within a deep-water estuary, Deep Sea Research Part II: Topical Studies in Oceanography, 42, 223–256, https://doi.org/10.1016/0967-0645(95)00013-G, 1995.

Syvitski, J. P., Kettner, A. J., Overeem, I., Hutton, E. W., Hannon, M. T., Brakenridge, G. R., Day, J., Vörösmarty, C., Saito, Y., and Giosan, L.: Sinking deltas due to human activities, Nature Geoscience, 2, 681–686, https://doi.org/10.1038/ngeo629, 2009.

Tambo, N. and Watanabe, Y.: Physical characteristics of flocs—I. The floc density function and aluminium floc, Water Research, 13, 409–419, https://doi.org/10.1016/0043-1354(79)90033-2, 1979.

Tennekes, H. and Lumley, J. L.: A first course in turbulence, MIT Press, 1972.

Tran, D. and Strom, K.: Floc sizes and resuspension rates from fresh deposits: Influences of suspended sediment concentration, turbulence, and deposition time, Estuarine, Coastal and Shelf Science, 229, 106397, https://doi.org/10.1016/j.ecss.2019.106397, 2019.

Tran, D., Kuprenas, R., and Strom, K.: How do changes in suspended sediment concentration alone influence the size of mud flocs under steady turbulent shearing?, Continental Shelf Research, 158, 1–14, https://doi.org/10.1016/j.csr.2018.02.008, 2018.

Van Leussen, W.: Aggregation of Particles, Settling Velocity of Mud Flocs A Review, in: Physical Processes in Estuaries, Berlin, Heidelberg, 347–403, https://doi.org/10.1007/978-3-642-73691-9_19, 1988.

~~Van Rijn, L. C.: Sediment Transport, Part II: Suspended Load Transport,~~Verwey, E. J. W.: Theory of the stability of lyophobic colloids., The Journal of ~~Hydraulic Engineering, 110, 1613–1641~~Physical Chemistry, 51, 631–636, https://doi.org/10.~~1061/(ASCE)0733-9429(1984)110:11(1613), 1984~~1021/j150453a001, 1947.

Walling, D. E. and Fang, D.: Recent trends in the suspended sediment loads of the world’s rivers, Global and planetary change, 39, 111–126, https://doi.org/10.1016/S0921-8181(03)00020-1, 2003.

West, A. J., Galy, A., and Bickle, M.: Tectonic and climatic controls on silicate weathering, Earth and Planetary Science Letters, 235, 211–228, https://doi.org/10.1016/j.epsl.2005.03.020, 2005.

Whitehouse, R., Soulsby, R., Roberts, W., and Mitchener, H.: Dynamics of estuarine muds, Thomas Telford, 2000.

Winterwerp, J. C.: A simple model for turbulence induced flocculation of cohesive sediment, Journal of Hydraulic Research, 36, 309–326, https://doi.org/10.1080/00221689809498621, 1998.

Woodfield, D. and Bickert, G.: An improved permeability model for fractal aggregates settling in creeping flow, Water research, 35, 3801–3806, https://doi.org/10.1016/S0043-1354(01)00128-2, 2001.

Wright, S. and Parker, G.: Density stratification effects in sand-bed rivers, Journal of Hydraulic Engineering, 130, 783–795, https://doi.org/10.1061/(ASCE)0733-9429(2004)130:8(783), 2004.

Xu, F., Wang, D.-P., and Riemer, N.: Modeling flocculation processes of fine-grained particles using a size-resolved method: comparison with published laboratory experiments, Continental Shelf Research, 28, 2668–2677, https://doi.org/10.1016/j.csr.2008.09.001, 2008.

Yu, X. and Somasundaran, P.: Role of polymer conformation in interparticle-bridging dominated flocculation, Journal of Colloid and Interface Science, 177, 283–287, https://doi.org/10.1006/jcis.1996.0033, 1996.

Zeichner, S. S., Nghiem, J., Lamb, M. P., Takashima, N., De Leeuw, J., Ganti, V., and Fischer, W. W.: Early plant organics increased global terrestrial mud deposition through enhanced flocculation, Science, 371, 526–529, https://doi.org/10.1126/science.abd0379, 2021.

Formatted: English (United States)